nature portfolio

https://doi.org/10.1038/s41563-021-00934-3

Supplementary information

Thermally conductive ultra-low-*k* dielectric layers based on two-dimensional covalent organic frameworks

In the format provided by the authors and unedited

Supplementary Information

Thermally Conductive Ultra-Low-*k* Dielectric Layers Based on Two-Dimensional Covalent Organic Frameworks

Austin M. Evans[1ǂ], Ashutosh Giri[2, 3ǂ], Vinod K. Sangwan[4], Sangni Xun[5,6,7], Matthew Bartnof[8], Carlos G. Torres-Castanedo[4], Halleh B. Balch[9, 12, 13], Matthew S. Rahn[4], Nathan P. Bradshaw[4], Edon Vitaku[1], David W. Burke[1], Hong Li[6, 7, 10], Michael J. Bedzyk[4, 11], Feng Wang[9, 12, 13], Jean-Luc Brédas[5, 6, 10], Jonathan A. Malen[8, 14], Alan J. H. McGaughey[8, 14], Mark C. Hersam[1, 4, 15, 16],William R. Dichtel[1*], Patrick E. Hopkins[2, 17, 18*]

[1]Department of Chemistry, Northwestern University, Evanston, IL, 60208
[2]Department of Mechanical and Aerospace Engineering, University of Virginia, VA, 22904
[3]Department of Mechanical, Industrial and Systems Engineering, University of Rhode Island, Kingston, RI, 02881
[4]Department of Materials Science and Engineering, Northwestern University, Evanston, IL, 60208
[5]School of Chemistry and Biochemistry, Georgia Institute of Technology, Atlanta, GA 30332
[6]Center for Organic Photonics and Electronics, Georgia Institute of Technology, Atlanta, GA 30332
[7]College of Environmental Science and Engineering, Hunan University, Changsha, P. R. China, 410082
[8]Department of Mechanical Engineering, Carnegie Mellon University, Pittsburgh, PA, USA, 15213
[9]Department of Physics, University of California Berkeley, Berkeley, CA, USA, 94701
[10]Department of Chemistry and Biochemistry, The University of Arizona, Tucson, Arizona, USA, 85721
[11]Department of Physics and Astronomy, Northwestern University, Evanston, IL, 60208
[12]Kavli Energy Nanosciences Institute, University of California Berkeley, Berkeley, CA, USA 94701
[13]Materials Science Division, Lawrence Berkeley National Laboratory, Berkeley, CA, 94701
[14]Department of Materials Science and Engineering, Carnegie Mellon University, Pittsburgh, PA, USA, 15213
[15]Department of Electrical and Computer Engineering, Northwestern University, Evanston, IL, USA 60208
[16]Simpson Querrey Institute, Northwestern University, Evanston, IL, USA 60208
[17]Department of Physics University of Virginia, VA, 22904
[18]Department of Materials Science and Engineering, University of Virginia, VA, 22904

[ǂ]These authors contributed equally to this work

Correspondence Addresses

Professor William R. Dichtel
Department of Chemistry
Northwestern University
2045 Sheridan Road
Evanston, IL 60208 , USA
wdichtel@northwestern.edu

Professor Patrick E. Hopkins
Department of Mechanical and Aerospace Engineering
Department of Materials Science and Engineering,
Department of Physics,
University of Virginia
Charlottesville, VA 22904, USA
phopkins@virginia.edu

Table of Contents

A. Materials and Methods

Materials

All monomers, solvents, and catalysts were either purchased from commercial sources or prepared following literature reported protocols. All materials were used as received without further purification. Anhydrous THF was obtained from a solvent purification system (JC Myer System).

Instrumentation

Nuclear Magnetic Resonance. ^{1}H NMR spectra were acquired on a 400 MHz Agilent DD MR-400 system or Bruker Avance III 500 MHz spectrometer and recorded at 25 °C. All chemical shifts were calibrated using residual solvent as internal reference ($CDCl_3$: 7.26 ppm for ^{1}H NMR. DMSO: 2.5 ppm for ^{1}H NMR).

Grazing-Incidence X-ray Diffractions. GIWAXS measurements were performed at either:

Advanced Photon Source at Argonne National Laboratory using the 8-ID-E Beamline under vacuum. All measurements were conducted with an incidence angle of 0.14° using 10.92 keV (λ = 1.135 Å) X-rays. The scattered photons were recorded on a Pilatus 1 M detector located 228 mm from the sample. Exposure times were varied such that the pixel with maximum counts was at 80% of saturation. In some cases, significant silicon substrate scatter was observed. The raw images were merged, pixel coordinates were transformed to q-space, and line cuts were generated using GIXSGUI for Matlab.[1]

or

Advanced Light Source-Lawrence Berkeley National Laboratory using Beamline Station 7.3.3 under a He atmosphere. A photon energy of 10 keV (λ = 1.24 Å). Data was collected by a Pilatus 2M detector with a pixel size of 0.172 × 0.172 mm and 1475 × 1679 pixels used to capture the 2D scattering patterns at a distance of 300 mm from the sample. A silver behenate standard was used as a calibrant. The grazing angle, α, was varied from 0.08° to 0.25°. Data were analyzed using the Nika macro for Igor Pro.[2]

All data is shown as a function of the scattering vector:

$$Q = \frac{4\pi}{\lambda}\sin(\theta) \qquad (1)$$

Simulated X-ray Diffraction. Simulations of 2D COF X-ray scattering profiles were carried out in MaterialsStudio (ver.5.0). First, the unit cell was constructed piecewise in a primitive P6 unit cell with the *a=b* lattice parameter set to be approximately the distance between two COF vertices based on approximate molecular bond lengths. The *c* parameter was set to be 3.5 Å, which is the interlayer spacing of graphene. We then used a Forcite geometry optimization routine with a universal forcefield to optimize the unit cell size with convergence tolerances of

Energy = 10^{-3} kcal mol^{-1} and Force = 0.5 kcal mol^{-1} $Å^{-1}$.

Diffraction simulation and Pawley refinement were carried out using the Reflex software package. COF models and their simulated patterns were Pawley refined to experimental patterns iteratively until the RWP value converges. The pseudo-Voigt profile function was used for whole profile fitting. The final RWP and RP values were calculated to be less than 5% in all cases. Simulated XRD patterns were calculated from the refined unit cell and compared with the experimentally observed patterns.

X-ray Reflectivity. XRR measurements were carried out using a Rigaku ATXG diffractometer equipped with an 18 kW Cu rotating anode (λ = 1.5418 Å) operating at a voltage of 50 kV and a current of 240 mA, with a collimated beam of 0.1 mm x 2 mm (0.2 mm^2). All measurements are plotted in terms of the scattering vector *Q* (Eq. 1), normalized to the measured incident beam intensity, and corrected for geometrical footprint and background signal. The XRR analysis was performed using Motofit software.[3] Three different systems were studied: COF-5/EG/SiC, COF-5/EG/SiO_2/Si and Al_2O_3/COF-5/EG/SiO_2/Si. The fittings show a well-resolved electron density profile which confirms no intermixing or degradation of the COF-5 film. All the electron densities correspond to the expected bulk-like values. The electron density for the COF-5 film was a free parameter determined from the fit. The fitting parameters are included in the tables. The fit determined electron density profiles are shown as insets in each of the XRR figures.

Fluorescence Spectroscopy. Emission and excitation spectra were recorded on a Horiba Jobin Yvon Fluorolog-3 fluorescence spectrophotometer equipped with a 450 W Xe lamp, emission and excitation polarizer, double excitation and double emission monochromators, a digital photon-counting photomultiplier and a secondary InGaAs detector for the NIR range. Correction for variations in lamp intensity over time and wavelength was achieved using a solid-state silicon photodiode as the reference. The spectra were further corrected for variations in photomultiplier response over wavelength and for the path difference between the sample and the reference by multiplication with emission correction curves generated on the instrument. To collect emission spectra of the 2D COF films, films were mounted in a proprietary film holder. When emission polarization was noted as "normalized", we divided the intensity of all emission intensities by the maximum emission intensity.

Atomic Force Microscopy. Atomic force microscopy (AFM) was conducted using the facilities at the Northwestern Atomic and Nanoscale Characterization Experiment Center (NUANCE) on a SPID Bruker FastScan AFM using a gold tip under the non-contact mode in air. To prepare films for imaging, they were scored with a pair of Teflon-coated forceps so as to not damage the underlying Si. These films were then imaged across the score to evaluate their thickness and roughness.

Scanning Electron Microscopy. 2D COF films were cleaved and mounted with carbon tape or double-sided copper taper on vertical SEM mounts. Each sample was coated with 7 nm of Os (SPI Osmium Coater, with OsO_4 as a volatile source) to create a conformal conductive coating prior to imaging. Images were collected with a Hitachi SU 8030 scanning electron

microscope with an acceleration voltage of 5 kV at a magnification of 80,000.

Preparation of epitaxial graphene on SiC. Epitaxial graphene was grown on 4H-SiC(0001) wafers (Cree, Inc.) by ultra-high vacuum (UHV) annealing. The SiC wafers were diced into 5x9 mm rectangles (American Precision Dicing, Inc.) and the resulting substrates were first degreased via sonication in acetone and isopropanol before being introduced into the UHV chamber with base pressure ~$5 \cdot 10^{-11}$ Torr. Substrates were degassed for 12 hours at 500 °C prior to graphitization at 1200 °C for 20 minutes while maintaining chamber pressure below $5 \cdot 10^{-8}$ Torr. During annealing, substrate temperature was monitored using an infrared pyrometer ($\varepsilon = 0.85$).

Capacitor Fabrication and Characterization. First, atomic layer deposition (ALD) was used to grow Al_2O_3 on COF-coated EG-SiC substrates using a Savannah S100 ALD reactor (Cambridge Nanotech, Cambridge MA). The substrates were loaded into the chamber pre-heated to 100 Å. The base pressure of the chamber was maintained at 0.8 Torr with a constant N_2 flow rate of 20 sccm. The growth was done at 100 Å by exposing samples to sequential doses of the metal oxide precursor (trimethyl aluminum (TMA), Aldrich, 99%) and deionized water interspersed with dry N_2 purge steps between each precursor dose. For Al_2O_3 growth, a single ALD cycle consisted of a TMA pulse for 0.015 s and a 30 s purge, followed by a H_2O pulse for 0.015 s and a second 30 s purge. During growth, TMA precursor bottles were kept at room temperature. An approximately 6-nm-thick Al_2O_3 was grown on COF layer by using 75 pulses of TMA using 0.8 Å/cycle growth rate, as verified independently for atomic force microscopy and ellipsometry. The thickness of Al_2O_3/COF-5 dielectric bilayer was extracted from topography images (Figure 3c,d) using tapping mode in an Asylum Cypher AFM system.

Parallel plate capacitors were completed by growing 100-nm-thick Au films on Al_2O_3/COF-5 dielectric bilayer using a thermal evaporator (Nano38, Kurt J. Lesker Company). The evaporation was done through a shadow mask with rectangular holes of 100 μm x 100 μm using a growth rate of 1 Å/sec.

Impedance Measurements.
Impedance measurements were carried out by a Solartron 1260 impedance analyzer using an AC amplitude of 100 mV in a frequency range of 100 Hz to 10 kHz. This frequency range was chosen because the signal was too noisy below 100 Hz and series resistance from the SiC wafer interfered with measurements above 10 kHz. Au pads were contacted by tungsten cat whisker soft-probes (Signatone, SE-SM) to avoid puncturing the COF dielectric. Capacitance-frequency (C-f) measurements were performed at zero dc bias, and capacitance-voltage (C-V) measurements were conducted at 1 kHz. Capacitance values were verified independently using the C-V module of a 4200 Semiconductor Characterization System (SCS), Keithley Instruments. Leakage measurements were also carried by the 4200 SCS system using a remote current preamplifier. Impedance data was analyzed by model fitting using ZPlot/ZView software from Scribner Associates, Inc.

B. Monomer Synthetic Procedures

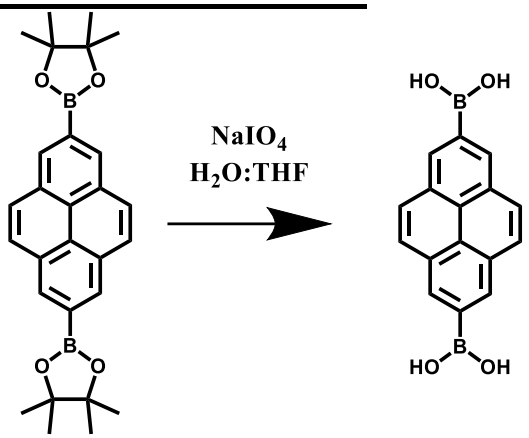

Scheme S1. Synthesis of 2,7-pyrenebisboronic acid (PyBA)

Synthesis of 2,7-pyrenebisboronic acid. PyBA was prepared by an adaptation of a previously reported synthesis.[4] A THF:H_2O mixture (300 mL, 4:1 vol) of pyrene-2,7-diboronicester (5g, 11 mmol, 1.0 equiv.) and $NaIO_4$ (3.5 g, 27.5 mmol, 2.5 equiv.) was prepared in a 500 mL RBF and stirred at room temperature for 16 hrs under N_2. During the course of this reaction, a white precipitate was formed. The reaction mixture was then diluted with H_2O (300 mL) and filtered. During filtration, the product was washed with an additional 300 mL of H_2O, taking care to not allow the product to dry completely on the filter paper. The product was then flushed with hexanes and dried, which produced a white powder (2.6 g, 81%). ^{1}H NMR analysis of this product was consistent with a previous report.[4]

^{1}H NMR (400 MHz, DMSO-d_6, 298 K): δ ppm 8.68 (4H, s, 1,3,6,7-H-pyrene), 8.44 (4H, s, 4,5,9,10-H-pyrene), 8.16 (4H, s, BO–H)

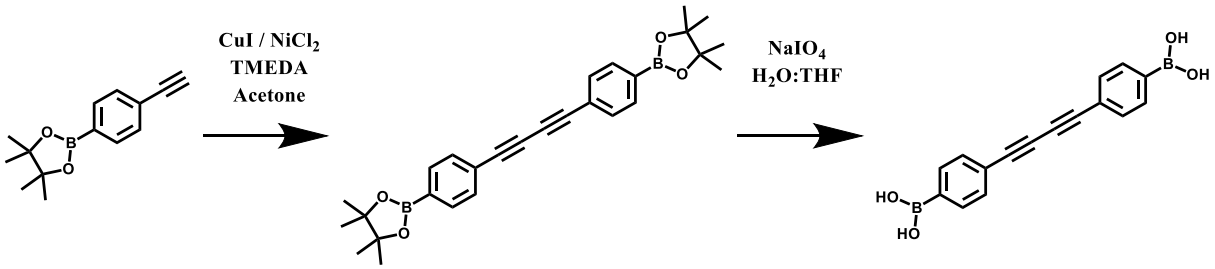

Scheme S2. Synthesis of 4,4′-diphenylbutadiynebis(boronic acid)

Synthesis of 4,4′-diphenylbutadiynebis(pinacolborane). The synthesis of this product was adapted from a previous report.[5] A 100 mL round bottom flask was charged with CuI (0.752 g, 3.94 mmol, .05 equiv.), NiCl2● 6H_2O (0.936 g, 3.94 mmol, .05 equiv.), and tetramethylethylenediamine (TMEDA) (1.836 g, 15.784 mmol, 0.25 equiv.). Acetone (50 mL) was added, and as the solids dissolved the mixture became dark green. 4-ethynylbenzeneboronic acid pinacole ester (18 g, 78.8 mmol, 1.0 equiv.) was added to this mixture, which was then stirred for 16 hours. The solvent was removed by rotary evaporation to yield a green residue that was washed with H_2O (300 mL). The resultant solid was isolated via filtration through a Büchener funnel. This solid was subsequently recrystallized from CH_3CN as a white solid, collected via filtration through a Büchener funnel, and dried under vacuum (5.25 g, 12 mmol, 30 %). ^{1}H NMR analysis of this product was consistent with a previous report.[5]

^{1}H-NMR ($CDCl_3$, 400 MHz, 298 K) δ 7.65 (d, J = 9.0 Hz, 4H); 7.52 (d, J = 9.0 Hz, 4H); 1.34 (s, 24H).

Synthesis of 4,4′-diphenylbutadiynebis(boronic acid). The synthesis of this compound was adapted from a previous report.[5] In a 20 mL scintillation vial, 4,4'-diphenylbutadiyne pinacole borane (1.00 g, 2.20 mmol, 1.00 equiv.) and sodium periodate (1.0 g, 5.00 mmol, 2.27 equiv.) were dissolved in THF:H2O (4:1 v/v, 30 mL). This mixture was stirred at room temperature with nitrogen actively bubbling through it for 30 minutes, after which 1M HCl (5 mL) was added via syringe. The reaction vessel was subsequently sealed and allowed to stir for an additional 24 hours. At this point, the reaction mixture was poured into 100 mL of H_2O, filtered through a Büchener funnel, and washed with an additional 100 mL of H_2O. This product was then flushed with 100 mL of diethyl ether. This powder was dried under vacuum for 10 minutes to afford a fine white powder (444 mg, 1.5 mmol, 69%). ^{1}H NMR analysis of this product was consistent with a previous report.[5]

^{1}H-NMR (DMSO-d_6, 400 MHz, 298 K) δ 8.26 (s, 4H); 7.82 (d, J = 7.5 Hz, 4H); 7.57 (d, J = 7.5 Hz, 4H).

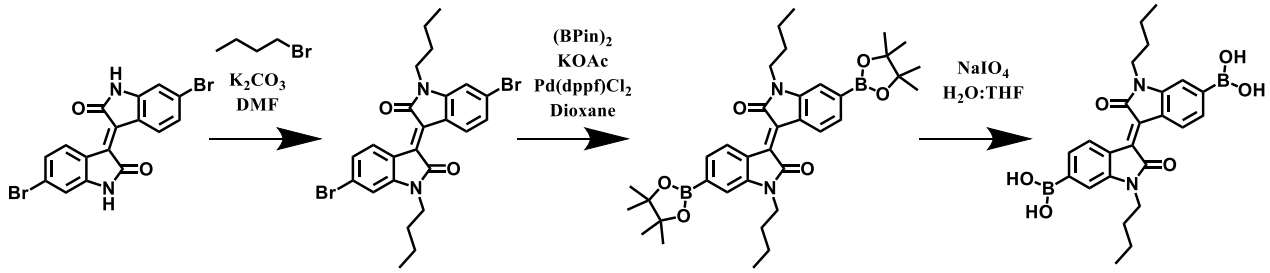

Scheme S3. Synthesis of N,N'-dihexyl-6,6'-isoindigobis(boronic acid)

Synthesis of *N,N*'-dibutyl-6,6'-bisbromoisoindigo. To a flame-dried 300 mL RBF, dibromoisoinidio (750 mg, 1.785 mmol, 1.0 equiv.), K_2CO_3 (1.65 g, 11.90 mmol, 6.67 equiv.), and DMF (32 mL) were added. Then, butylbromide (0.56 mL, 5.24 mmol, 2.93 equiv.) was added via syringe and heated to 110 °C. After 14 hours, the reaction mixture was cooled to room temperature and quenched with saturated NH_4Cl. The product was then extracted with EtOAc (2 X 100 mL). These fractions were then combined, washed with water (5 X 100 mL) and brine (2 X 100 mL). The organic fraction was then collected, dried with anhydrous $MgSO_4$, filtered, and concentrated *in vacuo* to give *N,N*'-dihexyl-6,6'-bisbromoisoindigo as a deep red product (590 mg, 1.1 mmol, 62%). ^{1}H NMR analysis of this product was consistent with a previous report.[6]

^{1}H NMR (400 MHz, cdcl$_3$) δ 9.07 (d, *J* = 8.6 Hz, 1H), 7.17 (dd, *J* = 8.6, 1.9 Hz, 1H), 6.93 (d, *J* = 1.9 Hz, 1H), 3.74 (t, *J* = 7.4 Hz, 2H), 1.66 (d, *J* = 7.4 Hz, 2H), 1.41 (d, *J* = 7.8 Hz, 2H), 0.97 (t, *J* = 7.4 Hz, 3H).

Synthesis of *N,N*'-dibutyl-6,6'-isoindigobis(pinacolborane). The following were added to a 50 mL Schlenk flask: N,N'-dihexyl-6,6'-bisbromoisoindigo (500 mg, 0.94 mmol, 1.0 equiv.), $(BPin)_2$ (596 mg, 2.35 mmol, 2.5 equiv), KOAc (332 mg, 3.38 mmol, 3.6 equiv.), $Pd(dppf)Cl_2•CH_2Cl_2$ (80 mg, 0.09 mmol, 0.10 equiv.), and 1,4-dioxane (8 mL). This flask was then closed with a septum and degassed under constant N_2 flow for 15 min. The reaction mixture was then heated at 80 °C for 40 hrs. Then, the reaction was cooled to room temperature and diluted with CH_2Cl_2. This mixture was then passed through a silica gel plug on a fritted funnel and washed with CH_2Cl_2. The filtrate was then concentrated *in vacuo* to yield a sticky red residue, which was mixed with MeOH (15 mL) and placed in a freezer. After 2 hrs, the precipitate was collected and dried to give *N,N*'-dihexyl-6,6'-isoindigobis(pinacolborane) as a deep red product (510 mg, .82 mmol, 87%). ^{1}H NMR analysis of this product was consistent with a previous report.[6]

^{1}H NMR (499 MHz, cdcl$_3$) δ 9.15 (d, *J* = 7.9 Hz, 1H), 7.49 (dd, *J* = 7.9, 1.1 Hz, 1H), 7.15 (s, 1H), 3.81 (t, *J* = 7.4 Hz, 2H), 1.73 – 1.68 (m, 2H), 1.46 – 1.41 (m, 2H), 1.37 (s, 12H), 0.97 (t, *J* = 7.4 Hz, 3H).

Synthesis of *N,N*'-dibutyl-6,6'-isoindigobis(boronic acid). To a 20 mL scintillation vial *N,N*'-dihexyl-6,6'-isoindigobis(pinacolborane) (100 mg, 0.16 mmol, 1.0 equiv.), $NaIO_4$ (85 mg, 0.4 mmol, 2.5 equiv.), a THF:H_2O 4:1 vol. (15 mL) were added. The vial was then placed

under N_2. After 3 days, the reaction was diluted with H_2O (15 mL) and filtered while continuously adding water (50 mL), taking care to not let the product dry to completion on the filter paper. Finally, the product was washed with hexanes and dried under vacuum. This yielded *N*,*N*'-dihexyl-6,6'-isoindigobis(boronic acid) as a bright red solid (52 mg, .112 mmol, 70% yield). Reliable NMR analysis was not possible due to insolubility of the product.

C. Monomer Nuclear Magnetic Resonance

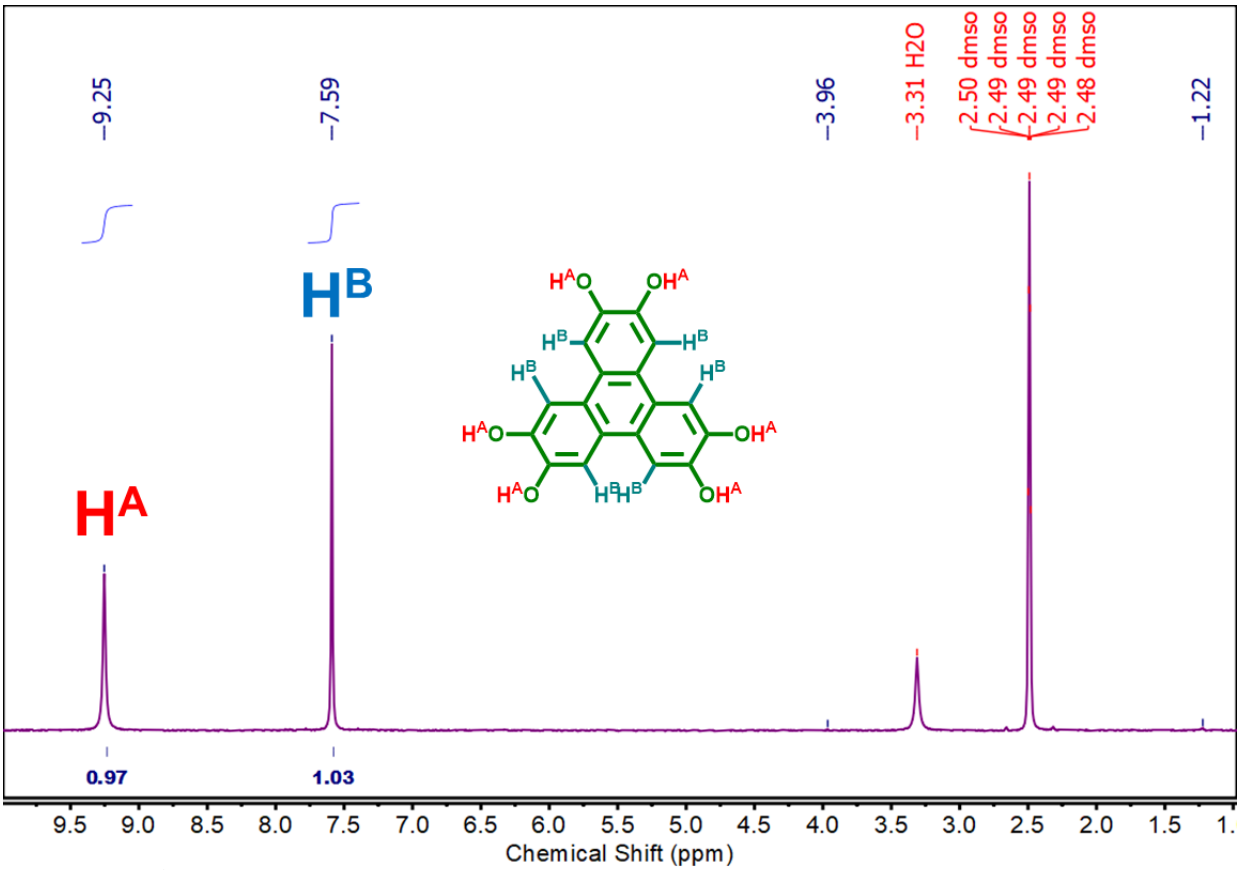

Figure S1. ^{1}H nuclear magnetic resonance spectra of 2,3,6,7,10,11-Hexahydroxytriphenylene Hydrate (HHTP), purchased from TCI America

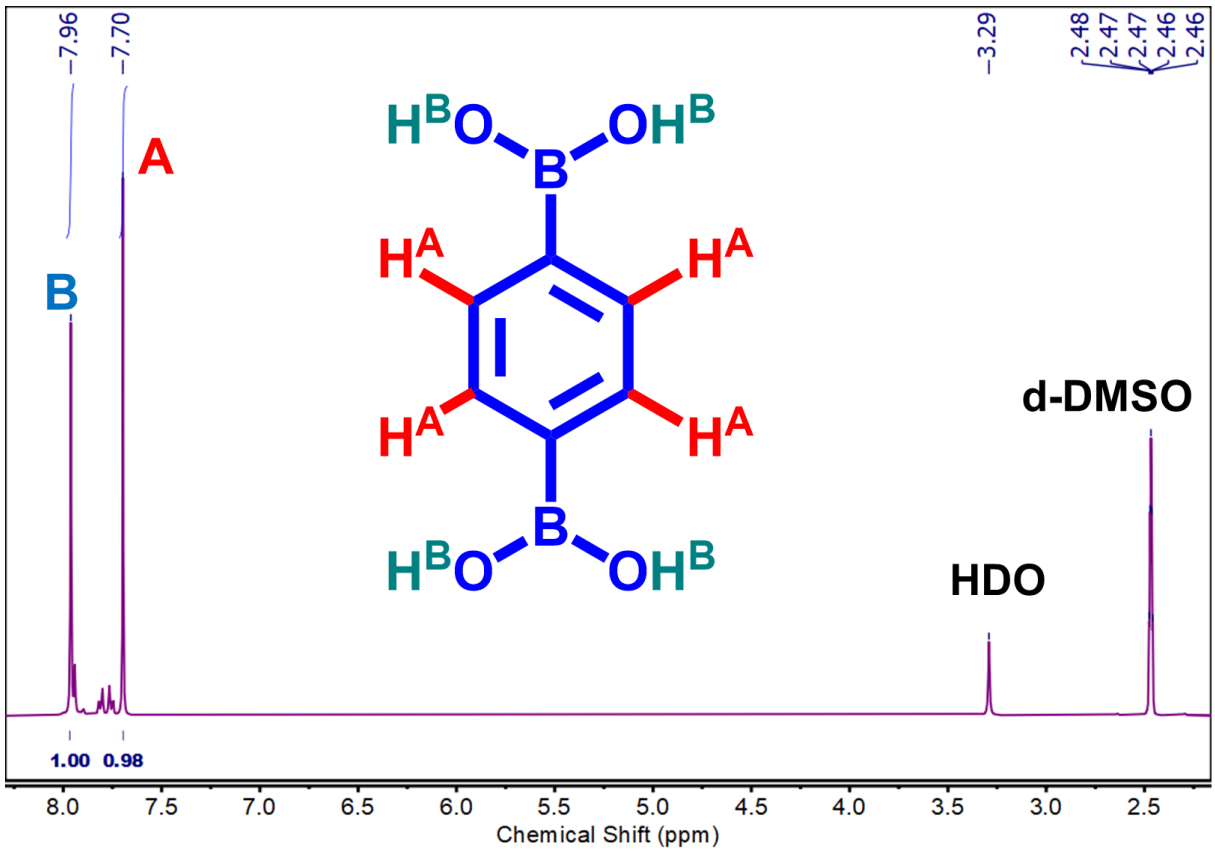

Figure S2. ^{1}H nuclear magnetic resonance spectra of 1,4-phenylenebisboronic acid (PBBA), purchased from Sigma Aldrich

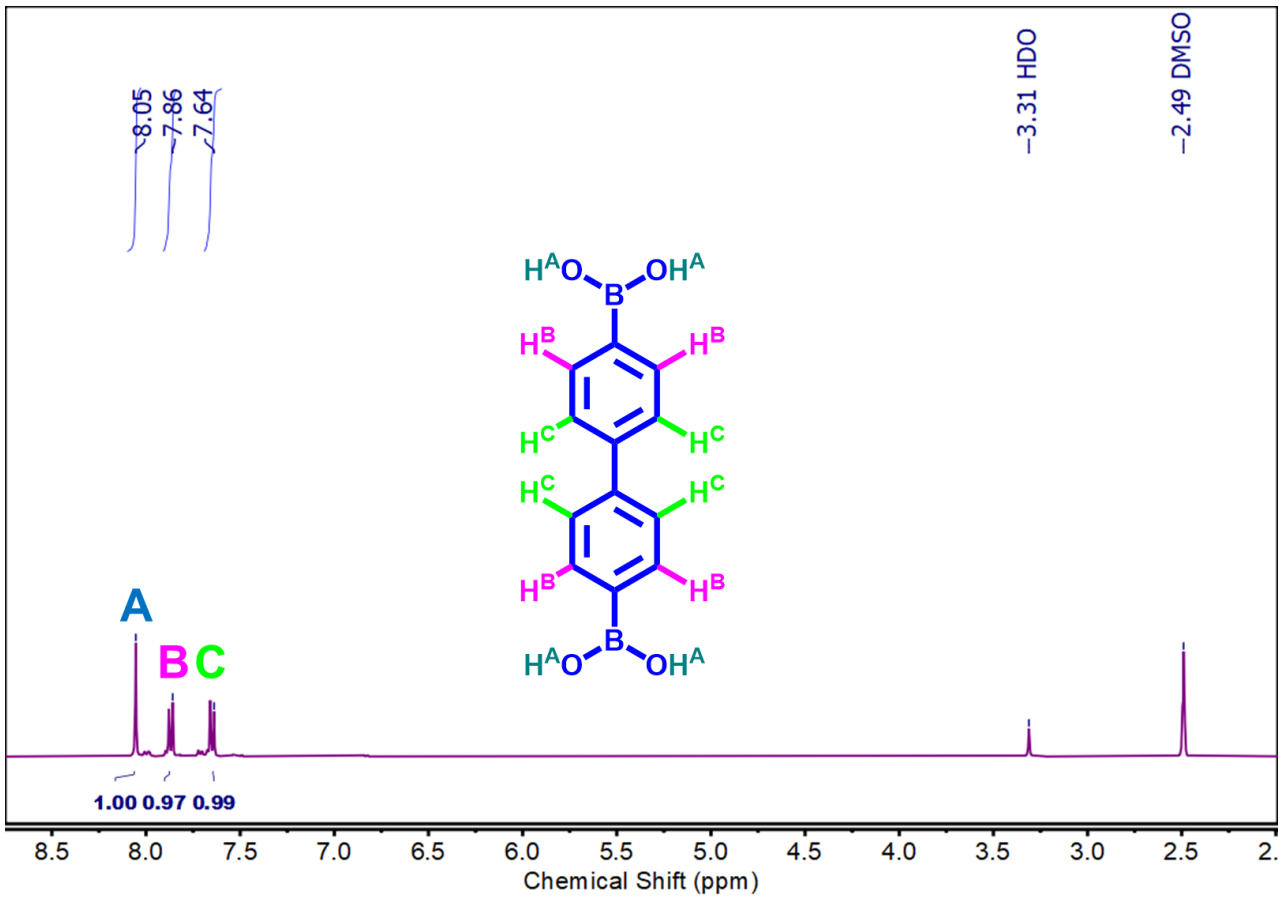

Figure S3. ^{1}H nuclear magnetic resonance spectra of 4,4'-biphenylbisboronic acid (BBBA), purchased from Sigma Aldrich

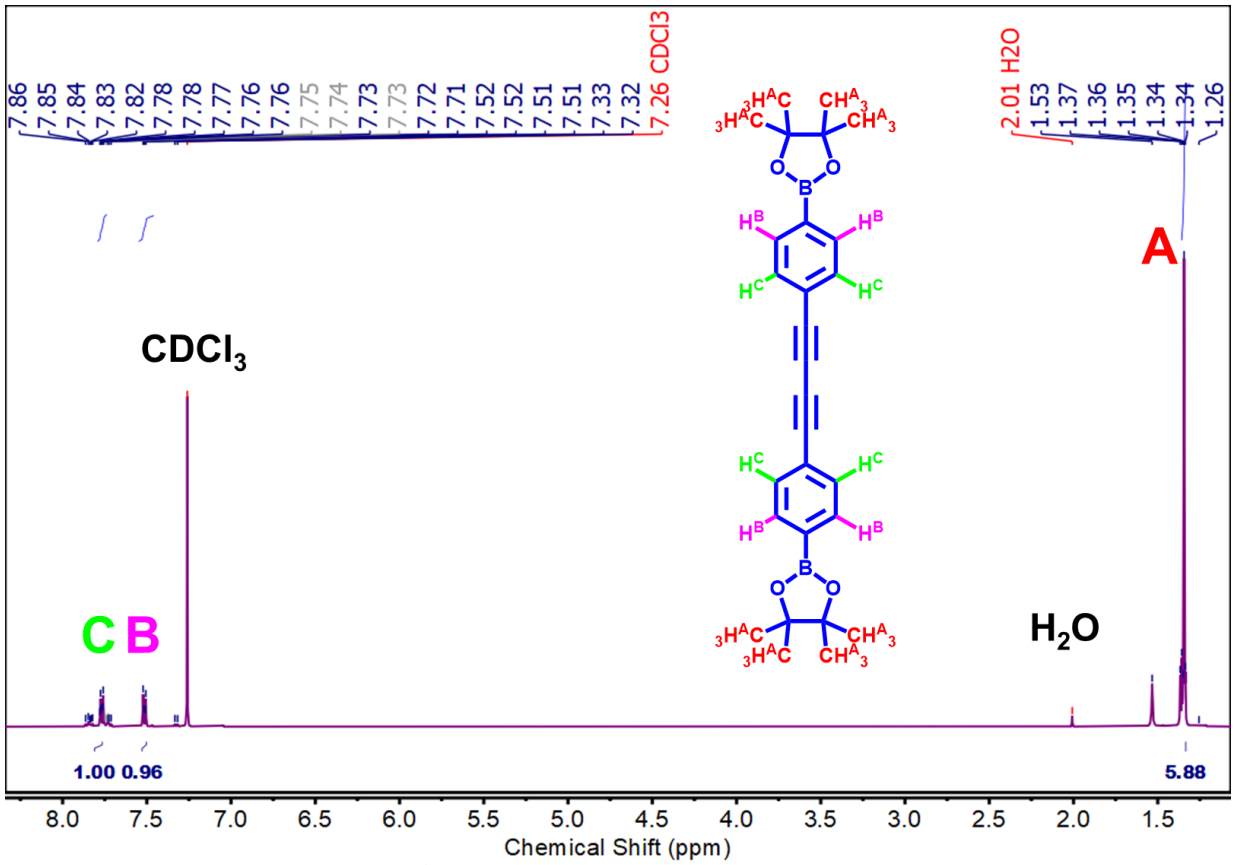

Figure S4. ^{1}H nuclear magnetic resonance spectra of 4,4′-diphenylbutadiynebis(pinacolborane)

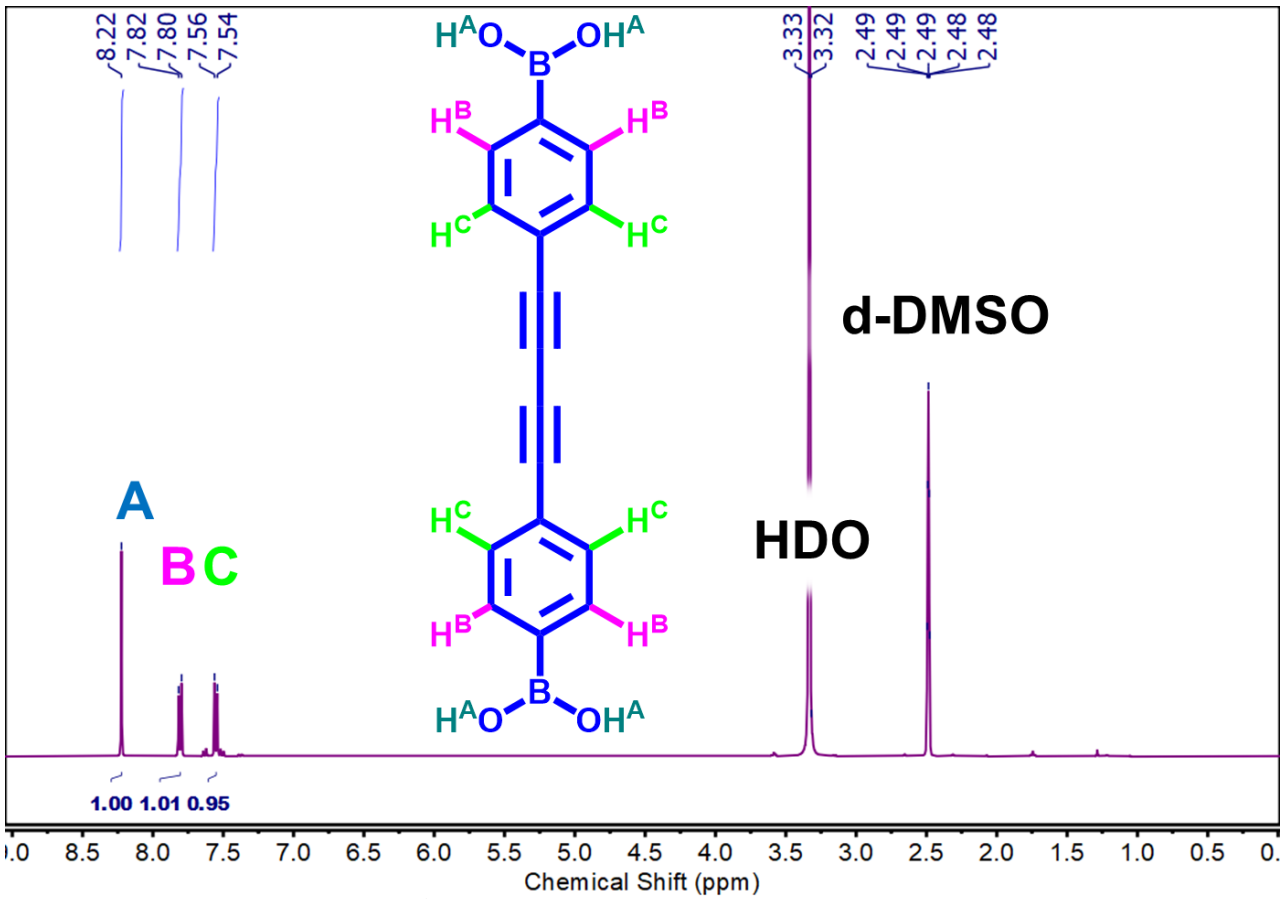

Figure S5. ^{1}H nuclear magnetic resonance spectra of 4,4′-diphenylbutadiynebis(boronic acid)

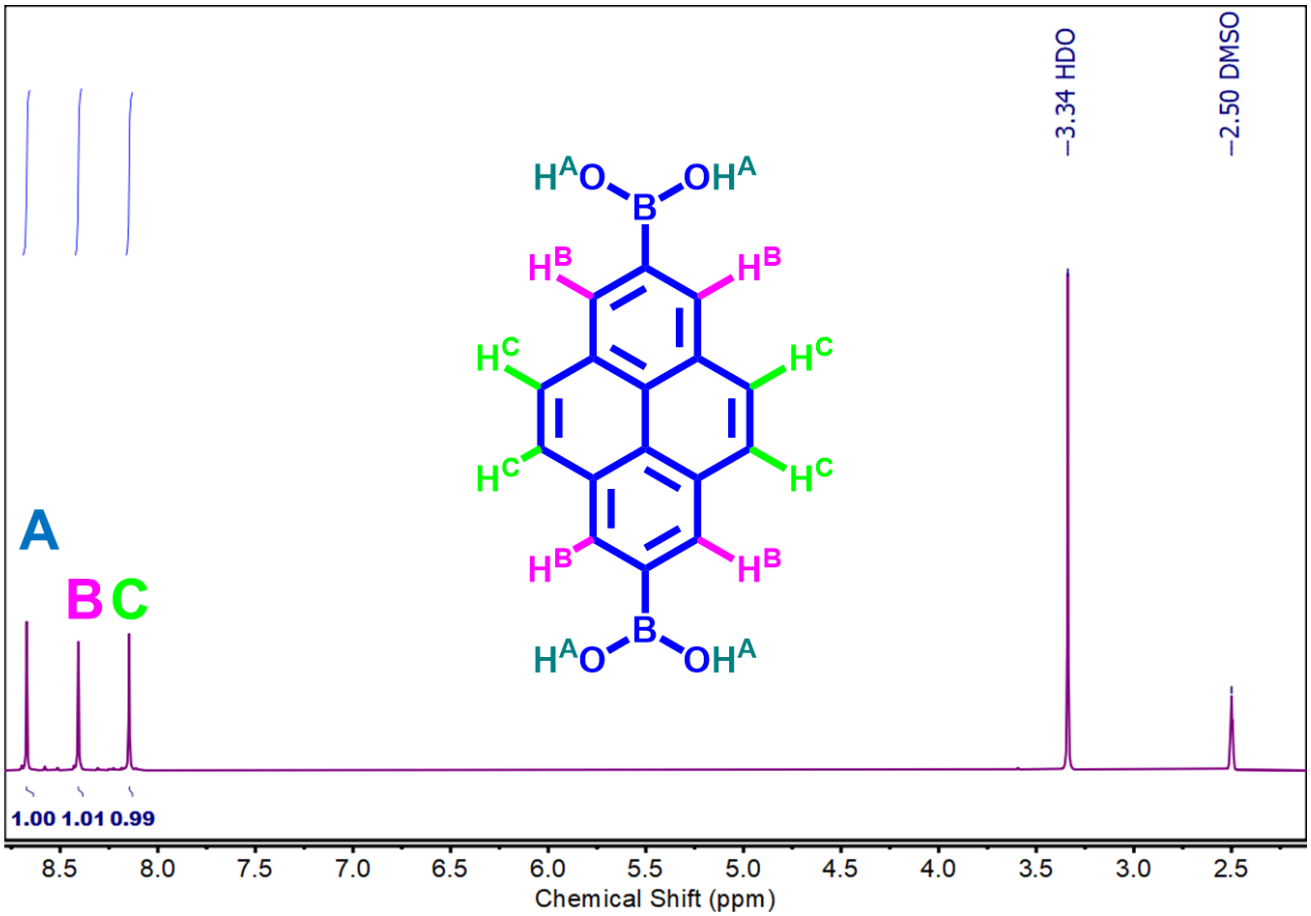

Figure S6. ^{1}H nuclear magnetic resonance spectra of 2,7-pyrenebis(boronic acid)

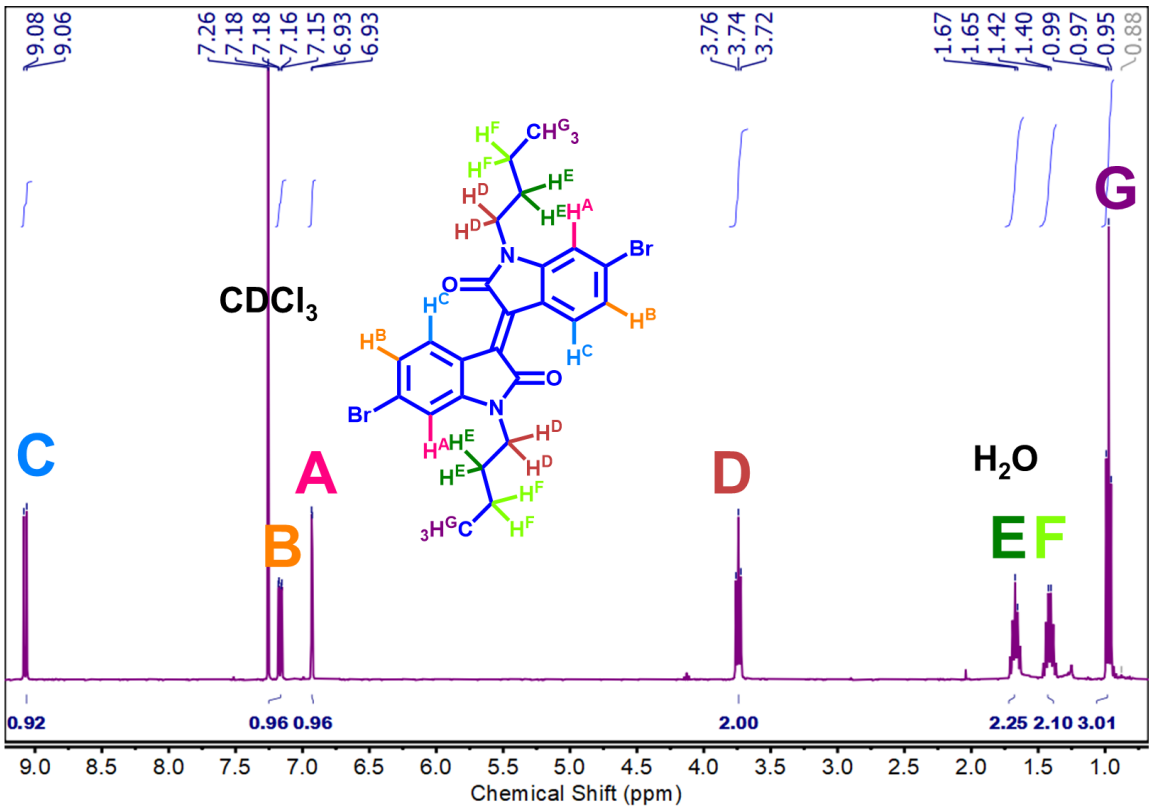

Figure S7. ^{1}H nuclear magnetic resonance spectra of *N*,*N*'-dibutyl-6,6'-bisbromoisoindigo

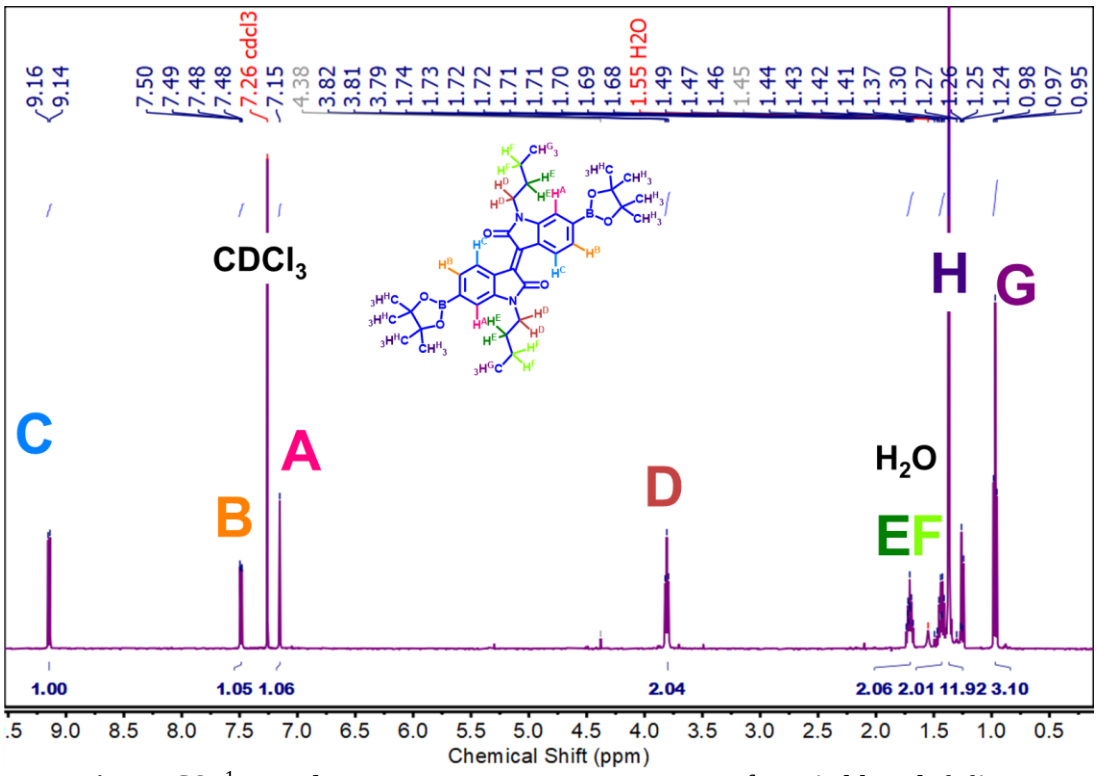

Figure S8. ^{1}H nuclear magnetic resonance spectra of *N*,*N*'-dibutyl-6,6'-bis(pinacolborane)isoindigo

D. 2D COF Film Synthetic Procedures

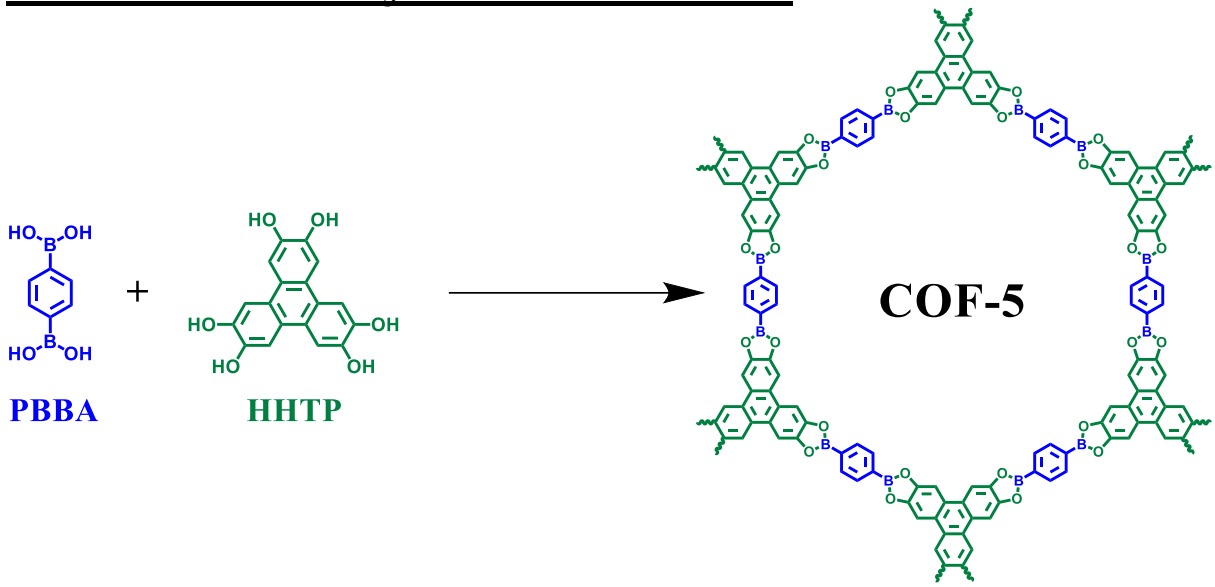

Figure S9. Synthesis of COF-5 Films

2D COF-5 Films. First, a graphene-coated Si/SiO_2 (1 cm X 1 cm, UniversityWafer, Inc.) was placed into a scintillation vial. Then, solutions of HHTP (2 mM) and PBBA (3 mM) were prepared separately in a solvent blend of 80/16/4 vol CH_3CN:1,4-dioxane:1,3,5-trimethylbenzene. These solutions were then filtered to remove any insoluble particulates. These solutions were then added in a 1:1 vol ratio to the substate-containing scintillation vial, producing a 20 mL solution of 1 mM HHTP and 1.5 mM PBBA. This scintillation vial was then sealed and heated to 80 °C for 24 hrs. After 24 hrs, a milky suspension had formed in the scintillation vial. Approximately 90% of the solution was then decanted and diluted with fresh 80/16/4 vol CH_3CN:1,4-dioxane:1,3,5-trimethylbenzene. This procedure was repeated 3 times to sufficiently dilute any colloidal species present in solution. The wafer was then removed from solvent with forceps and allowed to dry in air.

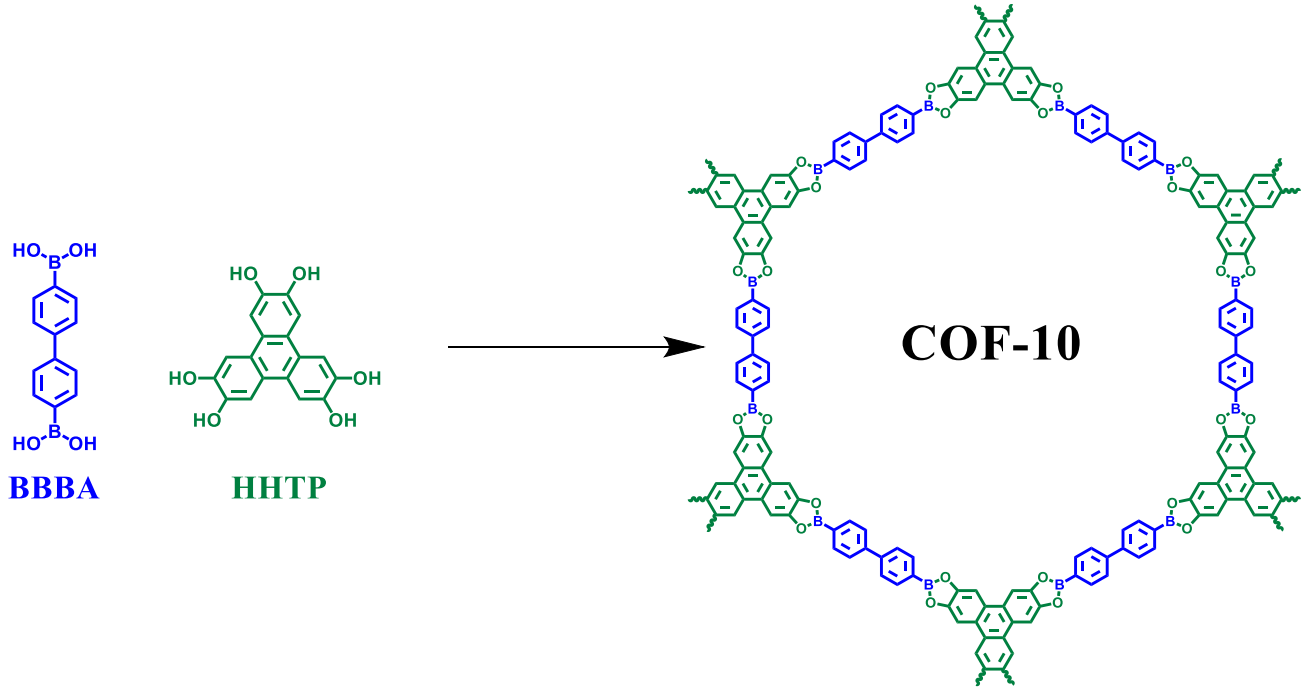

Figure S10. Synthesis of COF-10 Films

2D COF-10 Films. First, a graphene-coated Si/SiO_2 (1 cm X 1 cm, UniversityWafer, Inc.) was placed into a scintillation vial. Then, solutions of HHTP (2 mM) and BBBA (3 mM) were prepared separately in a solvent blend of 80/16/4 vol CH_3CN:1,4-dioxane:1,3,5-trimethylbenzene. These solutions were then filtered to remove any insoluble particulates. These solutions were then added in a 1:1 vol ratio to the substate-containing scintillation vial, producing a 20 mL solution of 1 mM HHTP and 1.5 mM BBBA. This scintillation vial was then sealed and heated to 80 °C for 24 hrs. After 24 hrs, a milky suspension had formed in the scintillation vial. Approximately 90% of the solution was then decanted and diluted with fresh 80/16/4 vol CH_3CN:1,4-dioxane:1,3,5-trimethylbenzene. This procedure was repeated 3 times to sufficiently dilute any colloidal species present in solution. The wafer was then removed from solvent with forceps and allowed to dry in air.

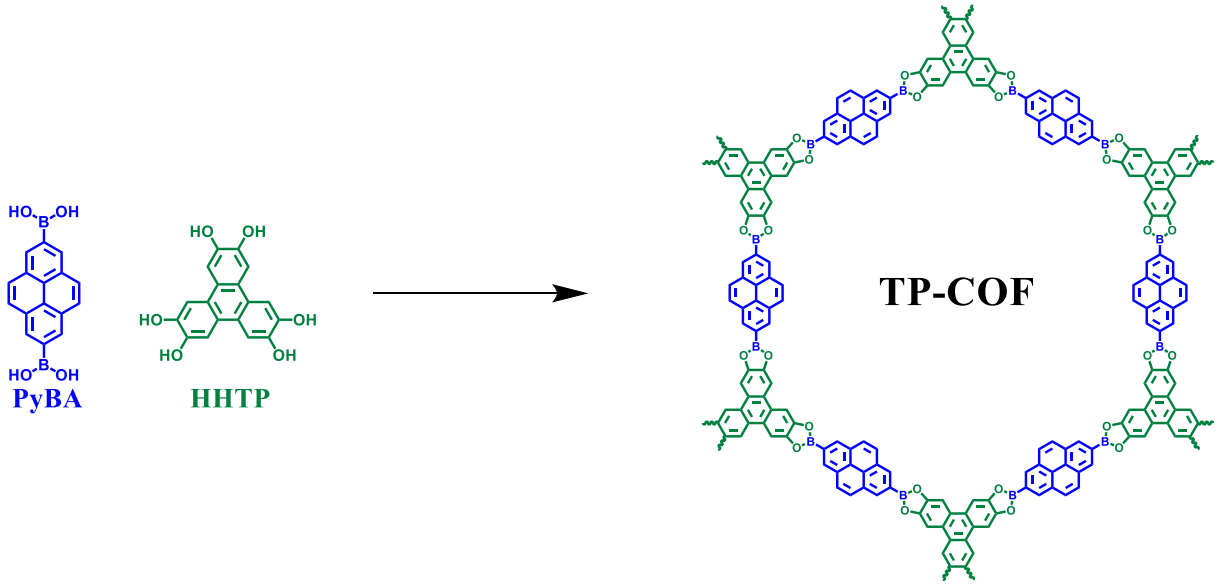

Figure S11. Synthesis of TP-COF Films

2D TP-COF Films. First, a graphene-coated Si/SiO_2 (1 cm X 1 cm, UniversityWafer, Inc.) was placed into a scintillation vial. Then, solutions of HHTP (2 mM) and PyBA (3 mM) were prepared separately in a solvent blend of 80/16/4 vol CH_3CN:1,4-dioxane:1,3,5-trimethylbenzene. These solutions were then filtered to remove any insoluble particulates. These solutions were then added in a 1:1 vol ratio to the substate-containing scintillation vial, producing a 20 mL solution of 1 mM HHTP and 1.5 mM PyBA. This scintillation vial was then sealed and heated to 80 °C for 24 hrs. After 24 hrs, a milky suspension had formed in the scintillation vial. Approximately 90% of the solution was then decanted and diluted with fresh 80/16/4 vol CH_3CN:1,4-dioxane:1,3,5-trimethylbenzene. This procedure was repeated 3 times to sufficiently dilute any colloidal species present in solution. The wafer was then removed from solvent with forceps and allowed to dry in air.

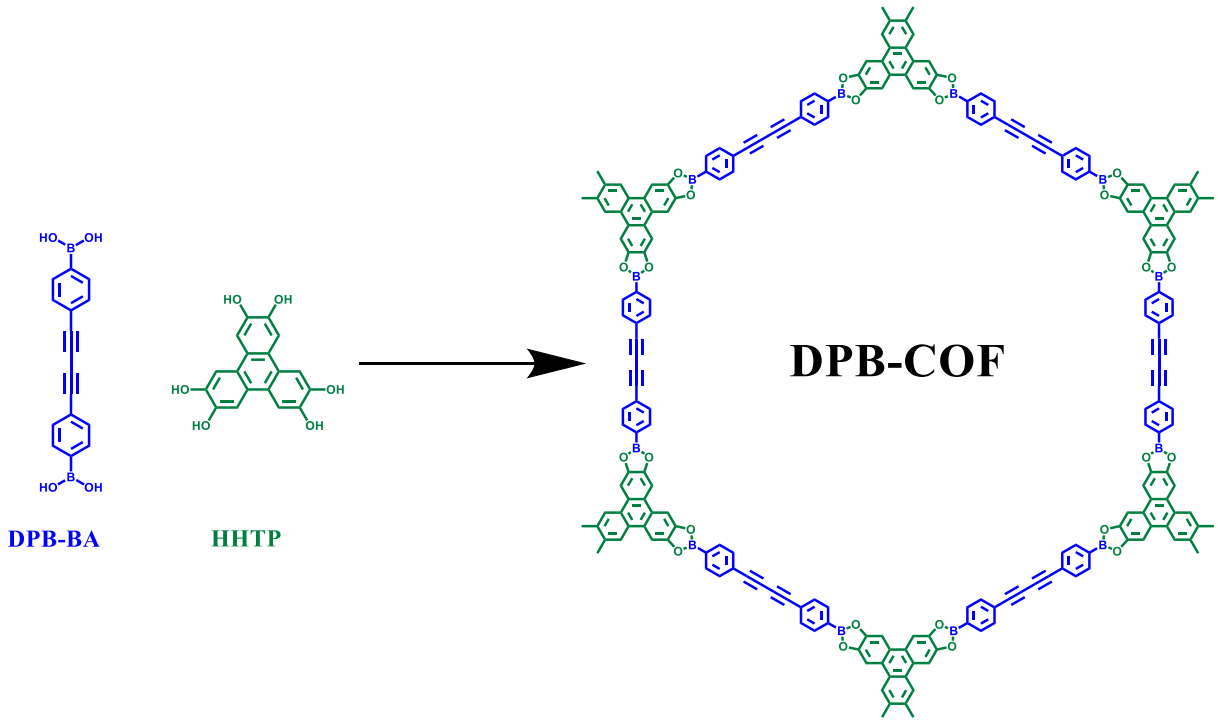

Figure S12. Synthesis of DPB-COF Films

2D DPB-COF Films. First, a graphene-coated Si/SiO_2 (1 cm X 1 cm, UniversityWafer, Inc.) was placed into a scintillation vial. Then, solutions of HHTP (2 mM) and DPB-BA (3 mM) were prepared separately in a solvent blend of 80/16/4 vol CH_3CN:1,4-dioxane:1,3,5-trimethylbenzene. These solutions were then filtered to remove any insoluble particulates. These solutions were then added in a 1:1 vol ratio to the substate-containing scintillation vial, producing a 20 mL solution of 1 mM HHTP and 1.5 mM DPB-BA. This scintillation vial was then sealed and heated to 80 °C for 24 hrs. After 24 hrs, a milky suspension had formed in the scintillation vial. Approximately 90% of the solution was then decanted and diluted with fresh 80/16/4 vol CH_3CN:1,4-dioxane:1,3,5-trimethylbenzene. This procedure was repeated 3 times to sufficiently dilute any colloidal species present in solution. The wafer was then removed from solvent with forceps and allowed to dry in air.

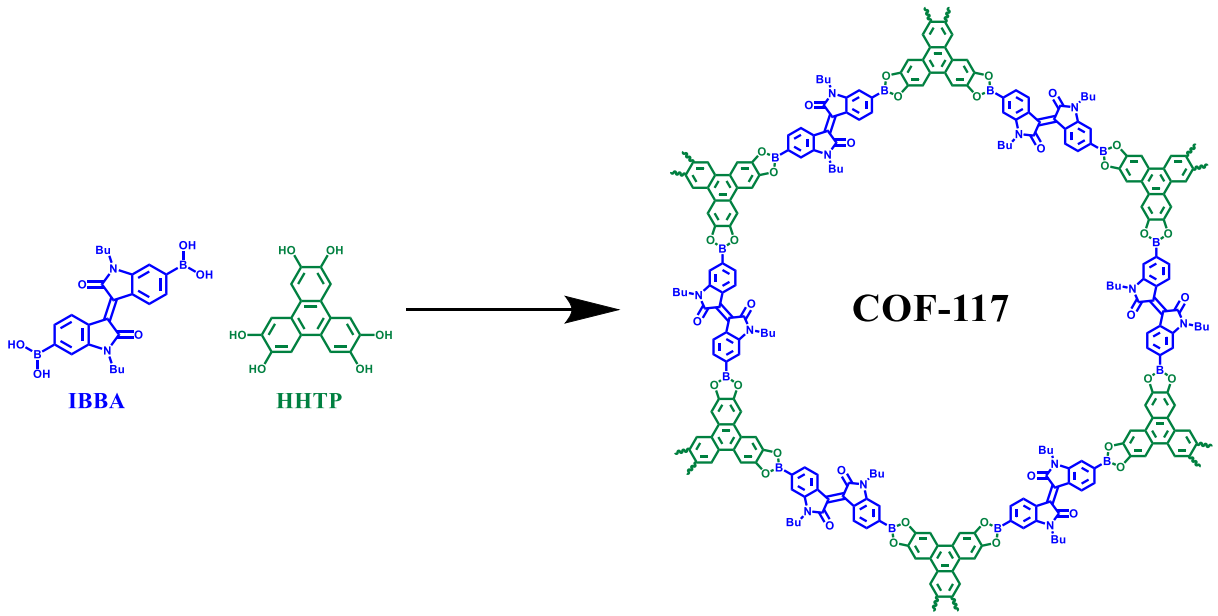

Figure S13. Synthesis of COF-117 Films

2D COF-117 Films. First, a graphene-coated Si/SiO_2 (1 cm X 1 cm, UniversityWafer, Inc.) was placed into a scintillation vial. Then, solutions of HHTP (2 mM) and IBBA (3 mM) were prepared separately in a solvent blend of 80/16/4 vol CH_3CN:1,4-dioxane:1,3,5-trimethylbenzene. These solutions were then filtered to remove any insoluble particulates. These solutions were then added in a 1:1 vol ratio to the substate-containing scintillation vial, producing a 20 mL solution of 1 mM HHTP and 1.5 mM IBBA. This scintillation vial was then sealed and heated to 80 °C for 24 hrs. After 24 hrs, a milky suspension had formed in the scintillation vial. Approximately 90% of the solution was then decanted and diluted with fresh 80/16/4 vol CH_3CN:1,4-dioxane:1,3,5-trimethylbenzene. This procedure was repeated 3 times to sufficiently dilute any colloidal species present in solution. The wafer was then removed from solvent with forceps and allowed to dry in air.

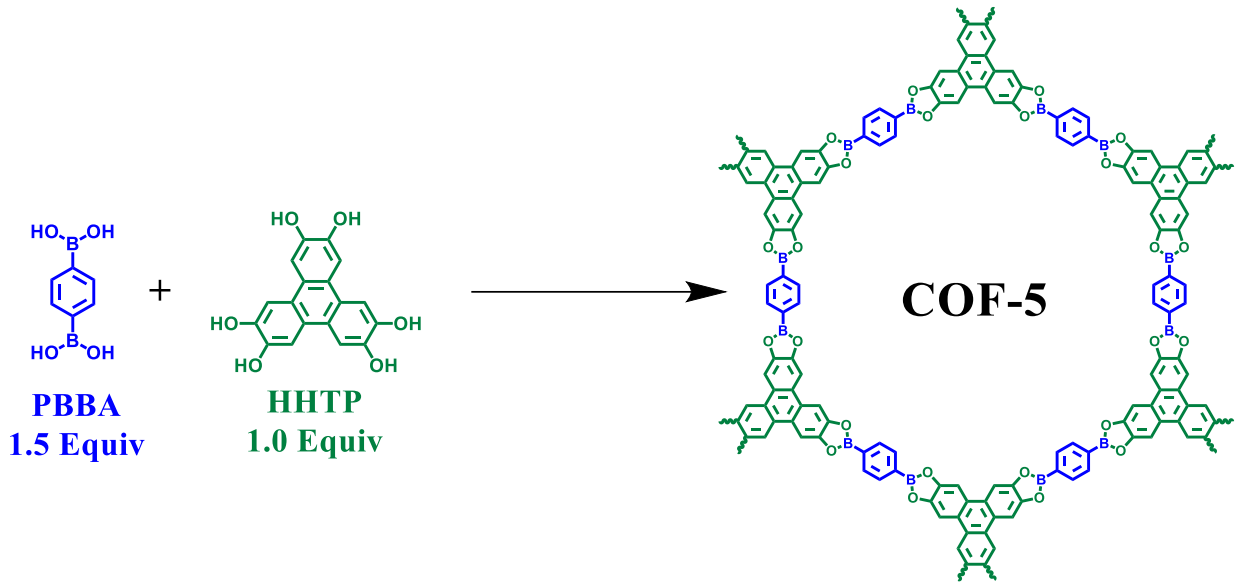

Figure S14. Synthesis of COF-5 Films at Higher Concentrations

2D COF-5 Films Prepared at Different Concentrations. First, a graphene-coated Si/SiO_2 (1 cm X 1 cm, UniversityWafer, Inc.) was placed into a scintillation vial. Then, solutions of HHTP (10 mM) and PBBA (15 mM) were prepared separately in a solvent blend of 80/16/4 vol CH_3CN:1,4-dioxane:1,3,5-trimethylbenzene. These solutions were then filtered to remove any insoluble particulates.

These solutions were then mixed in a 1:1 vol ratio, which was then diluted with additional 80/16/4 vol CH_3CN:1,4-dioxane:1,3,5-trimethylbenzene to yield solutions with HHTP concentrations of 5 mM (PBBA = 7.5 mM), 2 mM (PBBA = 3 mM), 1 mM (PBBA = 1.5 mM), and 0.5 mM (PBBA = 0.75 mM). These solutions were then added to the scintillation vial that contained the graphene-supported substrate. This scintillation vial was then sealed and heated to 80 °C for 24 hrs. After 24 hrs, a milky suspension had formed in the scintillation vial. Approximately 90% of the solution was then decanted and diluted with fresh 80/16/4 vol CH_3CN:1,4-dioxane:1,3,5-trimethylbenzene. This procedure was repeated 3 times to sufficiently dilute any colloidal species present in solution. The wafer was then removed from solvent with forceps and allowed to dry in air.

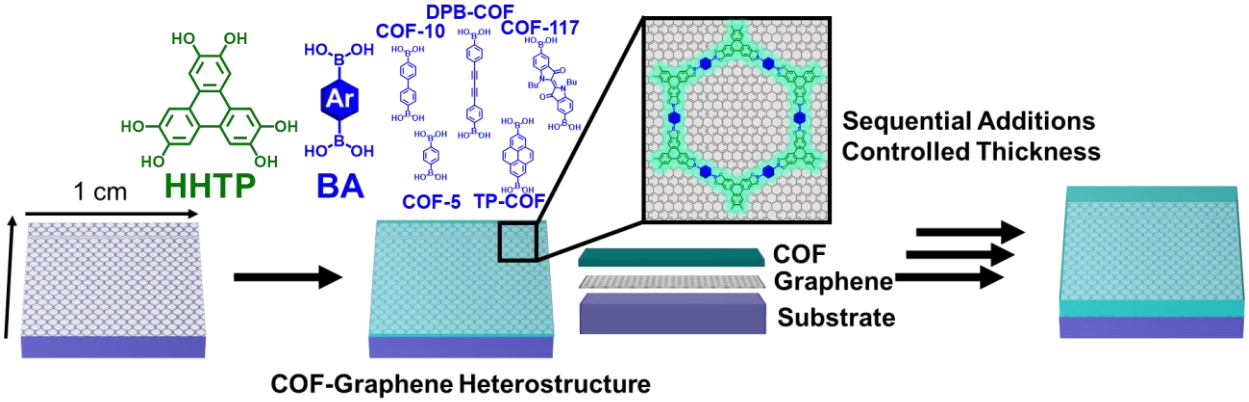

Figure S15. Multigrowth procedure of COF Films

Multigrowth COF Films. First, a graphene-coated Si/SiO_2 (1 cm X 1 cm, UniversityWafer, Inc.) was placed into a scintillation vial. Then, solutions of HHTP (2 mM) and corresponding boronic acid (3 mM) were prepared separately in a solvent blend of 80/16/4 vol CH_3CN:1,4-dioxane:1,3,5-trimethylbenzene. These solutions were then filtered to remove any insoluble particulates. These solutions were then mixed in a 1:1 vol ratio. This solution was then added to the scintillation vial that contained the graphene-supported substrate. This scintillation vial was then sealed and heated to 80 °C for 24 hrs. After 24 hrs, a milky suspension had formed in the scintillation vial. Approximately 90% of the solution was then decanted and diluted with fresh 80/16/4 vol CH_3CN:1,4-dioxane:1,3,5-trimethylbenzene. This procedure was repeated 3 times to sufficiently dilute any colloidal species present in solution.

Then, to instigate another round of growth, additional monomer species (prepared as described above) were added to the scintillation vial containing the wafer. This scintillation vial was then sealed and heated to 80 °C for 24 hrs. After 24 hrs, a milky suspension had formed in the scintillation vial. Approximately 90% of the solution was then decanted and diluted with fresh 80/16/4 vol CH_3CN:1,4-dioxane:1,3,5-trimethylbenzene. This procedure was repeated 3 times to sufficiently dilute any colloidal species present in solution.

This procedure was repeated for as many times as described. Finally, the wafer was removed from solvent with forceps and allowed to dry in air.

E. Optical Microscopy Images

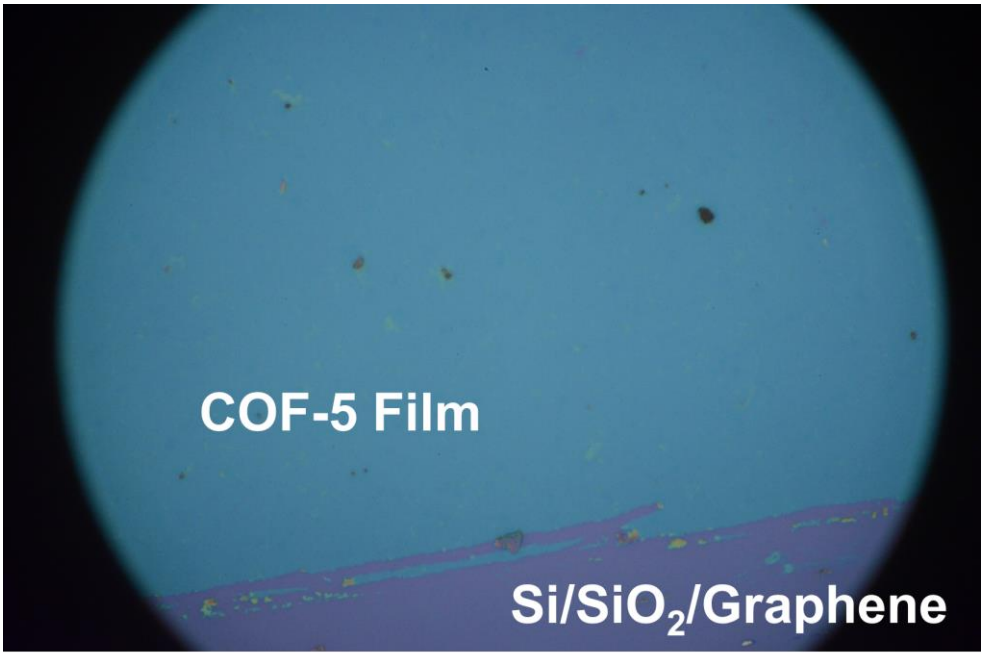

Figure S16. Optical Microscopy Image of COF-5/SiO_2/Si grown under colloidal conditions

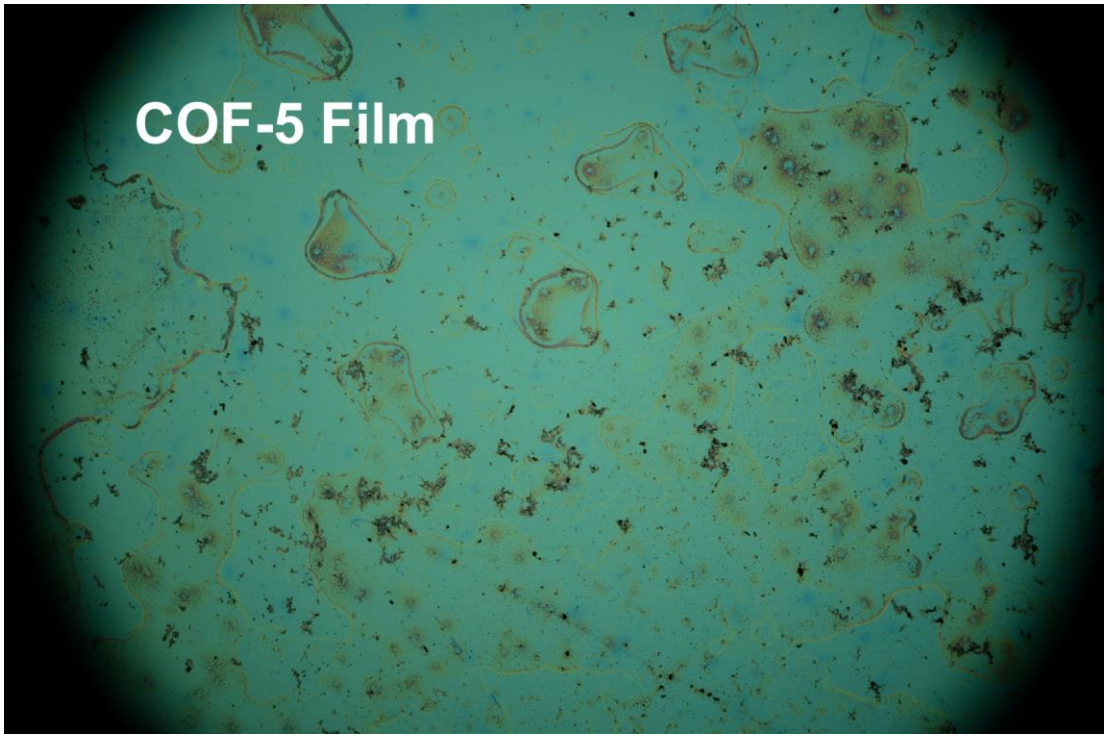

Figure S17. Optical Microscopy Image of COF-5/SiO_2/Si grown under previously reported solvothermal conditions.[7]

F. Atomic Force Microscopy

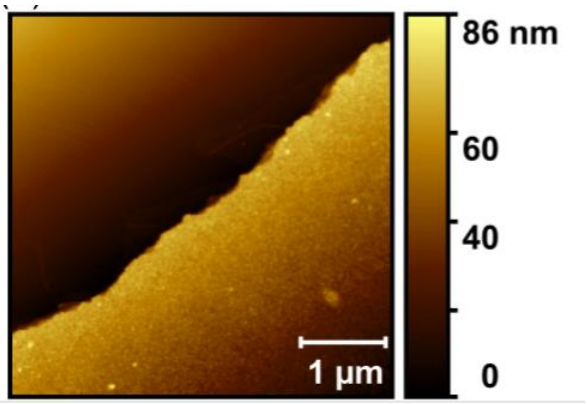

Figure S18. Atomic force micrograph of COF-5 film used for thermal property measurement

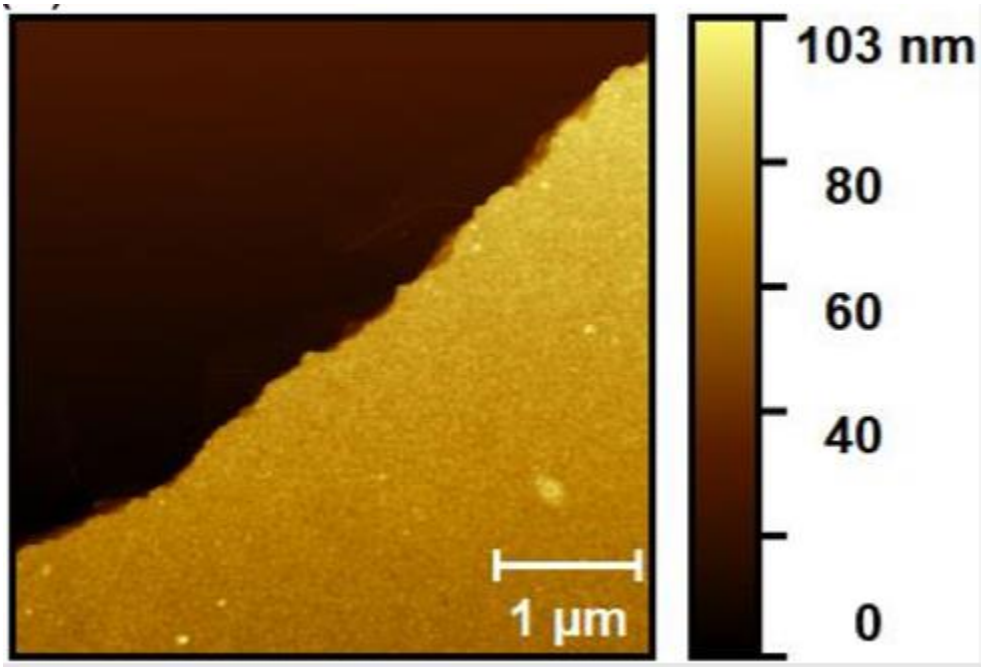

Figure S19. Atomic force micrograph of TP-COF film used for thermal property measurement

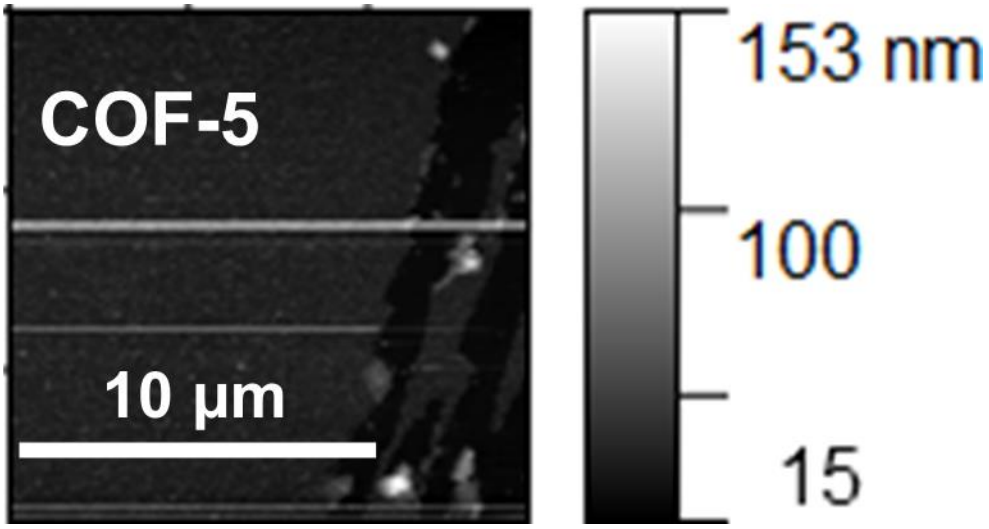

Figure S20. COF-5 film prepared using colloidal conditions

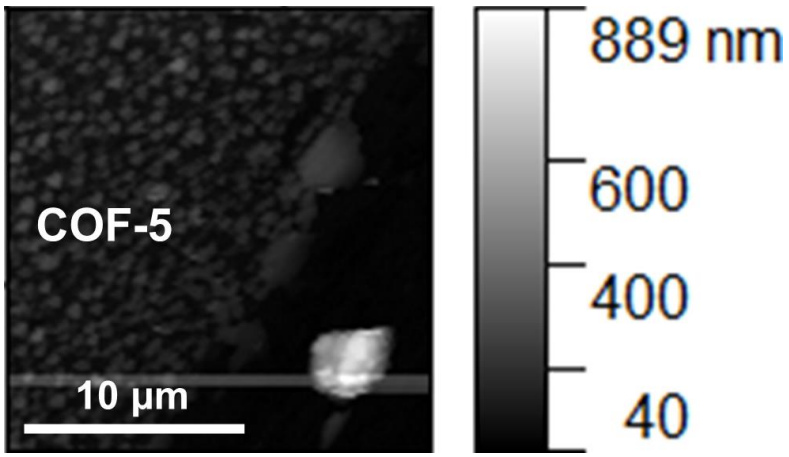

Figure S21. Atomic force micrograph of COF-5 film prepared using previously reported solvothermal conditions.[7]

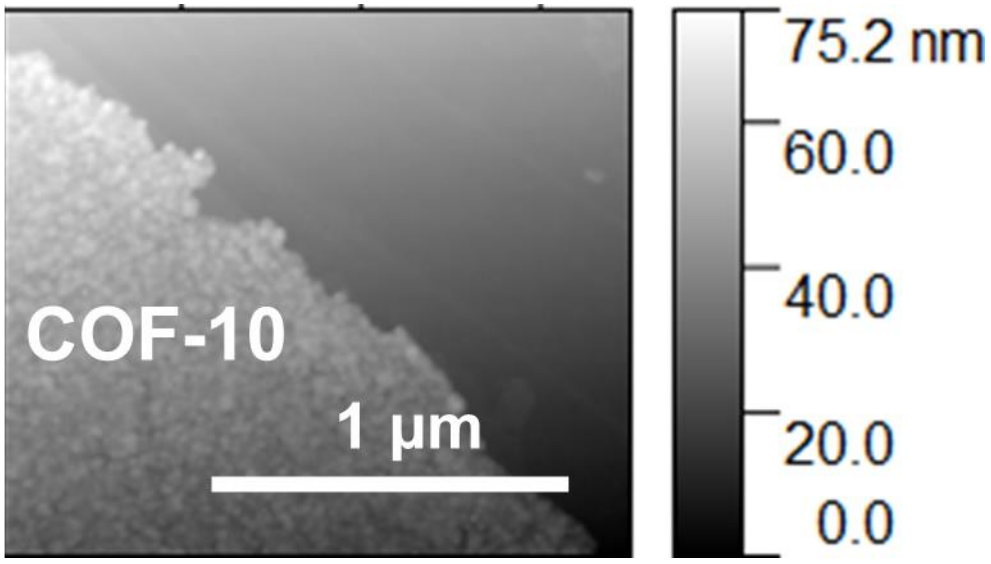

Figure S22. Atomic force micrograph of COF-10 produced using colloidal conditions

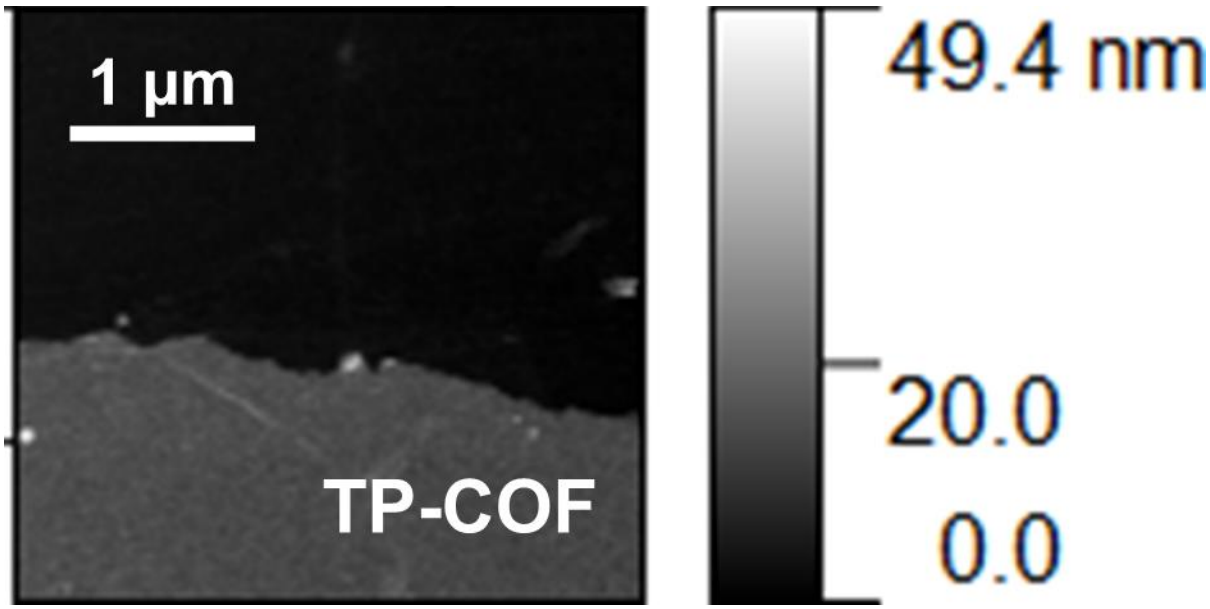

Figure S23. Atomic force micrograph of TP-COF produced using colloidal conditions

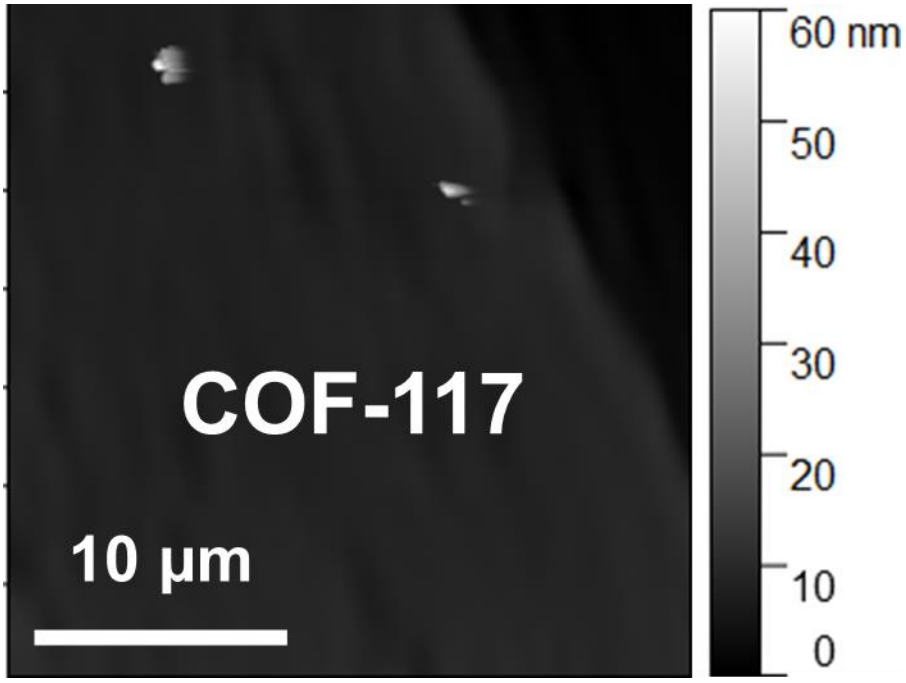

Figure S24. Atomic force micrograph of COF-117 produced using colloidal conditions

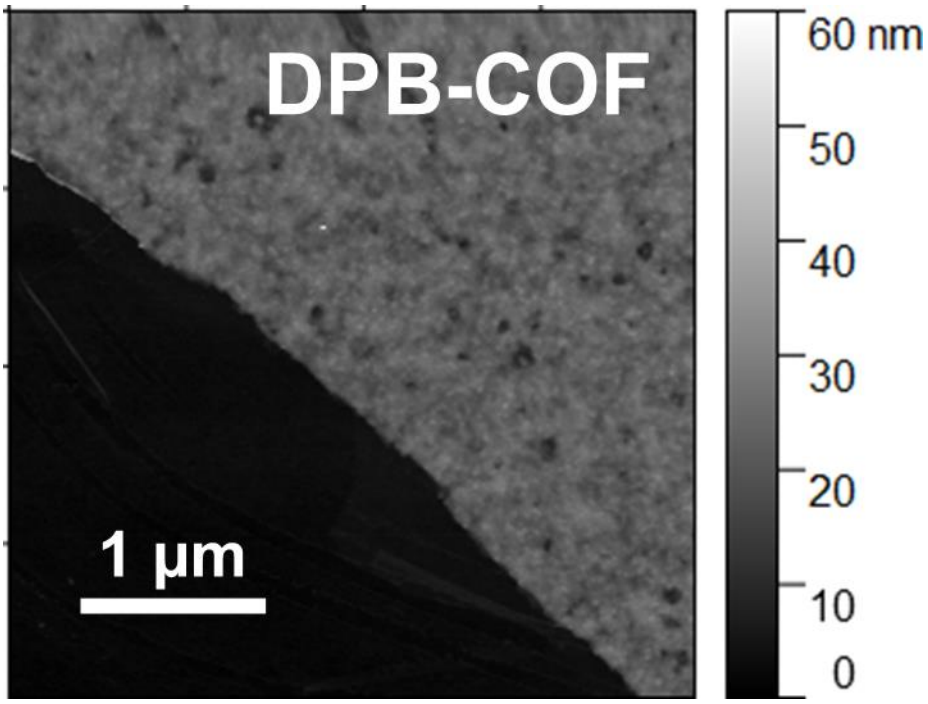

Figure S25. Atomic force micrograph of DPB-COF produced using colloidal conditions

G. Grazing-Incidence X-ray Diffraction

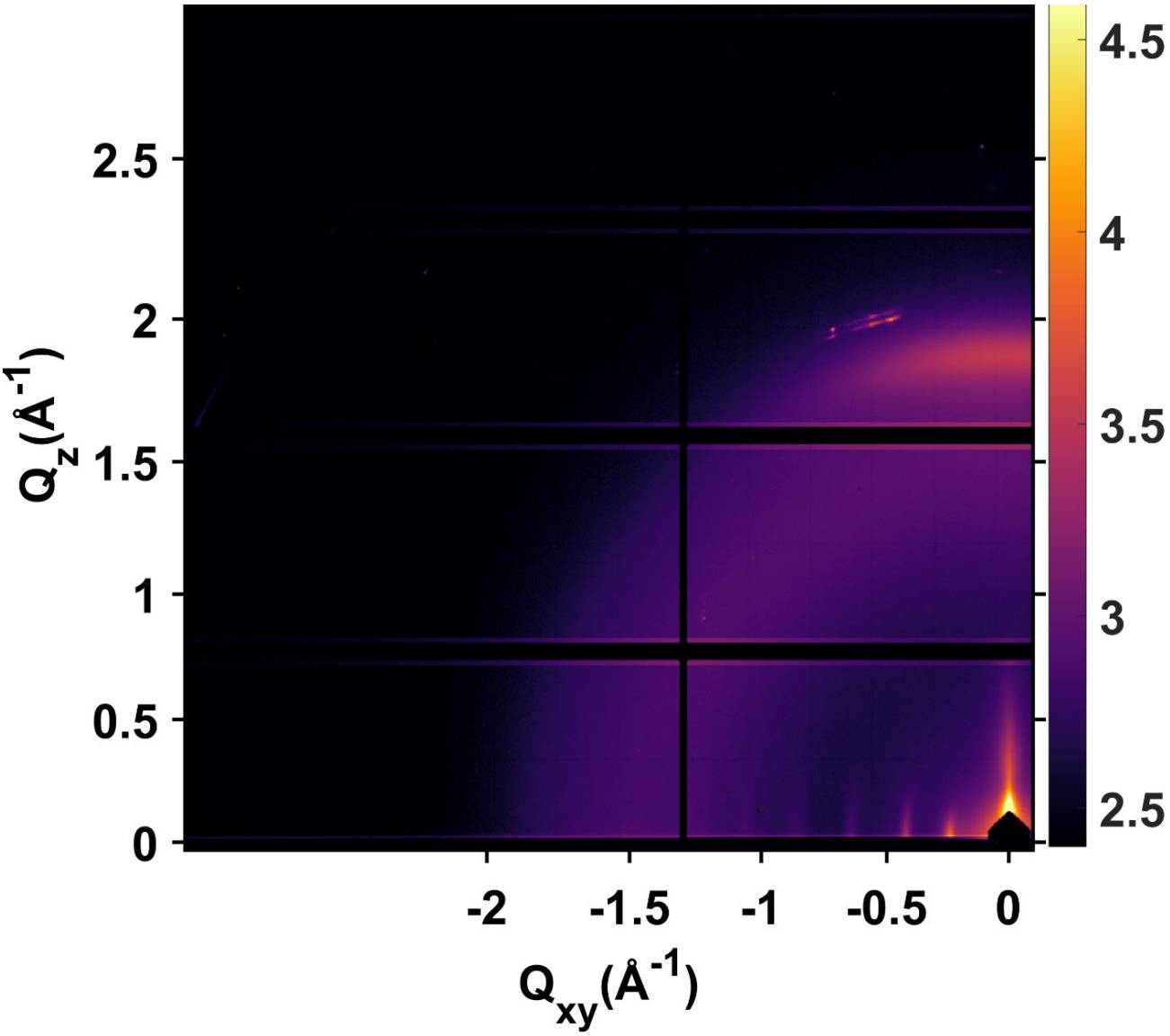

Figure S26. 2D Grazing-incidence X-ray diffraction Pattern of COF-5/SiO_2/Si grown by colloidal conditions

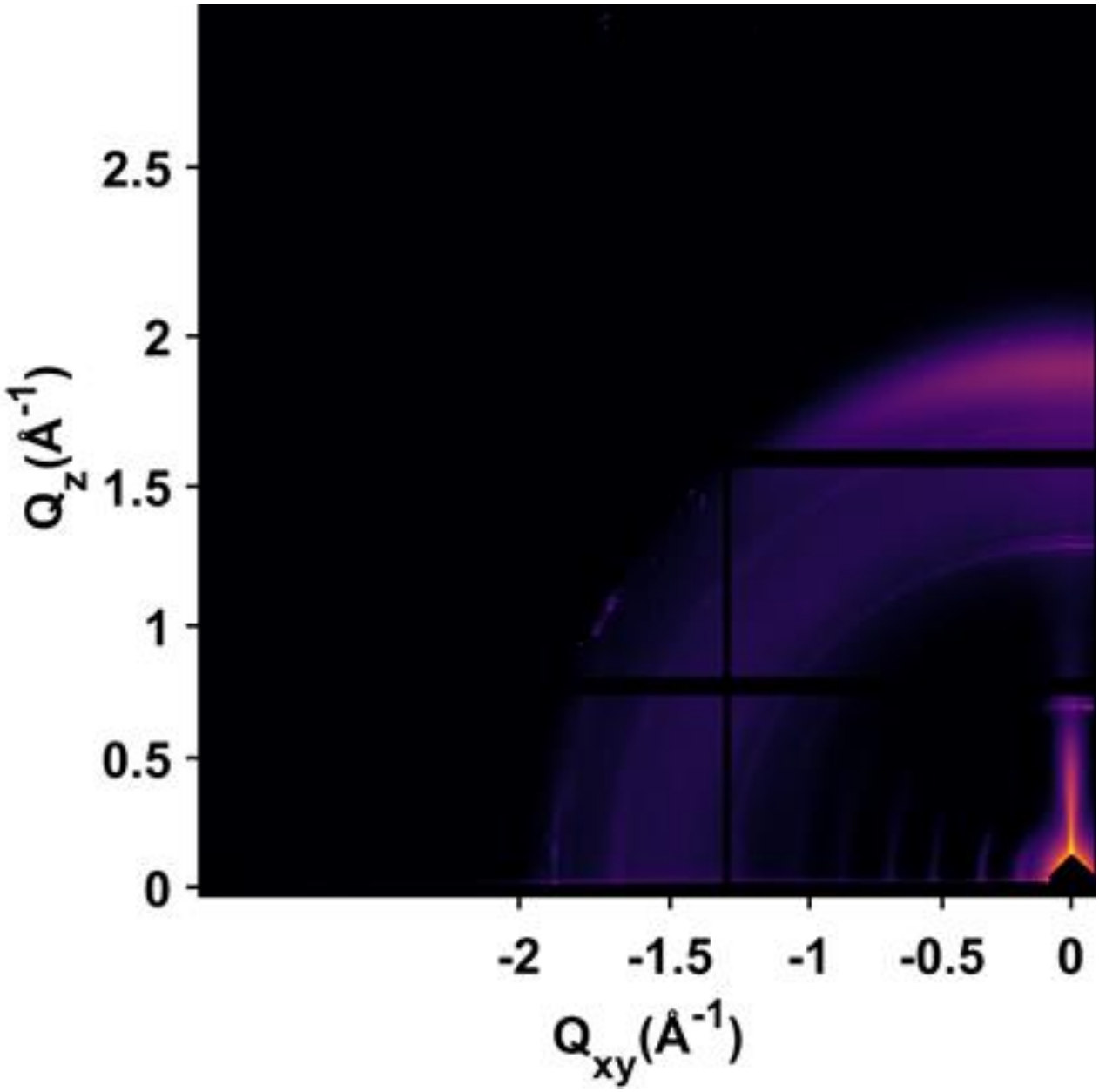

Figure S27. 2D Grazing-incidence X-ray diffraction Pattern of COF-10/SiO_2/Si grown by colloidal conditions

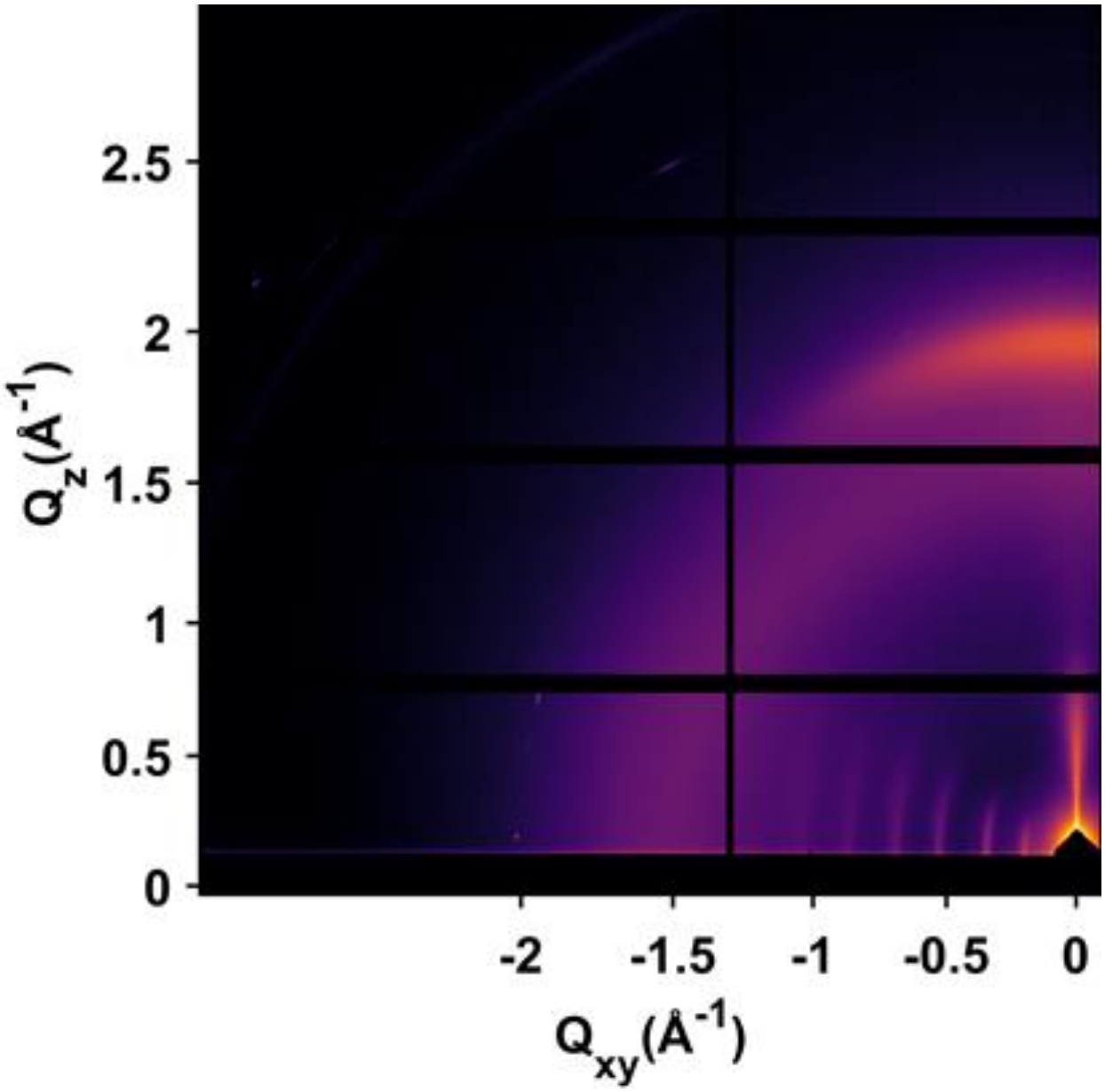

Figure S28. 2D Grazing-incidence X-ray diffraction Pattern of TP-COF/SiO_2/Si grown by colloidal conditions

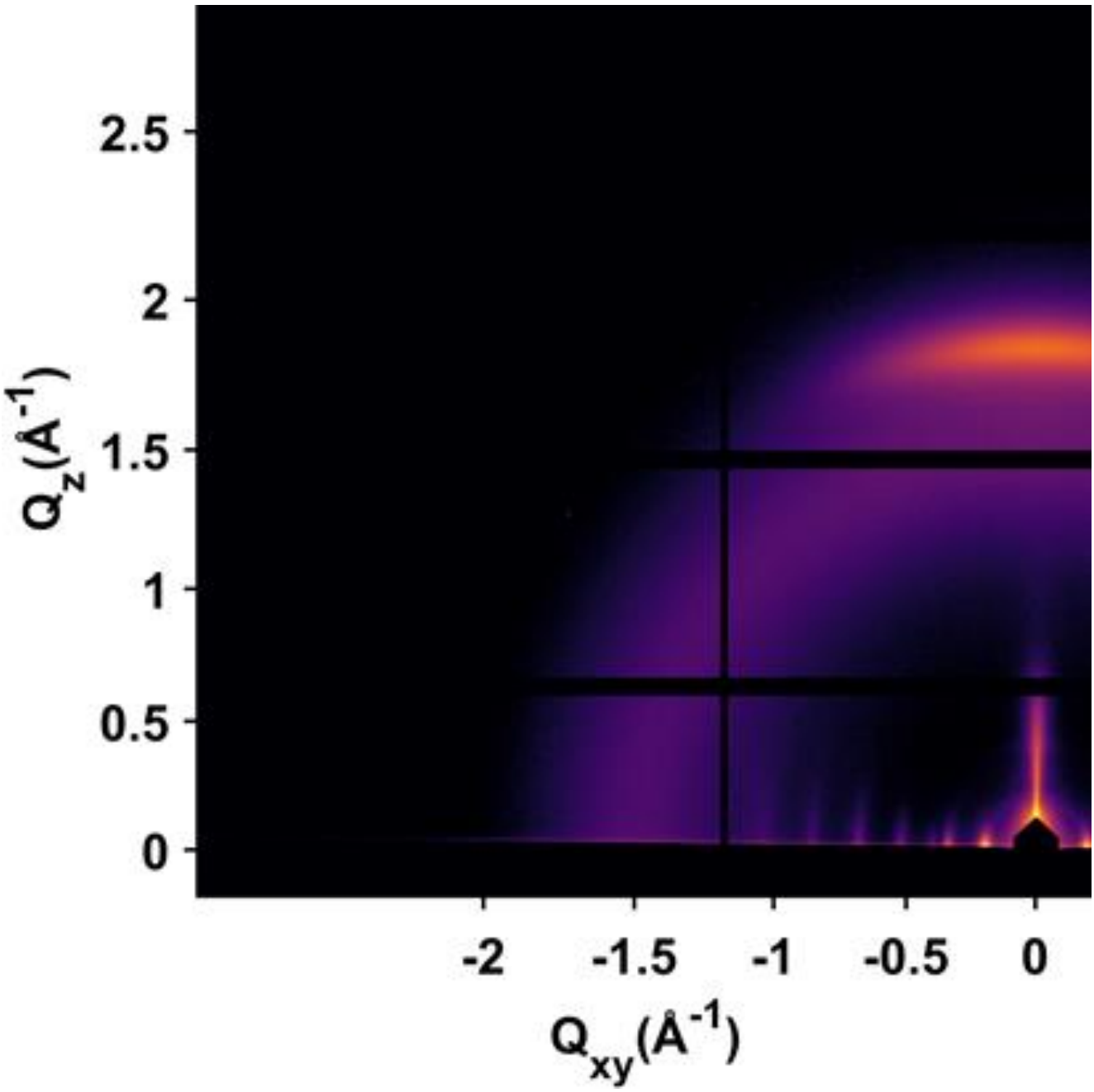

Figure S29. 2D Grazing-incidence X-ray diffraction Pattern of DPB-COF/SiO_2/Si grown by colloidal conditions

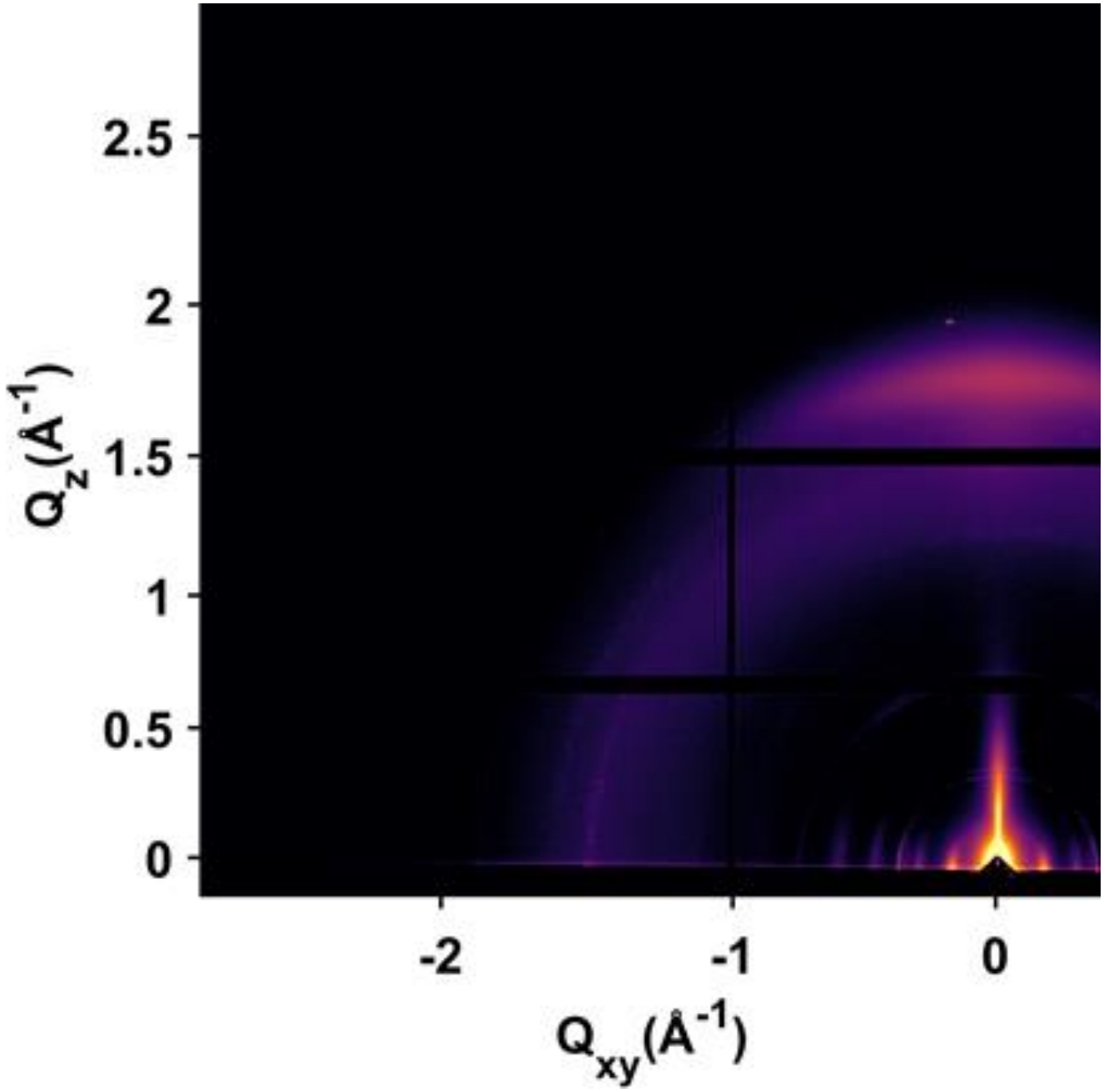

Figure S30. 2D Grazing-incidence X-ray diffraction Pattern of COF-117/SiO_2/Si grown by colloidal conditions

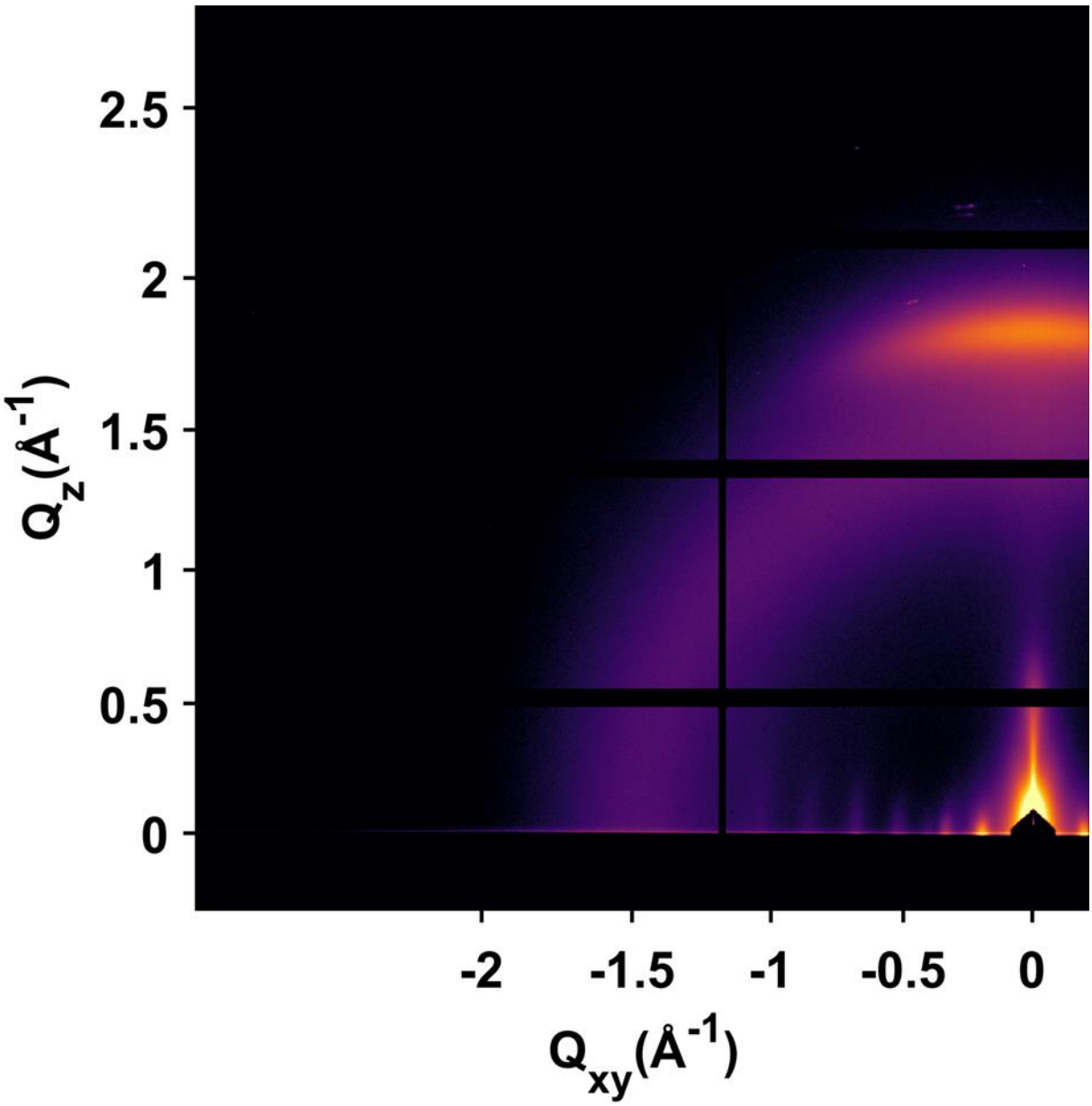

Figure S31. 2D Grazing-incidence X-ray diffraction Pattern of TP-COF/SiO_2/Si grown by colloidal conditions after one monomer polymerization cycle

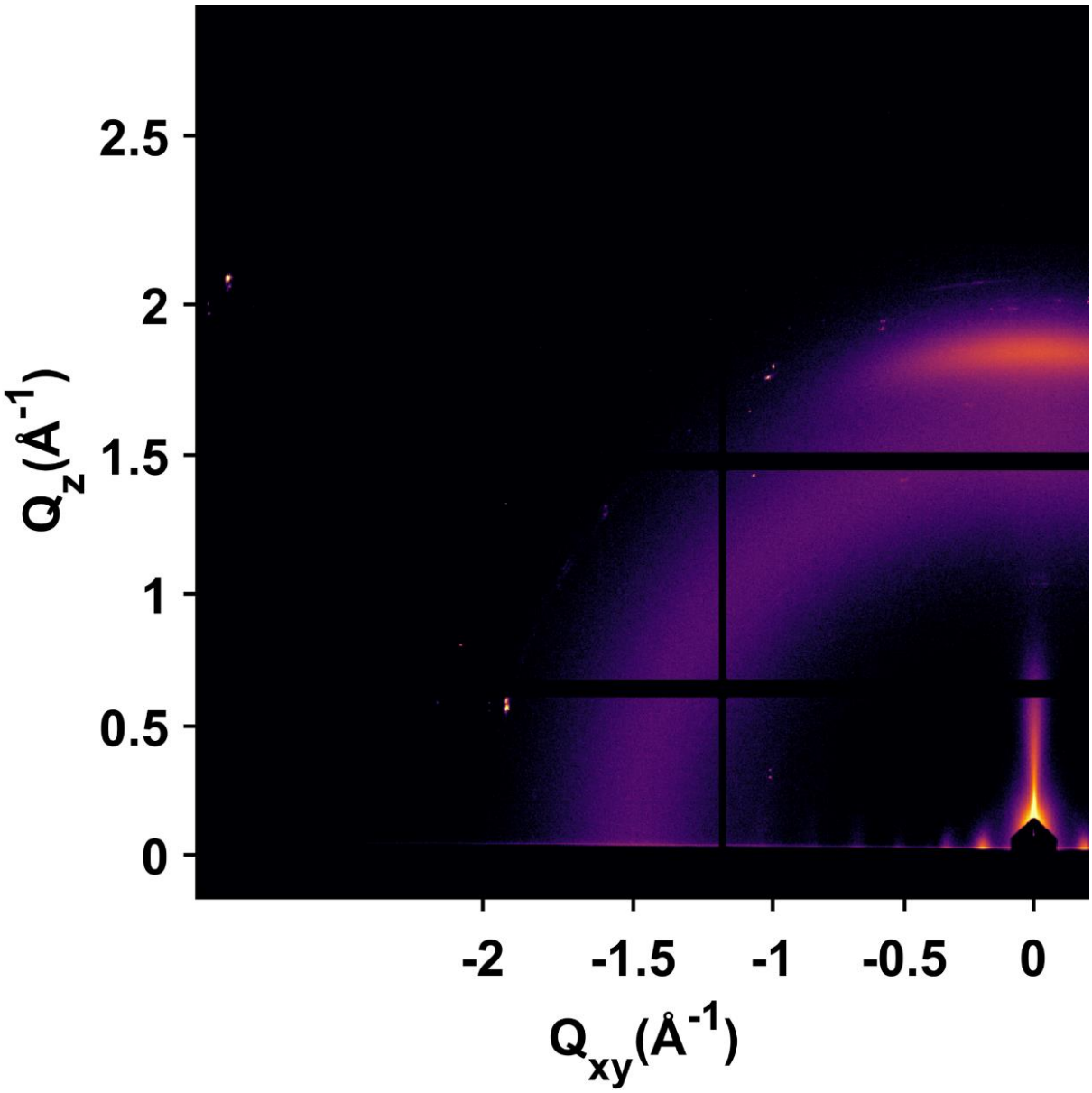

Figure S32. 2D Grazing-incidence X-ray diffraction Pattern of TP-COF/SiO_2/Si grown by colloidal conditions after two monomer polymerization cycles

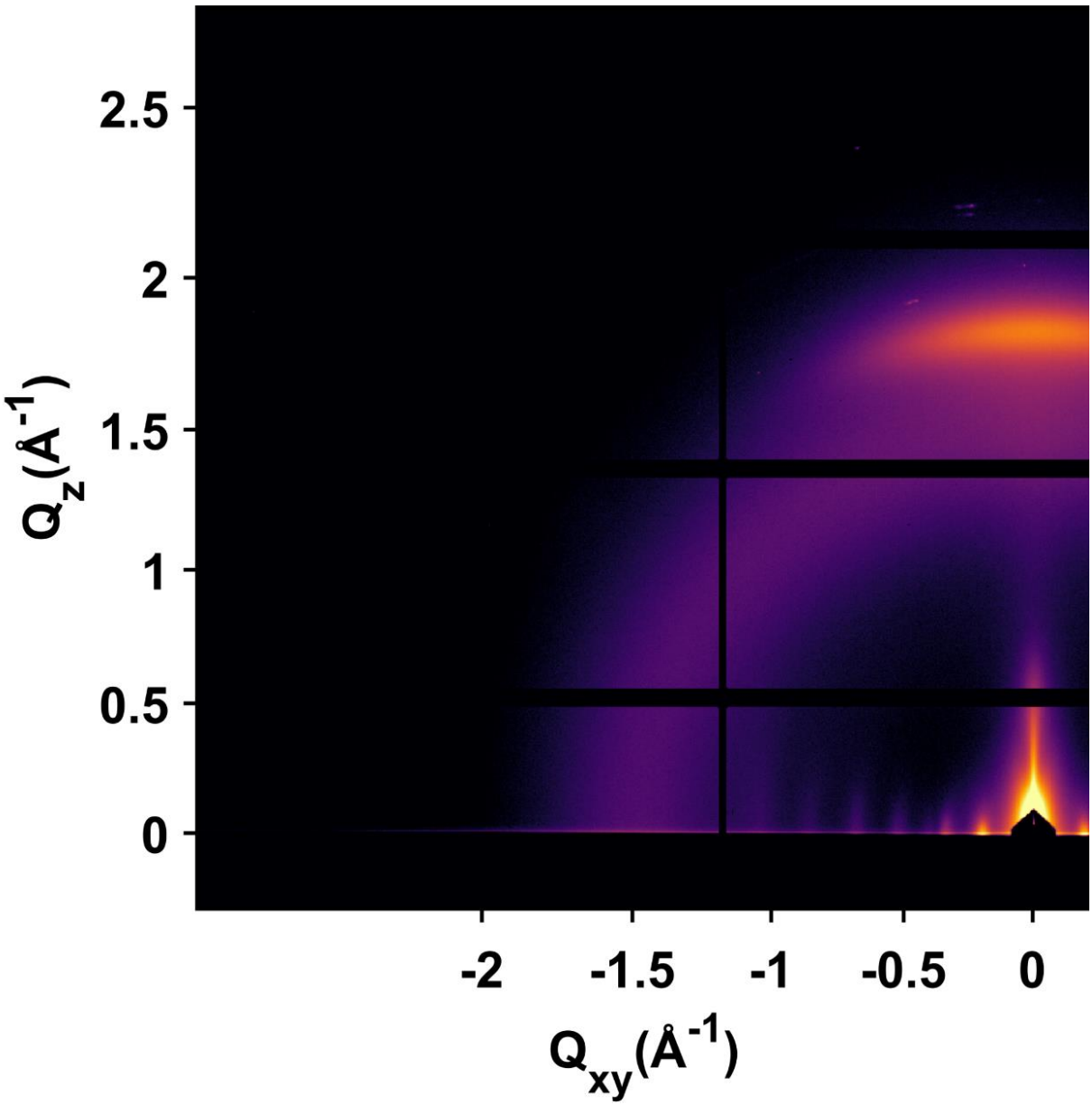

Figure S33. 2D Grazing-incidence X-ray diffraction Pattern of TP-COF/SiO_2/Si grown by colloidal conditions after three monomer polymerization cycles

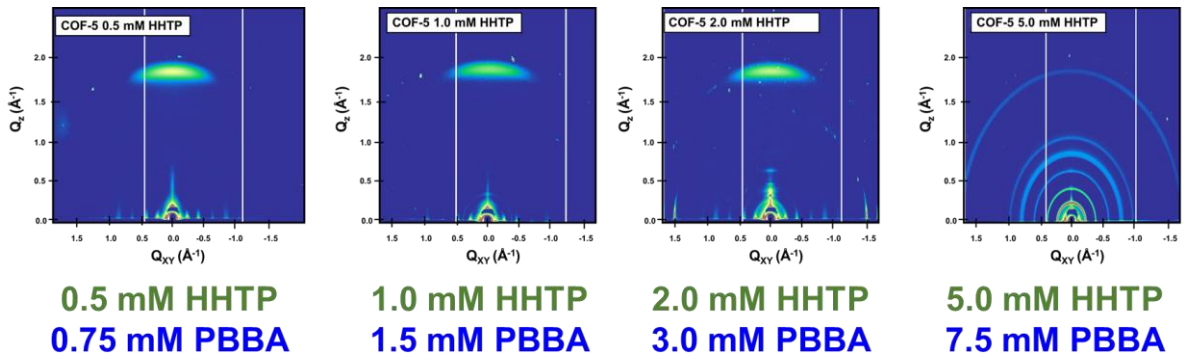

Figure S34. 2D Grazing-incidence X-ray diffraction Patterns of COF-5/SiO_2/Si polymerized from different initial monomer concentrations under colloidal conditions.

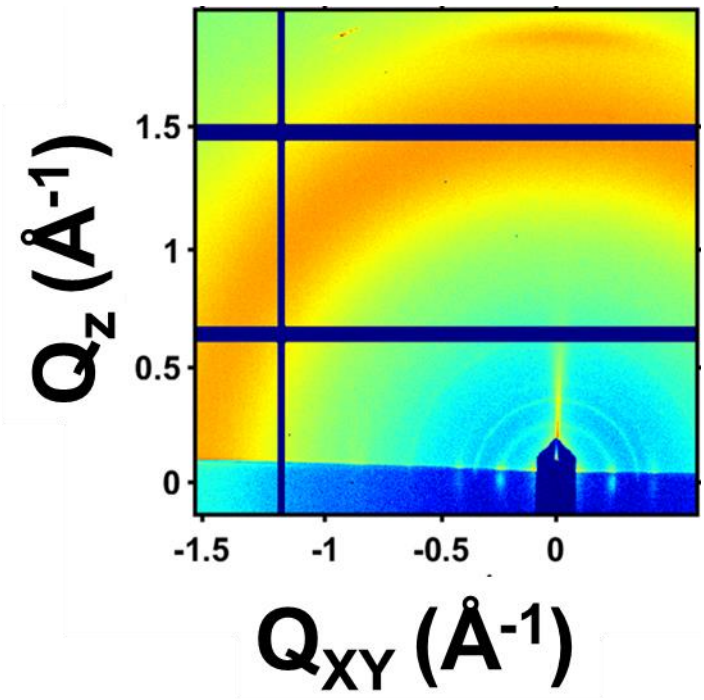

Figure S35. 2D Grazing-incidence X-ray diffraction Patterns of COF-5/SiO_2/Si polymerized from solvothermal noncolloidal conditions.[7]

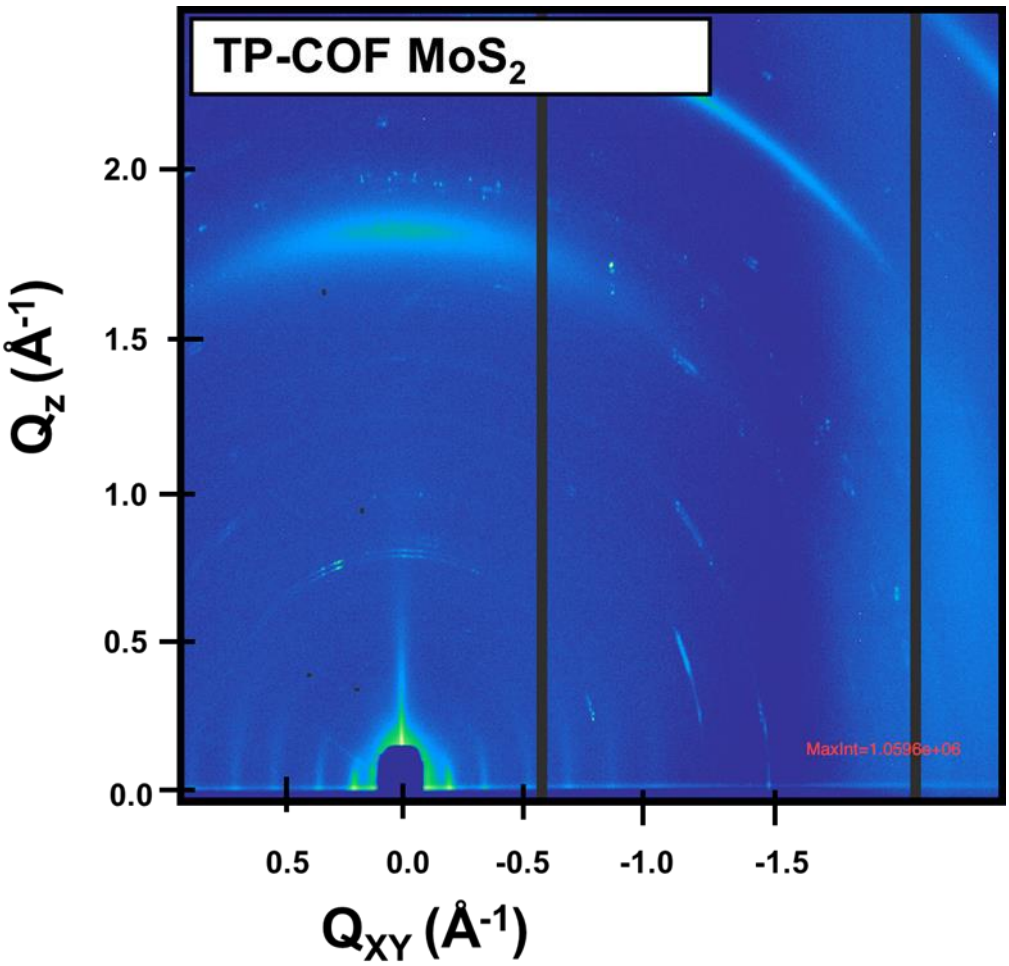

Figure S36. 2D Grazing-incidence X-ray diffraction Patterns of TP-COF/MoS_2/Al_2O_3 polymerized from solvothermal noncolloidal conditions

H. Simulated and Experimental X-ray Diffraction Patterns

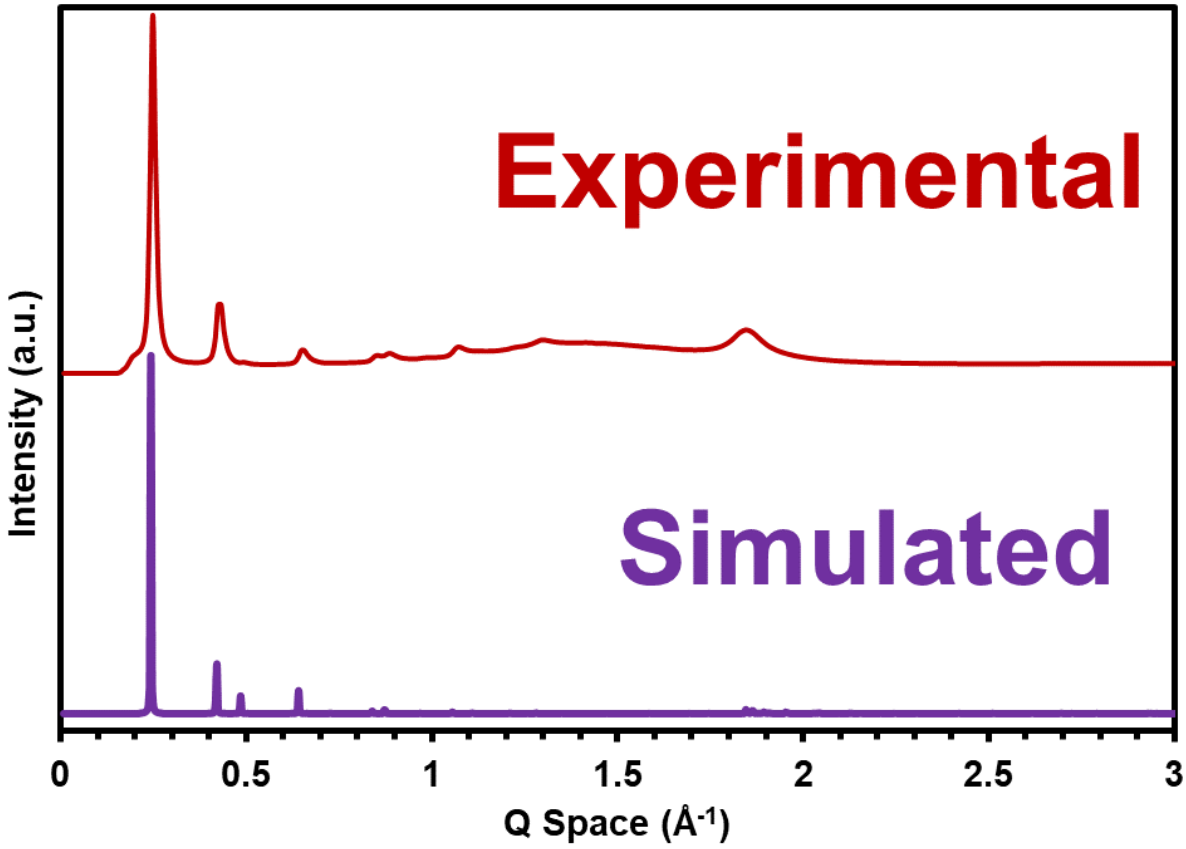

Figure S37. Linear experimental X-ray diffraction pattern extracted from 2D GI-WAXS pattern of COF-5 and simulated X-ray diffraction pattern from a geometry optimized COF-5 crystallite.

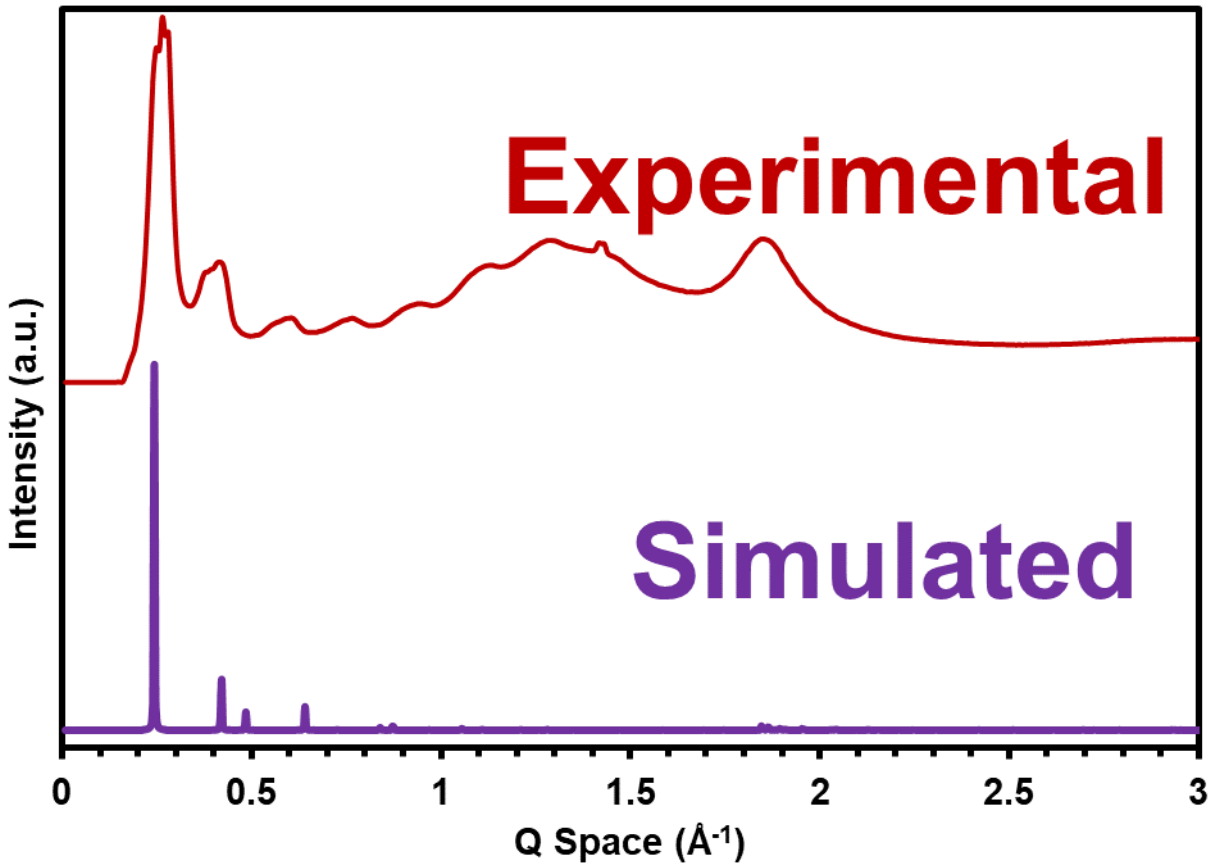

Figure S38. Linear experimental X-ray diffraction pattern extracted from 2D GI-WAXS pattern of COF-10 and simulated X-ray diffraction pattern from a geometry optimized COF-10 crystallite.

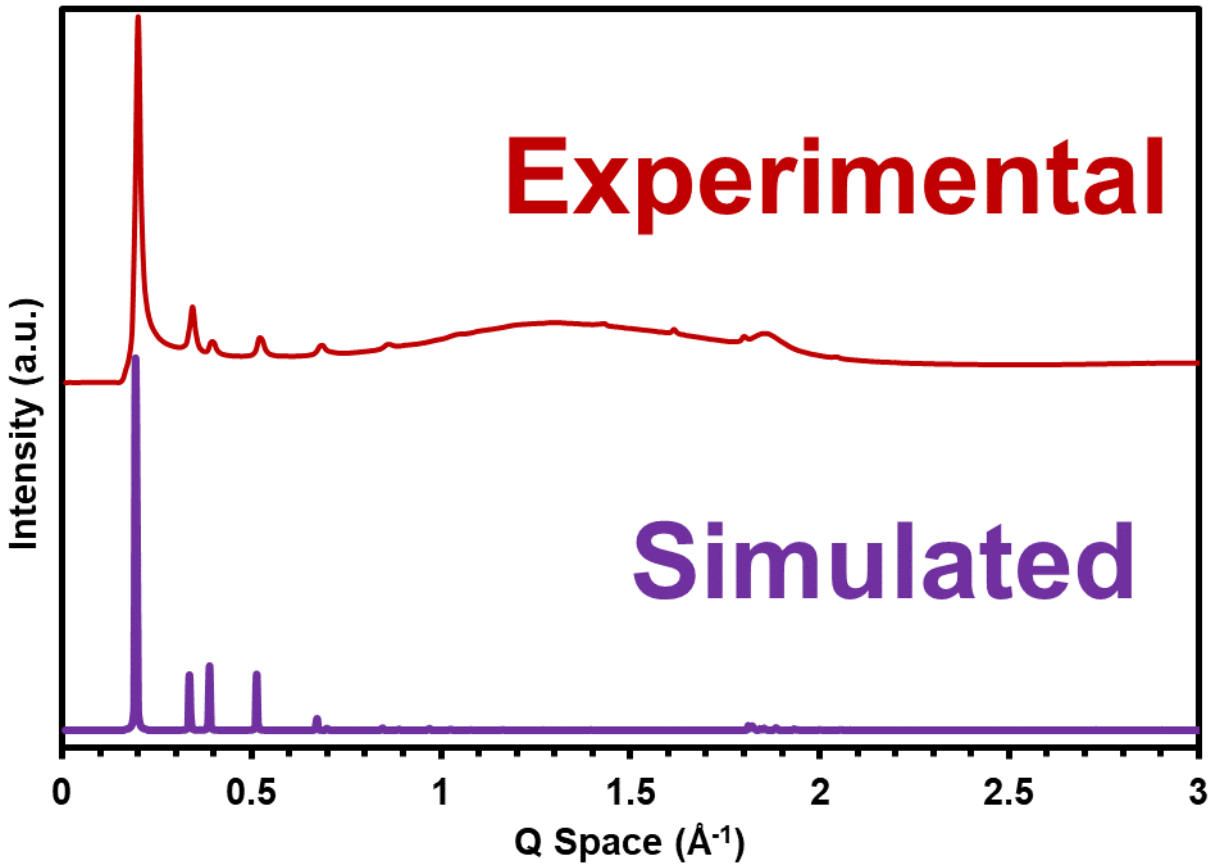

Figure S39. Linear experimental X-ray diffraction pattern extracted from 2D GI-WAXS pattern of TP-COF and simulated X-ray diffraction pattern from a geometry optimized TP-COF crystallite.

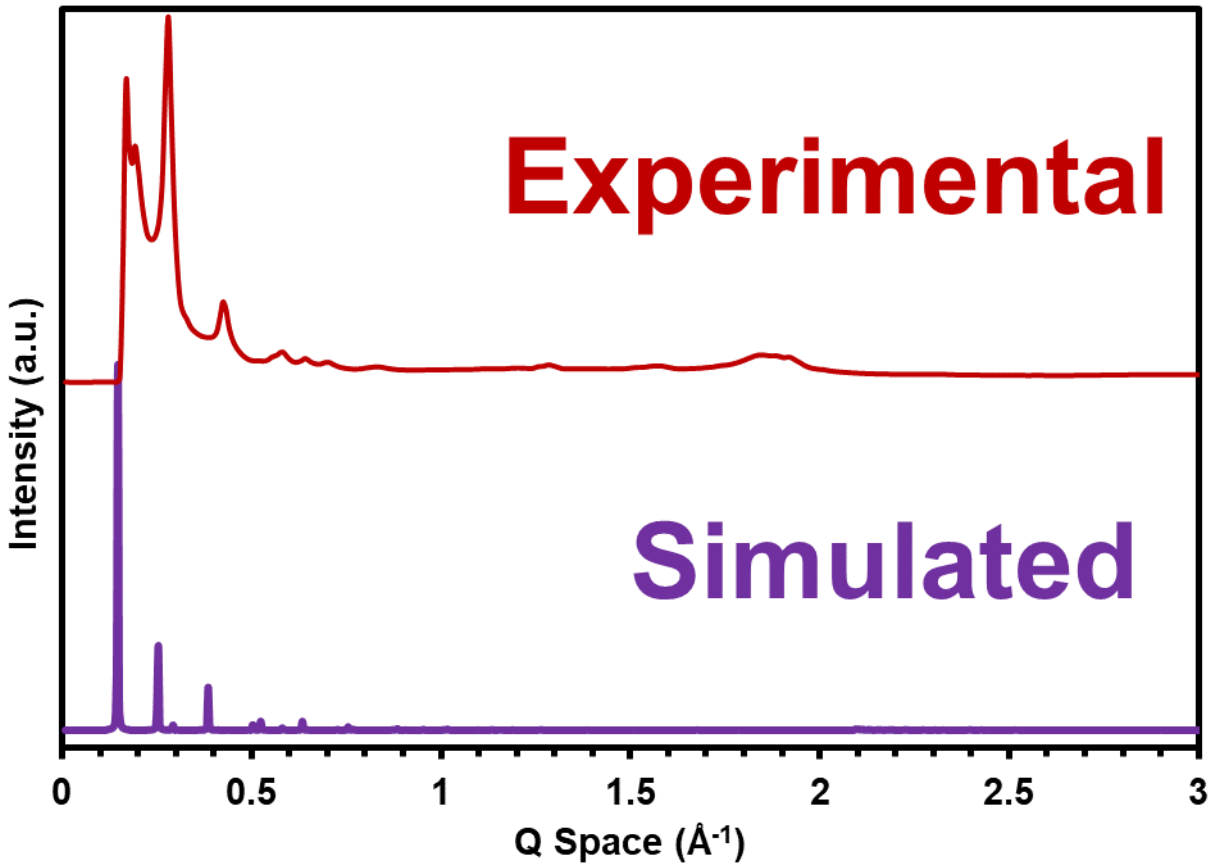

Figure S40. Linear experimental X-ray diffraction pattern extracted from 2D GI-WAXS pattern of DPB-COF and simulated X-ray diffraction pattern from a geometry optimized DPB-COF crystallite.

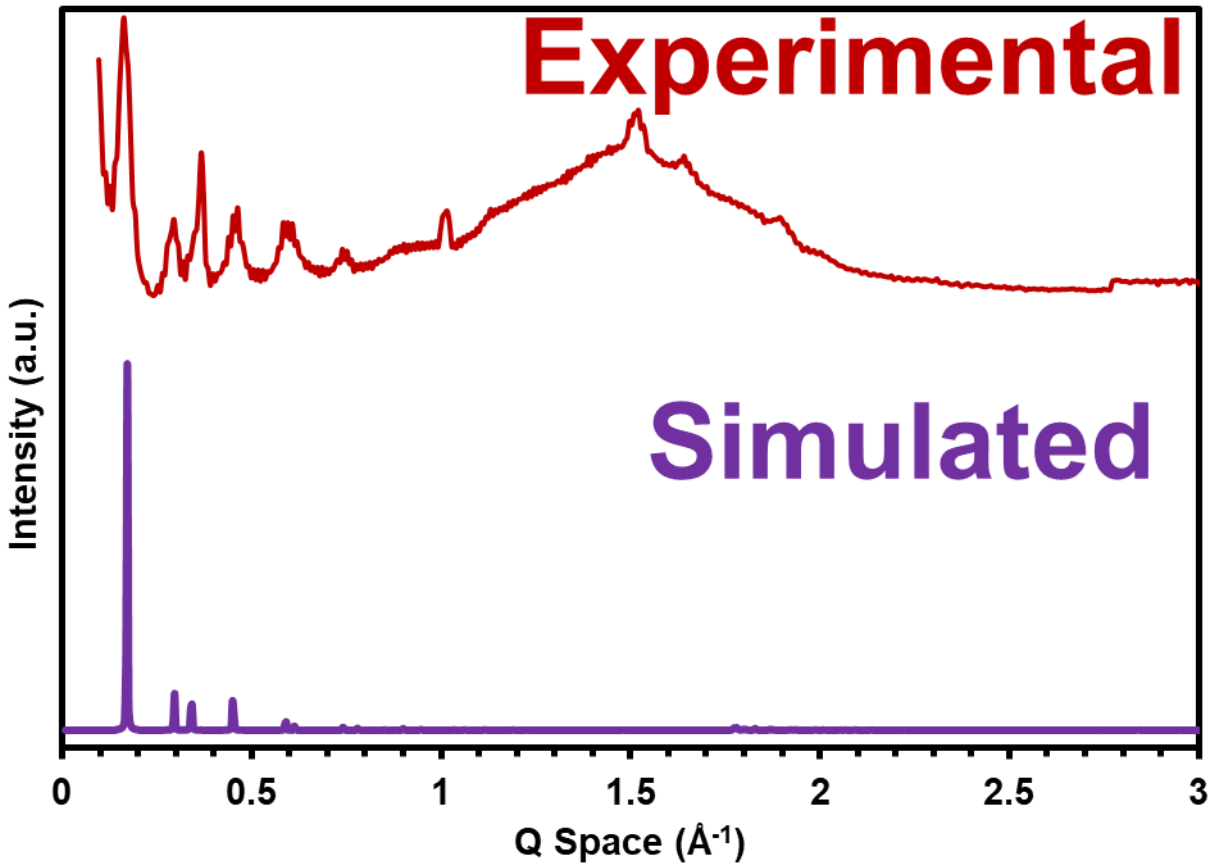

Figure S41. Linear experimental X-ray diffraction pattern extracted from 2D GI-WAXS pattern of COF-117 and simulated X-ray diffraction pattern from a geometry optimized COF-117 crystallite.

I. Density Functional Theory (DFT) Calculations

The electronic band structures of COF-5 were calculated with the CRYSTAL17 package[8,9] at the DFT PBE0 level[10,11] using the POB-TZVF basis set with D3 van der Waals (vdW) corrections[12]. 2 x 2 x 14 and 2 x 2 x 18 Γ-centered Monkhorst-Pack *k*-meshes were adopted in the geometry optimizations and self-consistent calculations (SCF), respectively.

The macroscopic static dielectric tensors taking account of the electronic contributions[13] were calculated at the DFT PBE level using the Vienna Ab initio Simulation Package (VASP) [14] and D3 vdW corrections. Γ-centered Monkhorst-Pack *k*-meshes were adopted in both geometry optimizations and SCF calculations (see **Table S1**). The convergence criterion for the total energy was set at 10^{-8} eV; the one for the forces was set at 0.01 eV $Å^{-1}$. We considered a Gaussian smearing of 0.01 eV. The lattice parameters after geometry optimization of each COF are shown in **Table S2**. The off-diagonal components in the calculated macroscopic static dielectric tensors are vanishingly small. The ionic contributions to the macroscopic static dielectric tensors of COF-5 were calculated via density functional perturbation theory (DFPT)[15] using VASP.

Table S1. Γ-centered Monkhorst-Pack *k*-meshes applied in the DFT/PBE calculations for the five COFs.Γ-centered Monkhorst-Pack *k*-meshes applied for each COF

	COF-5	TP-COF	COF-10	COF-117	DPB-COF
Optimization	1 × 1 × 8	1 × 1 × 10	1 × 1 × 10	1 × 1 × 11	1 × 1 × 12
SCF	2 × 2 × 16	2 × 2 × 20	2 × 2 × 20	2 × 2 × 22	2 × 2 × 24

Table S2. Optimized crystal structures at the DFT/PBE level for the five COFs.

	a(Å)	b(Å)	c(Å)	α(°)	β(°)	γ(°)
COF-5	30.17	30.17	3.73	90.00	90.00	120.00
TP-COF	37.53	37.53	3.72	90.00	90.00	120.00
COF-10	37.72	37.72	3.71	90.00	90.00	120.00
COF-117	41.98	41.98	4.08	90.00	90.00	120.02
DPB-COF	46.53	46.53	3.74	90.00	90.00	120.00

Table S3. Ionic and electronic contributions to the COF-5 dielectric tensors.

	ε_{xx}	ε_{yy}	ε_{zz}
Ionic contributions	0.3	0.1	0.0
Electronic contribution	2.0	2.0	1.3
Total	2.3	2.1	1.4

J. Polarization Dependent Emission of 2D COF Films

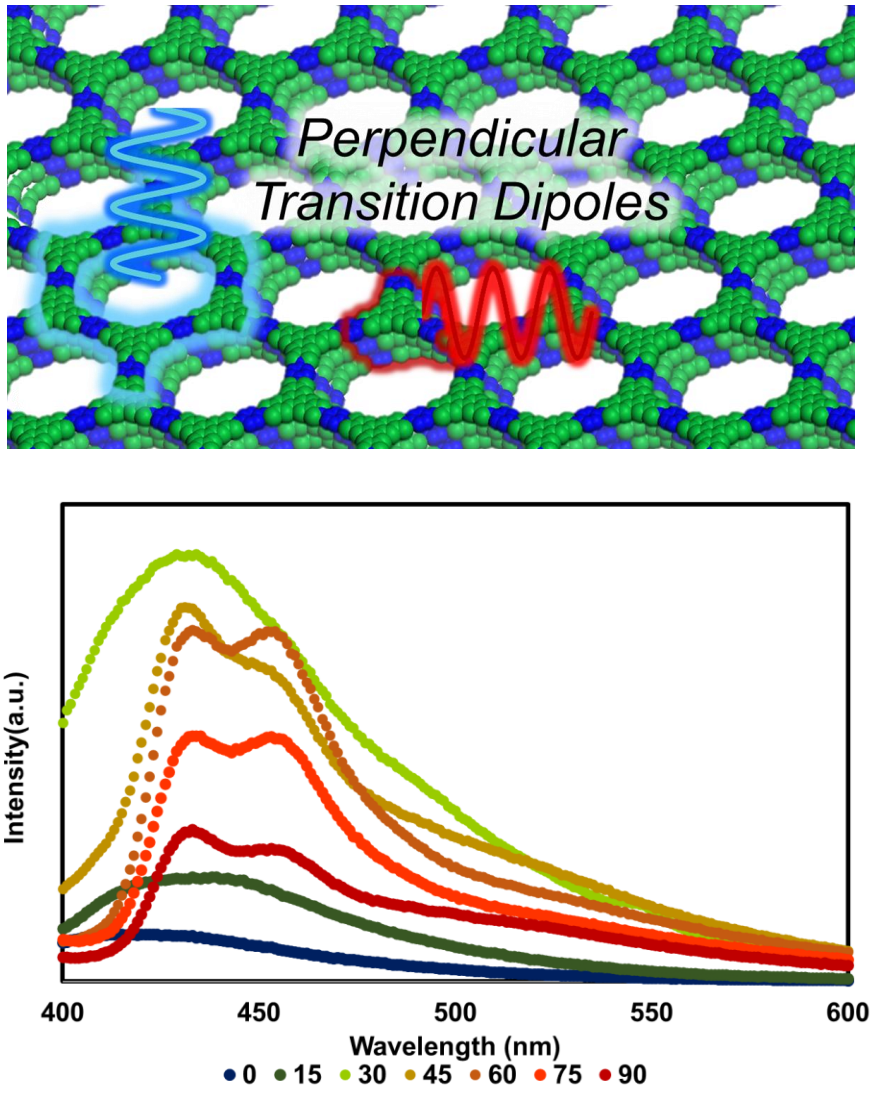

Figure S42. Polarization dependent emission of TP-COF films

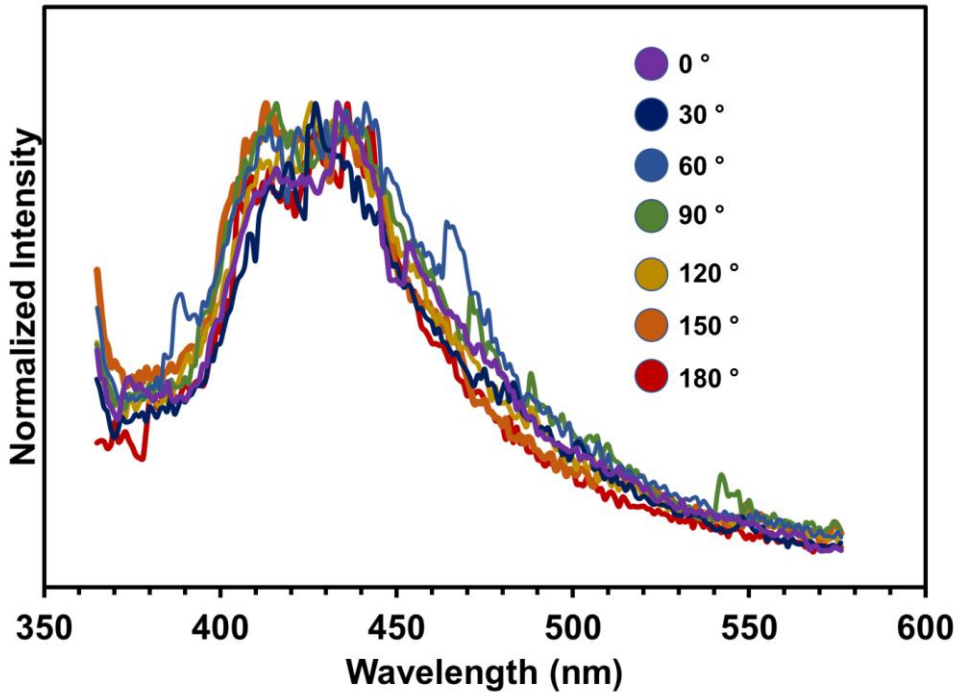

Figure S43. Polarization dependent emission of COF-5 films produced via solvothermal synthesis

K. Scanning Electron Microscopy

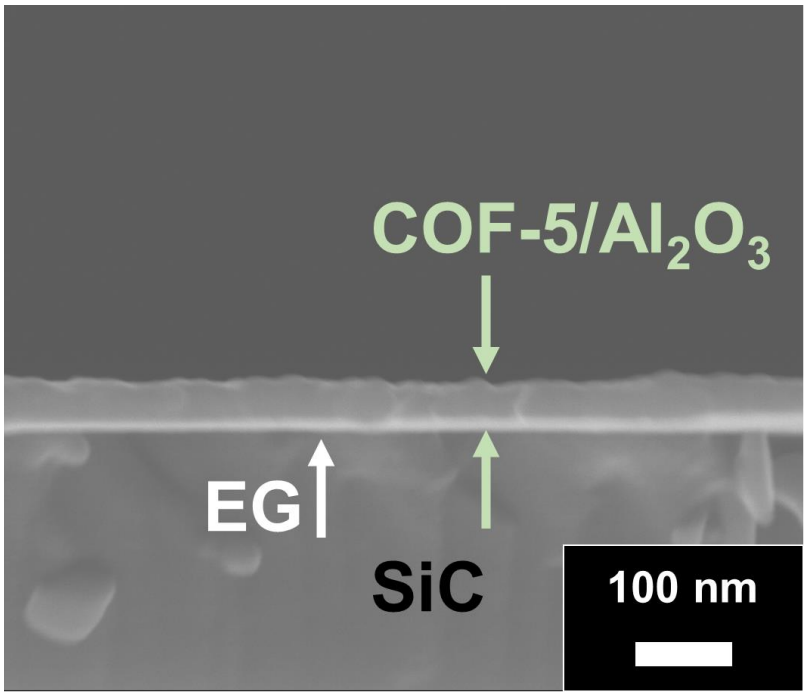

Figure S44. Cross-sectional scanning electron micrograph of COF-5/Al_2O_3/EG/SiC

L. X-ray Reflectivity of 2D COF Films and Devices

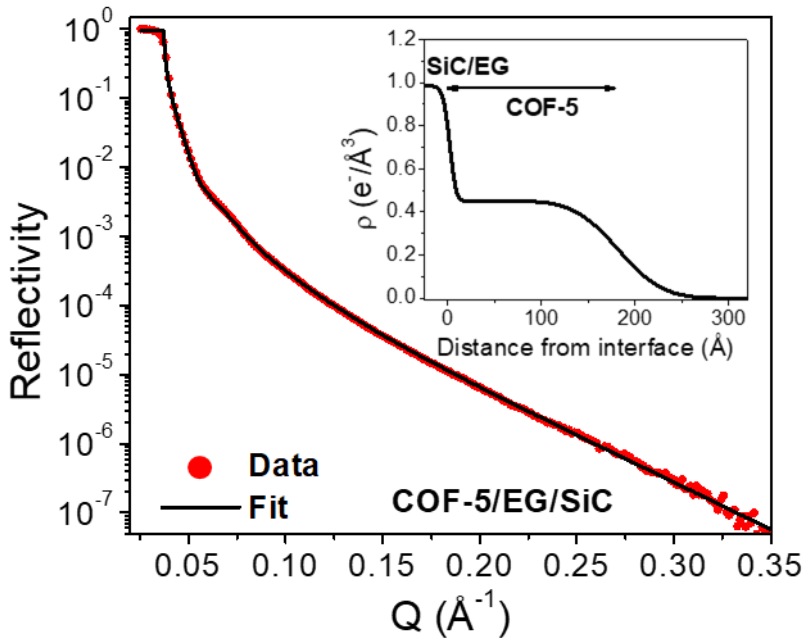

Figure S45. X-ray reflectivity profiles of COF-5/EG/SiC. Inset: Extracted Electron Density Profile.

Table S4. XRR fitting parameters from figure S45.

	Thickness (Å)	Roughness (Å)	e^- density (e^- Å^{-3})
COF-5	**177.7**	**37.3**	**0.452**
EG	**4.0**	**4.6**	**0.678**
SiC	**-**	**5.6**	**0.983**

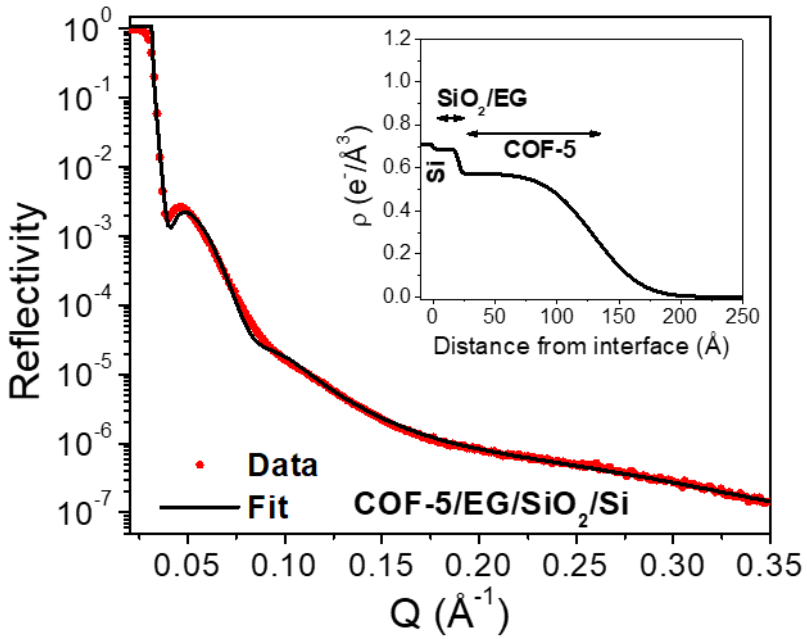

Figure S46. X-ray reflectivity data a fit of COF-5/EG/SiO2/Si. Inset: Electron density profile extracted from the XRR fit.

Table S5. XRR fitting parameters from figure S46

.

	Thickness (Å)	Roughness (Å)	e^- density (e^- Å^{-3})
COF-5	**108.8**	**30.4**	**0.573**
SiO_2/EG	**20.5**	**2.1**	**0.688**
Si	**-**	**1.0**	**0.709**

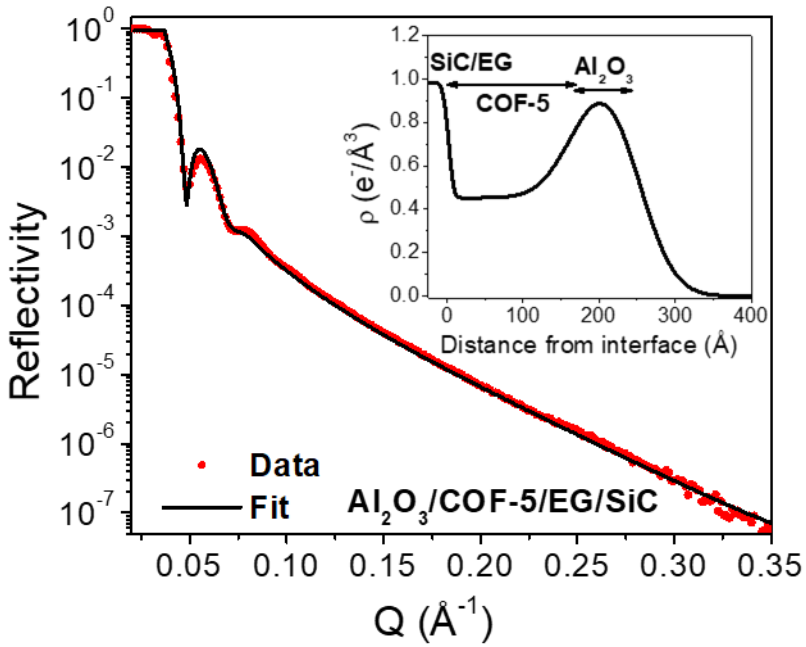

Figure S47. X-ray reflectivity profiles of Al_2O_3/COF-5/EG/SiO_2/Si Inset: Extracted Electron Density Profile.

Table S6. XRR fitting parameters from figure S47.

.

	Thickness (Å)	Roughness (Å)	e^- density (e^- Å^{-3})
Al_2O_3	75.1	38.7	1.192
COF-5	168.9	38.5	0.452
EG	3.99	4.6	0.678
SiC	-	5.6	0.983

M. 2D COF Film Device Measurements

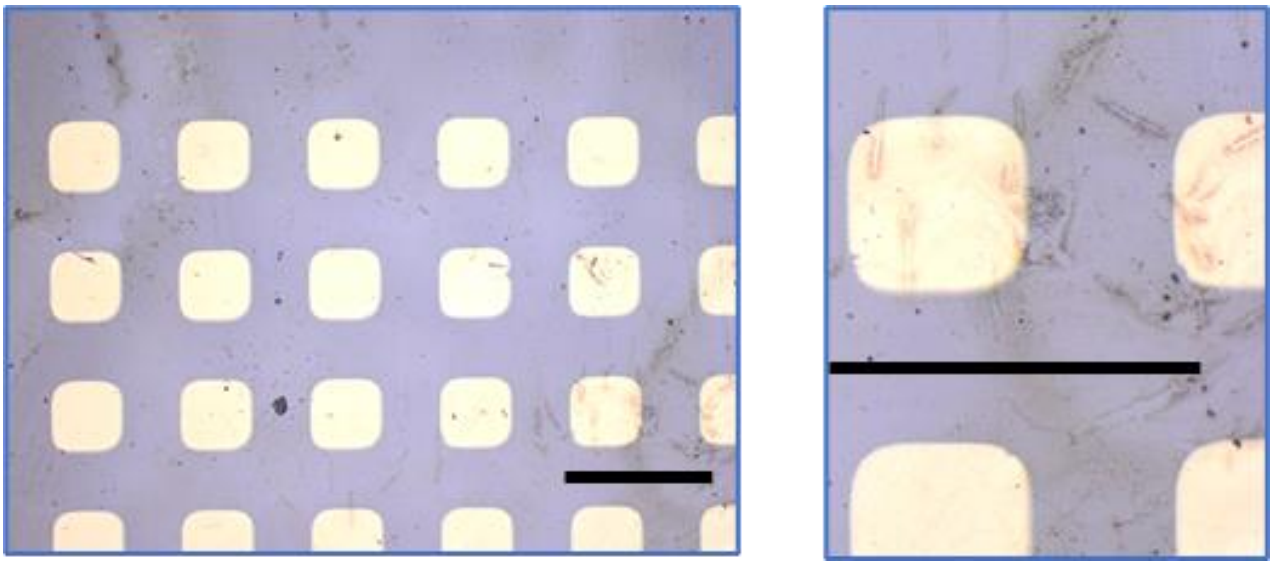

Figure S48. Optical microscope images of Al_2O_3/COF-5/EG/SiC (Scale Bar = 200 μm)

The area of each Au pad is roughly 100,000 μm^2 (10^{-8} m^2) as determined from the optical image on the right.

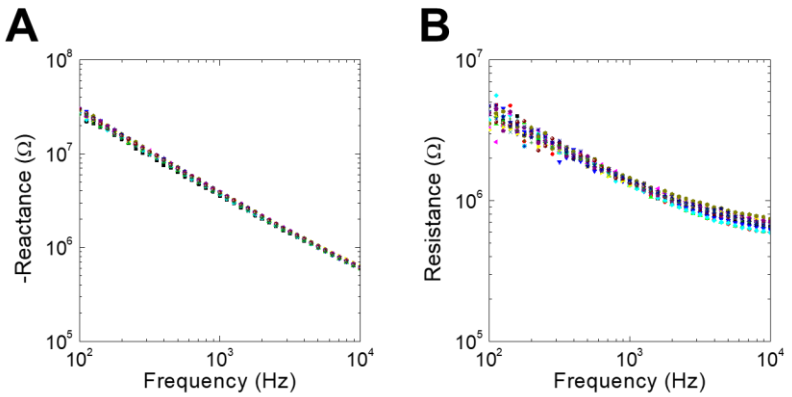

Figure S49. (A), (B) Bode plots showing tight distribution of real and imaginary parts of the impedance for 10 different COF-5 devices across the EG/SiC chip. The extracted capacitance is found vary by less than 10% over an area of 25 mm^2.

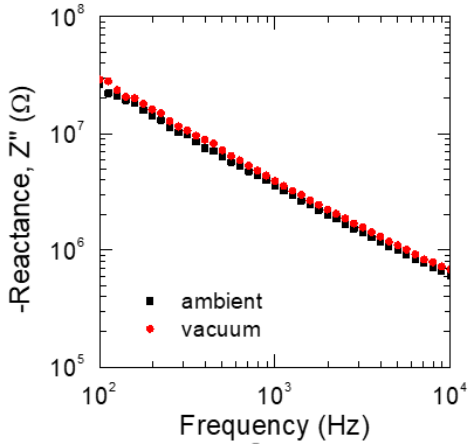

Figure S50. Plot of negative reactance (-Z") versus frequency of a Al2O3/COF-5 dielectric bilayer capacitor in ambient (relative humidity ~62 %) and in vacuum (pressure = 2 x 10-5 torr).

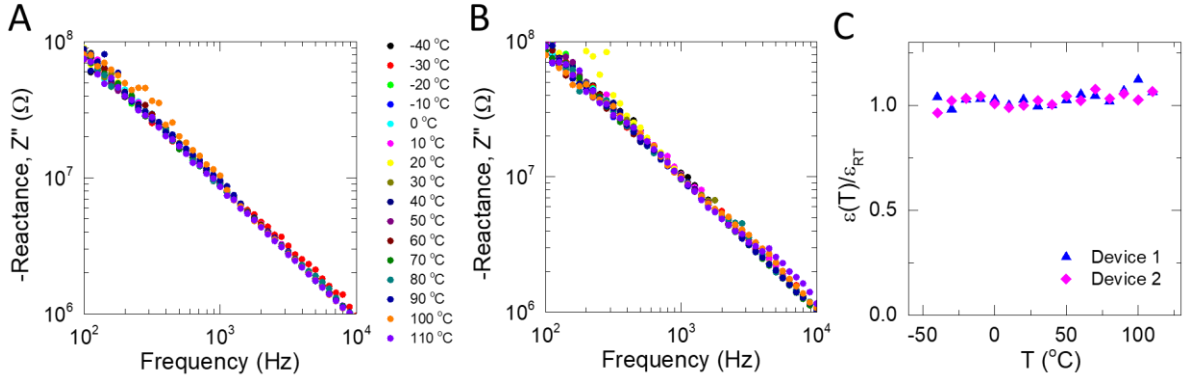

Figure S51. (A-B) Plot of negative reactance (-Z") of two different Al2O3 dielectric bilayer capacitor devices as a function of temperature (-40 °C - 110 °C). **(C)** Plot of the normalized dielectric constant across this temperature range for two devices, demonstrating that the dielectric constant is invariant across this temperature range.

N. Thermoreflectance Measurements

A. Sample Preparation. To prepare our samples for time-domain thermoreflectance (TDTR), we first deposit an 80 nm thick Al transducing layer via electron beam evaporation at $6 \cdot 10^{-6}$ Torr.

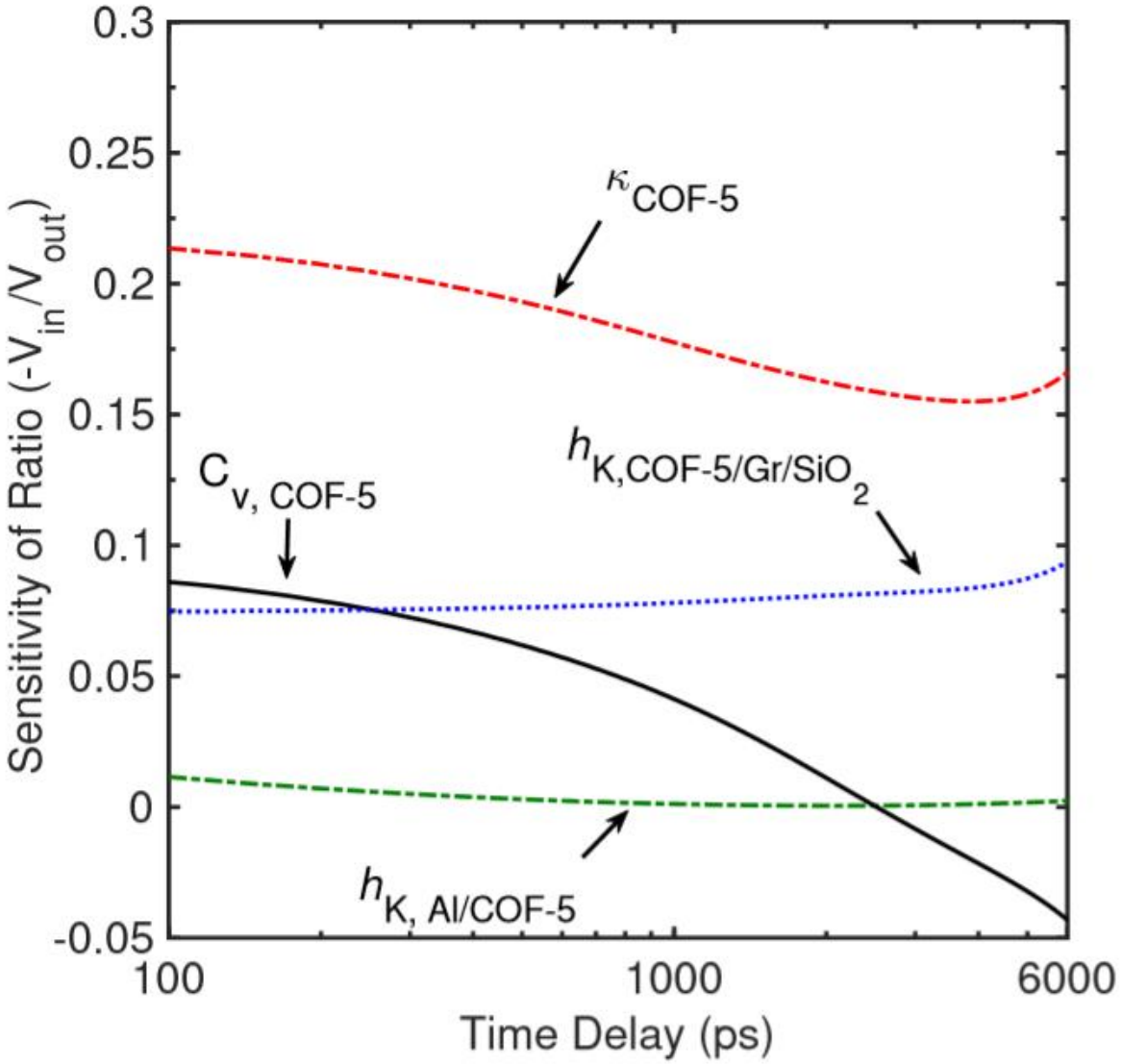

Figure S52. Sensitivity of the ratio of the in-phase (V_{in}) and out-of-phase (V_{out}) signals for COF-5 at 8.8 MHz modulation frequency.

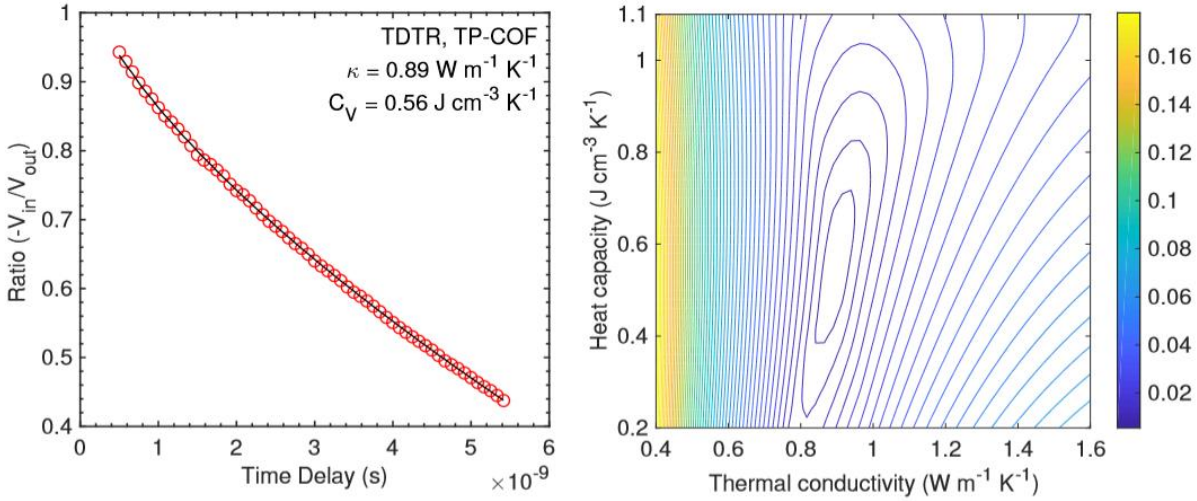

Figure S53. (Left) Characteristic TDTR data along with the best-fit curve for TP-COF. (Right) Sensitivity contour plot showing the interrelationship between the measured heat capacity and thermal conductivity of our 2D TP-COF

B. TDTR Measurements. In our TDTR setup, sub-picosecond laser pulses emanate from a Ti:Saphhire oscillator at 80MHz repetition rate. The pulses are separated into a pump path that heats up the sample and a time-delayed probe path that is reflected from the Al transducer. The reflected probe beam provides a measure of the change in the thermoreflectance due to the decay of the thermal energy deposited by the pump beam. A modulation of 8.8 MHz is applied by an electro-optic modulator on the pump beam and the ratio of the in-phase to out-of-phase signal of the reflected probe beam recorded at that frequency by a lock-in amplifier ($-V_{in}/V_{out}$) for up to 5.5 ns after the initial heating event. The pump and probe beams are focused on to the Al transducer at e^{-2} radii values of 10 and 5 μm for our pump and probe spots, respectively.

To simultaneously measure the thermal conductivity and heat capacity of our COFs, we fit a three-layer thermal model to our experimental data. However, we first consider the appropriate range of pump-probe delay times, in which the thermal model is extremely sensitive to changes in the thermophysical quantities. This is quantified by the sensitivity of the ratio (V_{in}/V_{out}) to the various thermal properties defined by,

$$S\alpha = \frac{\partial ln\left(\frac{Vin}{Vout}\right)}{\partial ln(\alpha)} \qquad (2)$$

where α is the thermophysical parameter of interest.[16] **Figure S50** shows the sensitivities of the ratio to thethermophysical parameters of the three-layer thermal model. The sensitivity to the thermal conductivity of COF-5, $\kappa_{COF\text{-}5}$, is relatively large compared to the other parameters for the entire time delay. The large and dynamic sensitivity of the heat capacity of our COF film (C_v) also allows for the simultaneous measurement of these two physical properties with relatively good precision, therefore, we treat κ_{COF} and C_v as adjustable parameters in our analytical model to fit the TDTR data for the entire pump-probe delay time.

Characteristic TDTR data and the best-fit of the thermal model for TP-COF at 8.8MHz modulation frequency is shown in **Figure S51**. **Figure S51** shows the sensitivity contour plot describing the interrelationship between the measured heat capacity and thermal conductivity of TP-COF at 8.845 MHz modulation frequency. Note, the contour plot represents the mean square deviation of our thermal model to the TDTR data with the various combinations of heat capacity and thermal conductivity as input parameters.[17,18] The standard deviation between our model and data is determined as,

$$\sigma = \frac{\sum_{j=0}^{n} (R_{m,j} - R_{d,j})^2}{n} \qquad (3)$$

where R_m and R*d* are the ratios from the model and data, respectively, and *n* is the total number of time delays considered.

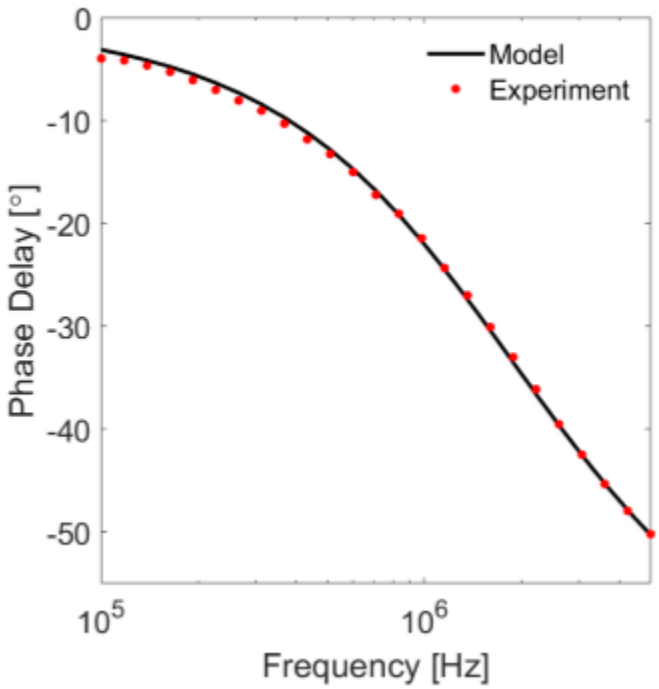

Figure S54. Phase delay data and fit as a function of modulation frequency for a representative FDTR experiment.

C. Thermal boundary conductance.

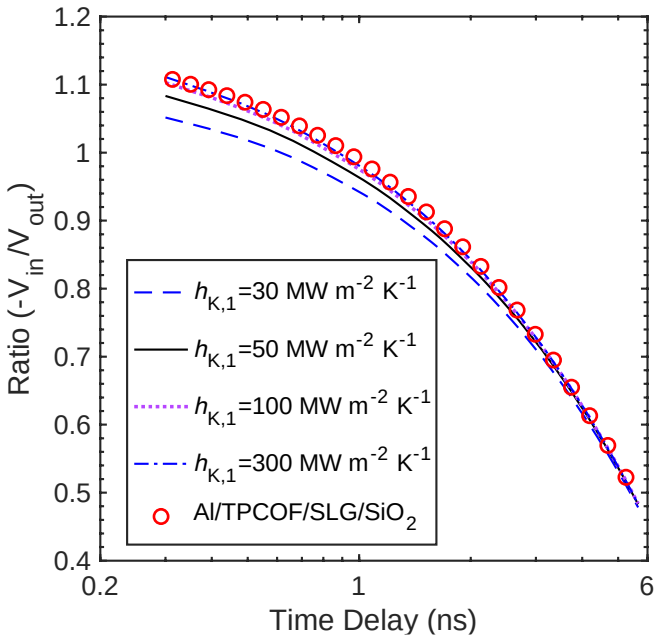

Figure S55. Analytical fits to the TDTR experimental data with different values of thermal boundary conductances across Al/COF interface $h_{K,1}$, while other parameters in the thermal model are unchanged.

From time-domain thermoreflectance measurements, we determine that the thermal resistivity of the Al/COF-5 boundary is minimal (**Fig. S55**). As observed from the analytical fits to our TDTR results with varying thermal boundary conductance (h_K) at the Al/COF interface, h_K < 70 MW m^{-2} K^{-1} results in poor fits to the experimental data as shown in Fig. R1 below. In contrast, higher h_K values optimize the fits for the early pump-probe time delays (especially at t < 1 ns). Moreover, increasing the value of h_K > 100 MW m^{-2} K^{-1} at the Al/COF interface has negligible influence on the best-fit to our experimental data. These results suggest that h_K at Al/COF is considerably higher than the conductance of our COF films.

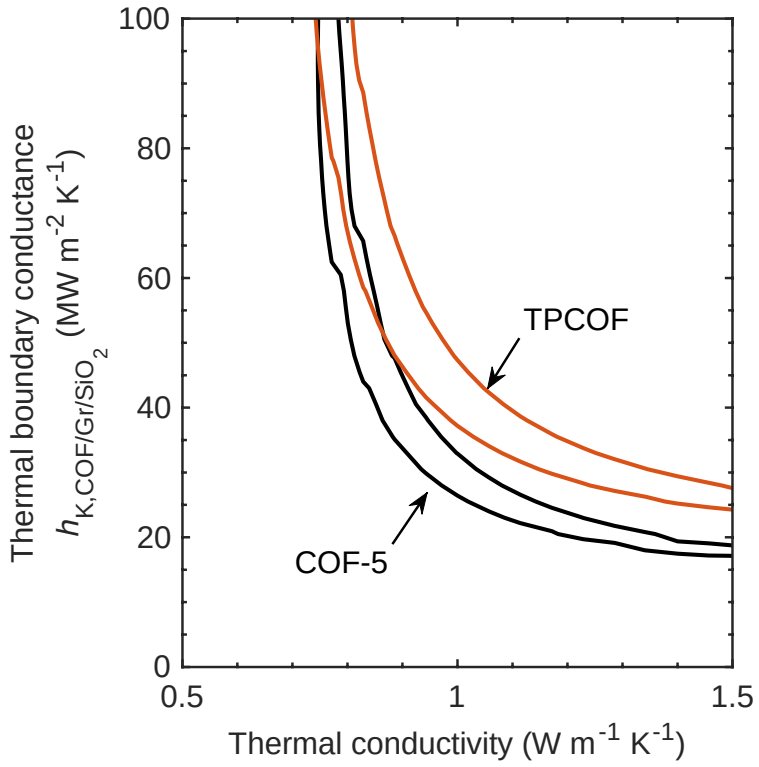

Figure S56. Sensitivity contour plot showing the interrelationship between thermal boundary conductance and thermal conductivity of our 2D COFs.

We plot sensitivity contour plots (**Fig. S56**) that represent the mean square deviation of the analytical model to our TDTR data with various combinations of thermal conductivity of COF (κ_{COF}) and $h_{K,2}$ at COF/SLG/SiO_2 interface as input parameters in our three-layer model. A combination of low $h_{K,2}$ (< 30 MW m^{-2} K^{-1}) and relatively high κ_{COF} (> 1.3 W m^{-1} K^{-1}) produce the best-fits suggesting that the resistance at the interface dominates heat transfer in the cross-plane direction. As such, we assign a lower bound of 30 MW m^{-2} K^{-1} to $h_{K,2}$ from our measurements.

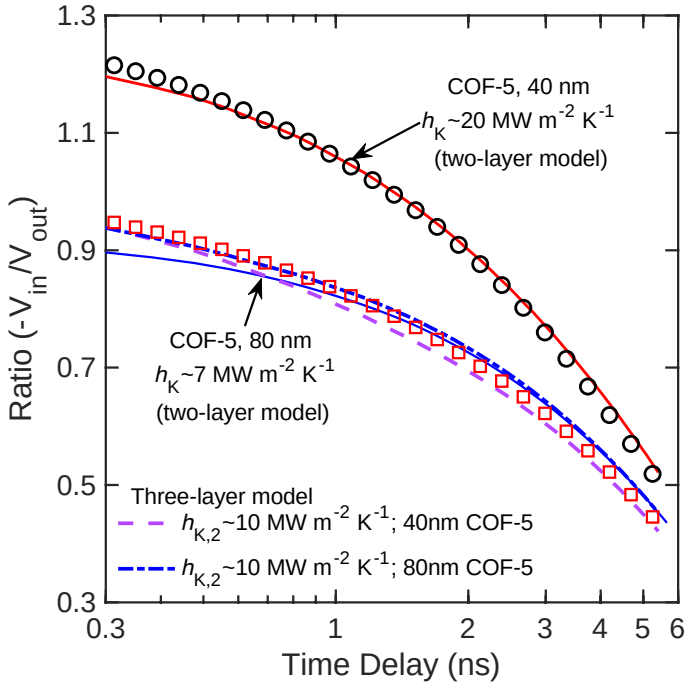

Figure 57. TDTR data for COF-5 films of 40 nm and 80 nm thickness along with the best-fit curves. The solid lines represent two-layer thermal model (for an Al/SiO_2 system) with thermal boundary conductance (h_K) as fitting parameter. The dashed and dotted-dashed lines represent three-layer thermal model with high interfacial resistances (R_K) across the COF-5/graphene/SiO_2 interface ($R_{K,2}$~10^{-7} m^2 K W^{-1}; $h_{K,2}$~10 MW m^{-2} K^{-1}) for 40 nm and 80 nm COF-5 thicknesses. A high interfacial resistance would result in poor fits to the experimental data, which suggests that interfacial resistances are much lower than the bulk resistance posed by the 2D COF thin film. As such, we are predominantly sensitive to the intrinsic thermal resistance of the 2D COF in this measurement.

In the scenario where interfacial resistances dominate heat transfer, decreasing the film thickness will have a negligible effect on total thermal transport. However, if heat transfer is dominated by the intrinsic resistance of the film, a change in the thickness results in a noteable change in the total conductance across the sample. To differentiate between these different possibilities, we synthesized an additional COF-5 film with a different thickness of that measured previously. TDTR measurements (**Figure S57**, open points) and two-layer thermal model (interfacial resistances considered as a single component) best fits (**Figure S57,** solid lines) reveals a thermal conductivity thickness dependence. To show how the fits would change if interfacial resistance would be the dominant resistance in our model, we also plot predictions from a three-layer model where we prescribe a low conductance (high resistance) across the COF-5/SLG/SiO_2 ($h_{K,2}$~ 10 MW m^{-2} K^{-1}) for 40 nm and 80 nm COF-5 samples (dashed line and dotted-dashed lines, respectively). For the scenario where thermal transport is dominated by interfacial resistance, the model predicts similar behavior for the two thicknesses, which is inconsistent with our TDTR data.

D. Frequency-Domain Thermoreflectance. To cross-validate and gain confidence in our TDTR results, we perform Frequency domain thermoreflectance (FDTR) measurements on our COF-5 sample. Similar to TDTR, FDTR is also a laser-based metrology implemented to measure thermal properties of a sample.[19,20] A thin (73.1 nm measured by KLA Tencor P-15 Profilometer) coating of Au is sputter deposited (PerkinElmer6J) on top of the sample. The Au-coated sample is periodically heated via a sinusoidally modulated (100 kHz - 5 MHz) pump laser at 488 nm wavelength. The sample's temperature will fluctuate with the same frequency as the pump laser, but with a time delay. The phase delay is characteristic of the thermal properties of the sample. The temperature is measured using a concentric probe laser (532nm), which is sensitive to the thermoreflectance of Au. The frequency-dependent time delay measured as a phase delay of the reflected probe laser with respect to the pump laser modulation frequency is measured with a photodiode connected to a lock-in amplifier. The phase delay, as shown in **Fig. S52**, is fit to an analytical solution to heat diffusion equation for a layered, semi-infinite solid to extract the thermal conductivity of the COF-5 sample. Our TDTR analysis also has sensitivity to the thermal boundary conductance across the COF-5/single layer graphene/SiO2 interface. By using the heat capacities determined via MD and FDTR (see below), we fit for a thermal boundary conductance of ~30 MW m^{-2} K^{-1}, in reasonable agreement with previous measurements across similar (single layer graphene/SiO2) interfaces.[21]

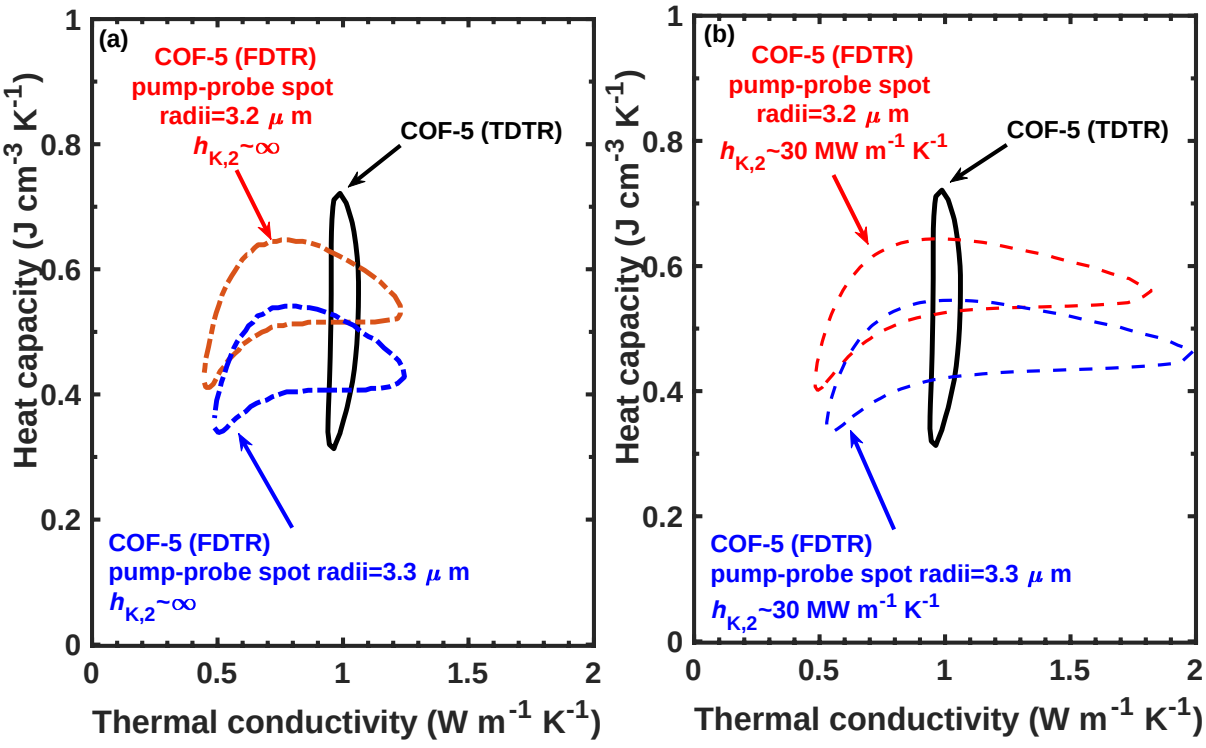

Figure S58. Contours at 1.2×Minimum MSE for FDTR data averaged over four experiments for COF-5, as a function of assumed heat capacity and thermal conductivity for 3.2 μm (red dashed line) and 3.3 μm (blue dashed line) pump-probe spot radii (a) without a resistance at the

interface and (b) with a finite thermal boundary conductance at the COF-5/SLG/SiO_2 ($h_{K,2}$ ~ 30 MW m^{-2} K^{-1}). For comparison, we also include the contour from our TDTR measurement on the same sample

COF thermal conductivity is the targeted property, but its value depends on the heat capacity of the COF, which is also unknown. We evaluated the quality of the fit between the model and data based on the mean squared error (MSE). The MSE was calculated assuming a range of thermal conductivity and heat capacity combinations and averaged for four independent data sets. In Fig.S4 we plot the global minimum MSE and a contour at 1.2 times the global minimum MSE for two different spot radii (red for a radius of 3.2 μm and blue for a radius of 3.3μm). The predicted values of thermal conductivity (κ_{COF}) and heat capacity (C_V) are sensitive to the spot size. The contours indicate that a range of $0.5 < \kappa < 2$ W m^{-1} K^{-1} and $0.33 < C < 0.63$ J cm^{-3} K^{-1} could be reasonably interpreted from the FDTR experiments. Though FDTR is less sensitive to κ than TDTR, the range of values for C and κ overlap (as shown in **Fig. S53**) and FDTR serves to strengthen the conclusion reached by TDTR.

E. Uncertainty Analysis for Thermal Properties.

To determine the uncertainties in our measurements for C_v and κ_{COF}, we use a combination of sensitivity contour analysis along with the changes in the predicted values of C_v and κ_{COF} based on perturbing different parameters in our three-layer thermal model within their error bounds. For example, we measure the thermal conductivity of aluminum as 126 ± 4 W m^{-1} K^{-1} using the four-point probe method and determine its thickness as 80 ± 3 nm using picosecond acoustics. Therefore, the uncertainty in our measured C_v and κ_{COF} includes the error associated with our thickness measurement of the aluminum transducer and its thermal conductivity, κ_{Al}. Perturbing the thickness of aluminum by 3 nm changes κ_{COF} by ~11 % and C_v by ~6 %. Whereas the error in κ_{Al} leads to a relatively lower uncertainty (of < 2 %) associated with both κ_{COF} and C_v measurements. We note that the uncertainty in C_v is relatively higher than the uncertainty in κ_{COF} since perturbing the thermal conductivity by ~2 % changes the heat capacity by ~ 20 % as shown in the sensitivity contour plot in Fig. S53. We use FDTR technique discussed in detail in the following section to reduce the uncertainty associated with our C_v measurement. We note that the biggest uncertainty to our measurements is due to the unknown $h_{K,2}$ (at the COF/Single-layer-graphene/SiO_2 interface) for which we can only set a lower estimate of ~ 50 MW m^{-2} K^{-1} as we detail below.

O. Molecular Dynamics Simulations

Our molecular dynamics (MD) simulations are performed with the LAMMPS code[22] and the interatomic interactions are described by the adaptive intermolecular reactive empirical bond order (AIREBO) potential.[23] We apply periodic boundary conditions in all directions. The computational domains are equilibrated under the Nose-Hoover thermostat and barostat,[24] (which is the NPT83 integration with the number of particles, pressure and temperature of the system held constant) for a total of 1ns at 0 bar pressure. Following the NPT integration, an NVT integration (with constant volume and number of particles) is prescribed to fully equilibrate the structures at the desired temperature for another 1 ns. Note, we prescribe a time step of 0.5 fs for all our simulations. **Figure S45a** shows an example of our computational domain for the COF-5 and the unit cell of the COF-5 is shown in **Fig S45b**. For the simulations, we vary the total cross-plane thickness, d, and length of the computational domain, L, to check for size effects in our thermal conductivity predictions as detailed below.

After equilibration, the thermal conductivities of our COFs at different temperatures predicted via the Green-Kubo (GK) approach under the EMD framework. In this formalism, the thermal conductivities of our COFs along the x-,y-(in-plane) and z-(cross-plane) directions are calculated as,

$$\kappa_{x,y,z} = \frac{1}{k_B V T^2} \int_0^\infty < S_{x,y,z}(t) \bullet S_{x,y,z}(0) > dt \qquad (4)$$

Here t is time, T and V are the temperature and volume of the systems, respectively, and $< S_{x,y,z}(t)\, S_{x,y,z}(0) >$ is the component of the heat current autocorrelation function (HCACF) in the prescribed directions.

To ensure that the HCACF decays to zero, we set the total correlation time period for the integration of the HCACF to 50 ps as shown in the inset of **Fig. 55**. The heat current is computed every 10 time steps during the data collection period, after which, integration is carried out to calculate the converged thermal conductivity for our COF-5 structure. The converged thermal conductivity is determined by averaging from 10 ps to 50 ps as shown in **Fig. S56** (dashed line). We note that since the main goal of our simulations is to establish a comparative analysis of in-plane and cross-plane thermal conductivity, we refrain from comparing our experimentally determined cross-plane thermal conductivity with our MD predictions. Moreover, the choice of the interatomic potential has large implications on the thermal conductivity predictions for similar covalently bonded carbon structures.[25-27]

The GK approach has been extensively used to predict the lattice thermal conductivity of different crystalline and amorphous material systems.[28-35] However, there has been considerable ambiguity in efficiently calculating the thermal conductivity via Eq. 4 due to uncertainties associated with finite simulation times and domain sizes.[29-31,33,36-40] To ensure that the EMD-predicted thermal conductivities are not influenced by size effects, the dimensions of the simulation box are chosen to produce converged values of thermal conductivities. To this end, the thermal conductivities of structures with cross-sections of 15×13 nm^2 and 30×26 nm^2 are

comparable within uncertainties. Similarly, the thermal conductivities of structures with computational domain sizes of 15.1×13.1×3.4 nm^3, and 15.1×13.1×10.2 nm^3 are also similar within uncertainties.

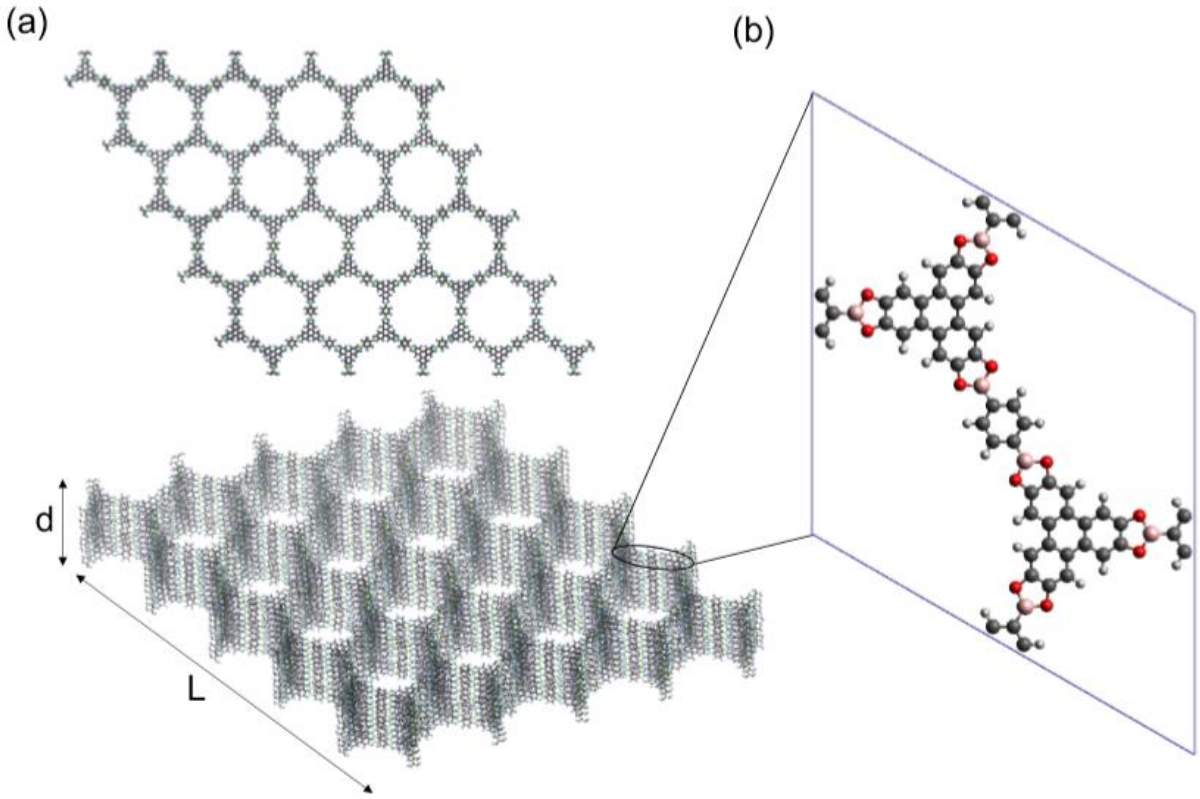

Figure S59. (a) Schematic of the computational domain of the COF-5 structure used for our molecular dynamics simulations. (b) Schematic of the unit cell of the COF-5 structure with different atomic species represented by the different colors.

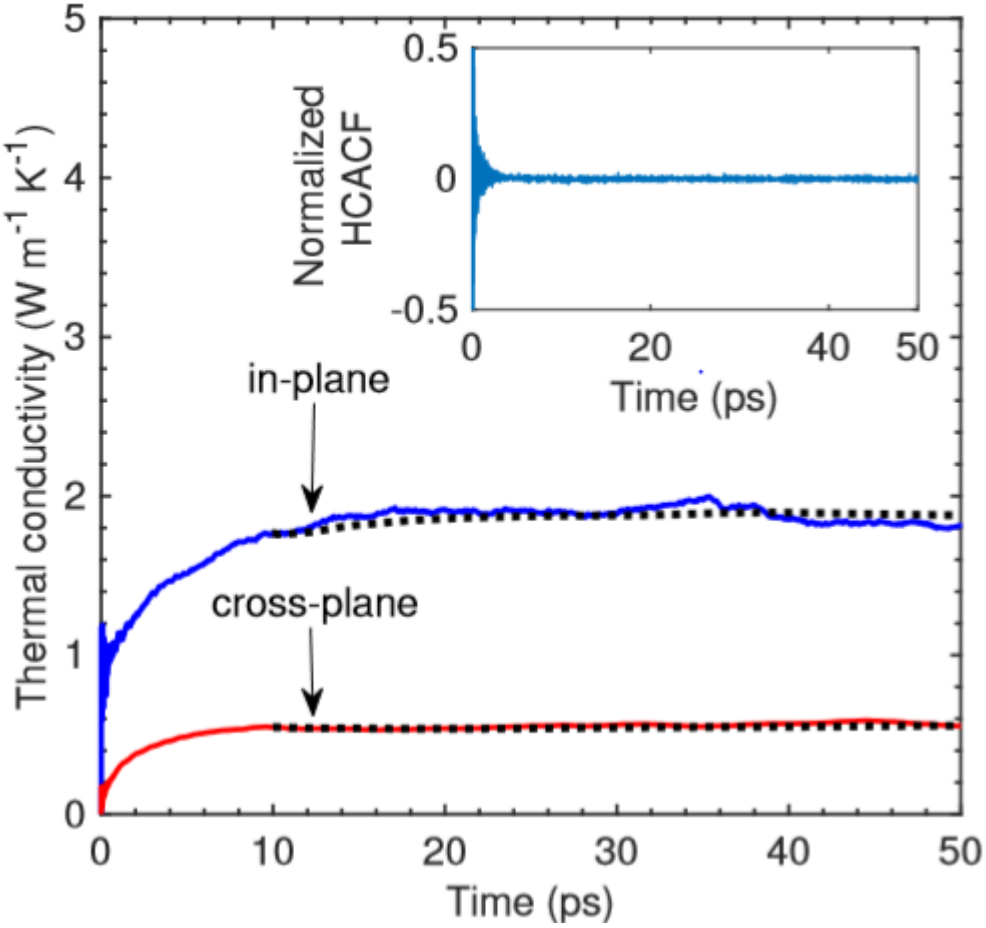

Figure S60. Converged values of in-plane and cross-plane thermal conductivities obtained for our COF-5 structure from the integral of the heat current autocorrelation function (HCACF). (inset) Normalized HCACF vs time for our COF-5 structure which shows that the HCACF decays to zero within the first 10 ps.

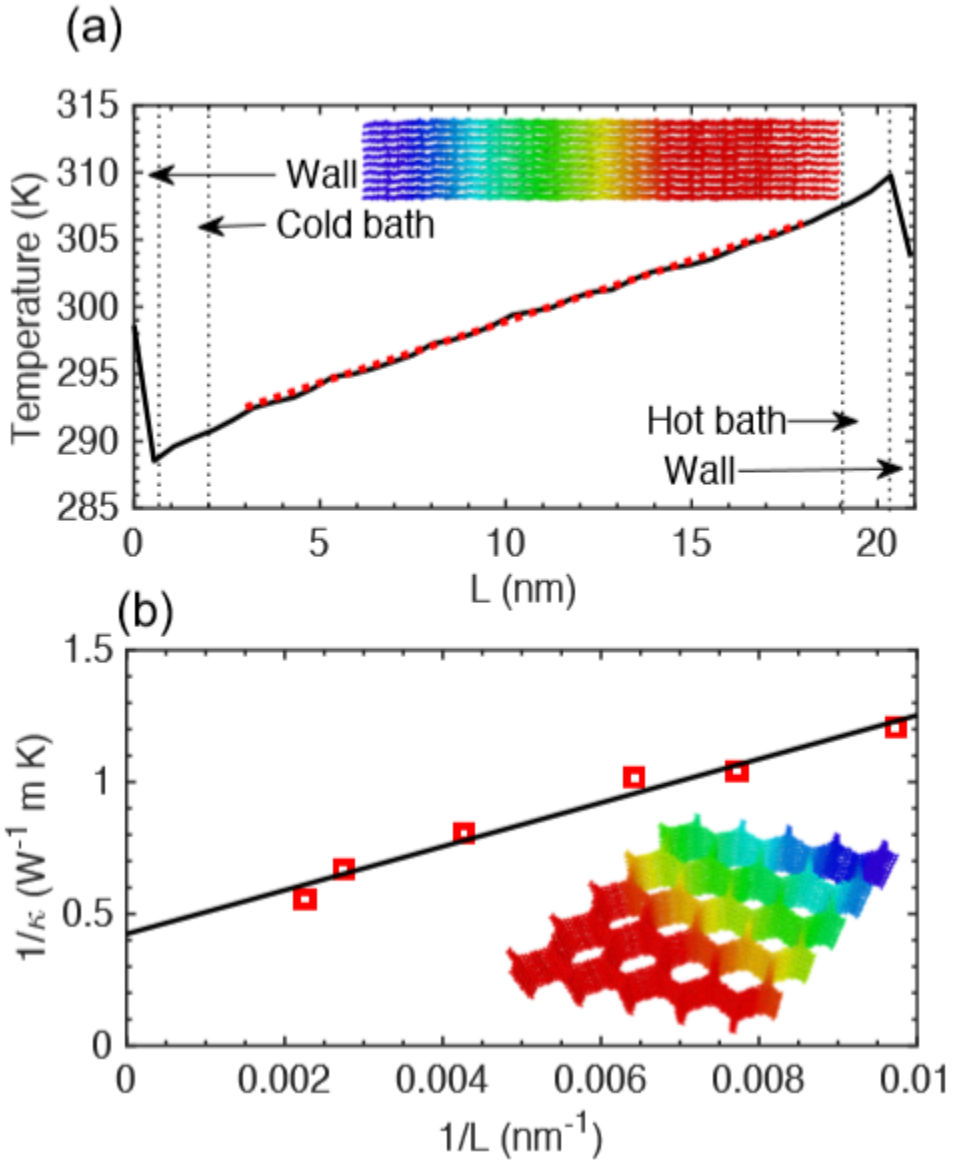

Figure S61. (a)Example of the time-averaged steady-state temperature profile in the in-plane direction of the COF-5 structure. (b) NEMD-predicted inverse of size-dependent thermal conductivities vs inverse of the computational domain length in the applied heat flux direction, which is the in-plane direction for our COF structure.

Since there has been contention on the use of the heat current calculations in LAMMPS to predict the thermal conductivity of structures with many-body interatomic potentials,[41,42] we run nonequilibrium MD (NEMD) simulations to gain more confidence in our in-plane thermal conductivity predictions for our COF-5 structure. For the NEMD simulations, a steady-state temperature gradient is established by adding a fixed amount of energy per time step to a heat bath at one end of the computational domain, while removing an equal amount of heat from a cold bath at the other end of the domain; energy is added and removed at specified rate of 0.4 eV ps^{-1} under the microcanonical ensemble where the number of atoms (N), volume (V), and

energy (E) of the system are held constant. A fixed wall at either side of the domain is enforced for our NEMD simulations. The temperature profile along the in-plane direction is obtained by averaging the temperature of the atoms along equally spaced bins in the applied heat flux direction for a total of 10 ns and the thermal conductivity is predicted via Fourier's law; the initial 3 ns of data are ignored to create time-averaged steady-state temperature profiles as shown in Fig. S8a. We calculate thermal conductivities for different domain lengths to accurately predict the bulk in-plane thermal conductivity of our COF-5 structure. For this, we plot the inverse of thermal conductivity, κ^{-1}, as a function of the inverse of the computational domain length, d^{-1}, which shows a linear trend as shown in **Fig. S56b**, and extrapolate to $d^{-1} = 0$ to predict the size-independent thermal conductivity.[43] The result of the NEMD simulations and EMD simulations are shown in **Fig 4c** of the manuscript. Our EMD simulations underpredict the cross-plane thermal conductivity of COF-5, which could potentially be due to the insufficiencies in the interatomic potential used to describe the COF structures. However, the fact that our experimental measurements are higher in comparison to the defect-free pristine structures simulated in our MD calculations, exemplifies the high quality of our crystalline 2D COFs studied in this work. From our EMD and NEMD simulations, we predict an in-plane thermal conductivity of ~2 W m^{-1} K^{-1} and an anisotropy ratio of ~4 between the in-plane and cross-plane thermal conductivity predictions.

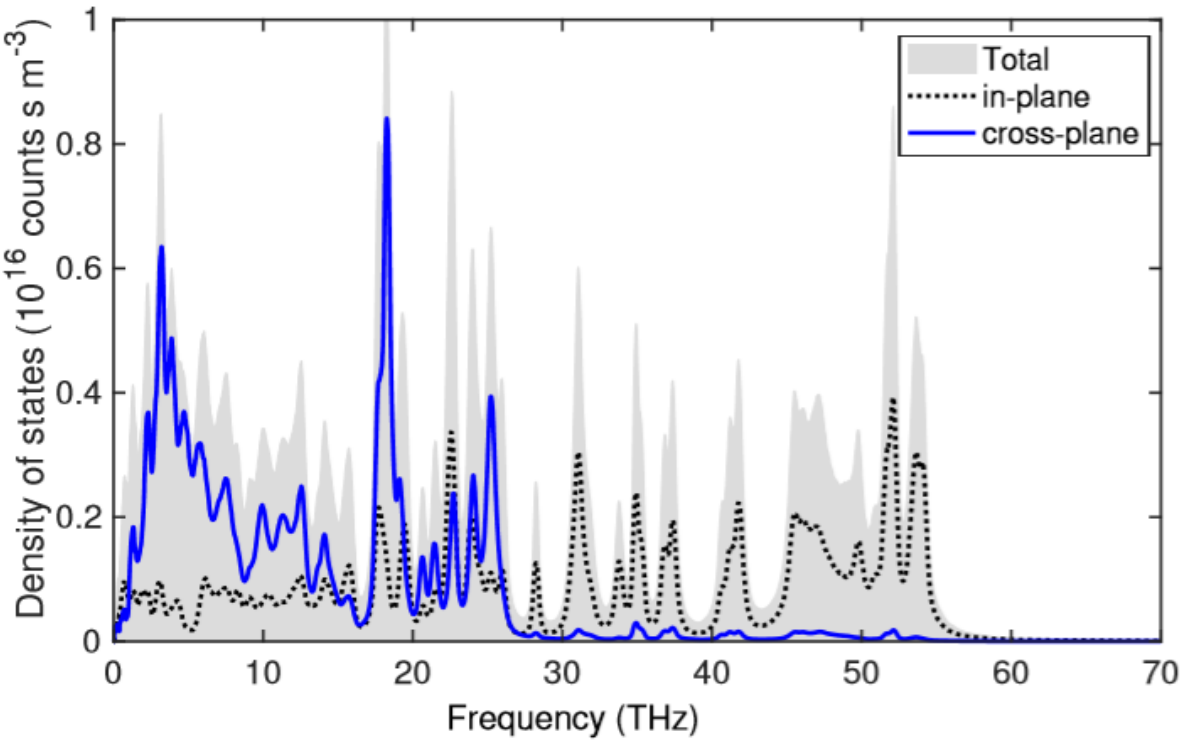

Figure S62. MD-predicted vibrational density of states for COF-5.

To get an estimate for the heat capacity of these COFs, we calculate the vibrational density of states (DOS) from our MD simulations. The velocities of the atoms in the COF-5 structure are output every 10 time steps for a total of 1ns. A velocity autocorrelation function algorithm is used to obtain the local phonon DOS in the cross-plane and in-plane directions as shown in **Fig. S57**. The density of states, D(ω), is obtained from the Fourier transform (F) of the velocity

correlation function (VACF).[28] The Welch method of power spectral density estimation is applied to obtain the D(ω) and is normalized as follows,

$$D(\omega) = \frac{1}{2} m\mathcal{F}(VACF)\left(\frac{1}{k_B T}\rho\right) \quad (5)$$

where m is the atomic mass, k_B is the Boltzmann constant, T is the local temperature, and ρ is the atomic density. We use the DOS to calculate the room temperature heat capacity as,

$$C_V = \int_0^{\omega_c} h\omega D(\omega) \frac{df}{dT} d\omega \quad (6)$$

where ω_c is the cutoff frequency, and f is the Bose-Einstein distribution. We estimate a value of $C_V \sim 0.54$ J cm^{-3} K^{-1} for our COF-5 at room temperature, which agrees well with our experimentally determined value ($C_V \sim 0.52 \pm 0.08$ J cm^{-3} K^{-1}).

To generalize our results and to investigate the effect of varying porosities on the thermal conductivity of 2D COFs, we perform additional GK simulations on structures with varying densities in the range of 0.5 g cm^{-3} to 1 g cm^{-3}. As shown in Fig. S63a, the structures compared are based on TP-COF, COF-5, and COF-1 (with pore sizes of ~3.6 nm, 2.7 nm and 1.3 nm, respectively). To investigate the effect of varying porosities while maintaining similar internal microstructure, we modify the COF-1 structure by adding a phenyl ring to the linkers (COF-1-2R, where 'R' stands for 'rings'). We compare the thermal conductivity of these four different 2D COFs with varying porosities and internal architectures in the zig-zag, arm-chair and cross-plane directions in Fig. S63b as a function of their densities. The thermal conductivity in the zig-zag and arm-chair directions are similar within uncertainties for a particular COF. More interestingly, the thermal conductivity of 2D COFs is significantly dictated by their corresponding density, both in the in-plane and cross-plane directions. These additional simulations provide design criteria for the synthesis of 2D COFs with potentially modular thermal conductivities based on controlling their porosity.

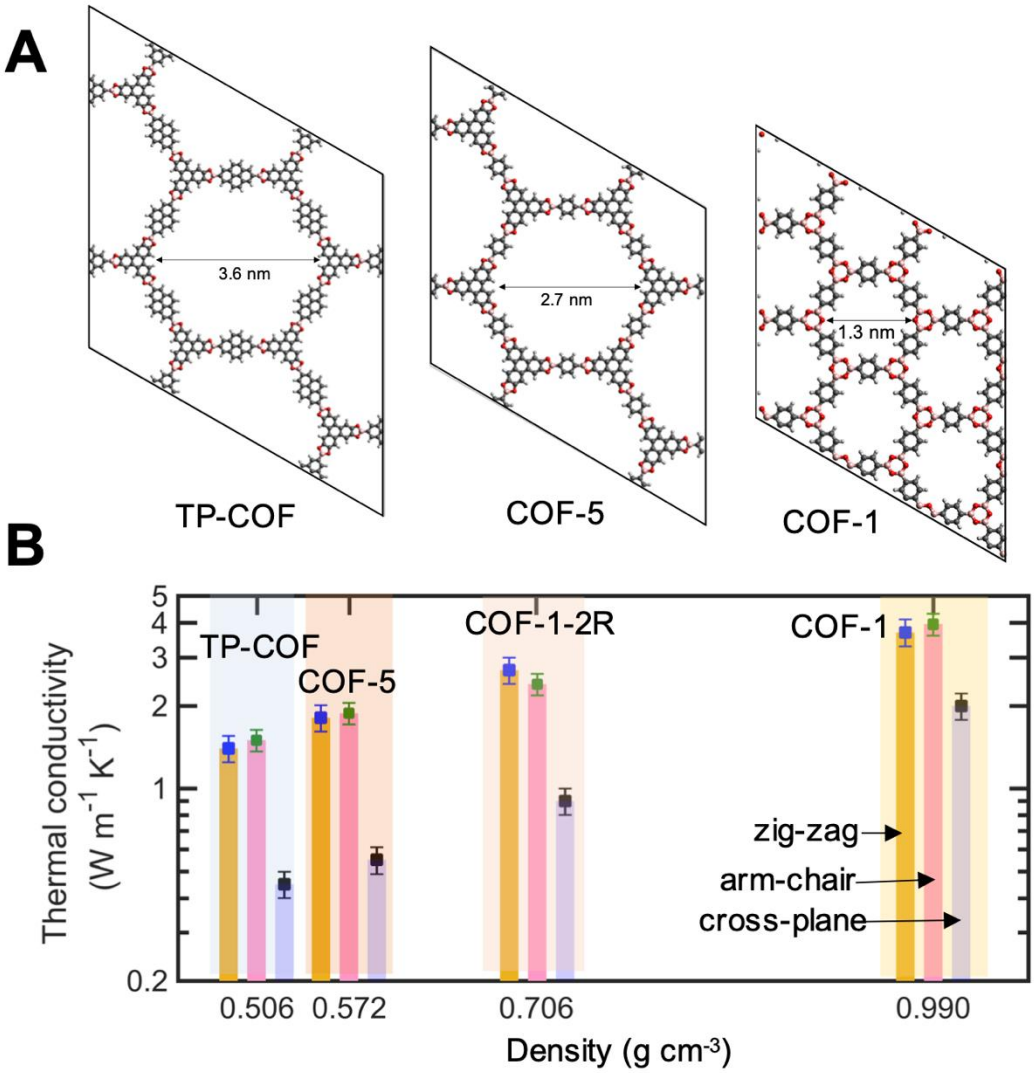

Figure S63: (A) Schematic illustration of the different molecular structures of COFs studied via MD simulations. To investigate the effect of varying porosities while maintaining similar internal microstructure, we modify the COF-1 structure by adding a phenyl ring to the linkers (COF-1-2R, where `R' stands for `rings'). (B) The thermal conductivity in the three principal directions for the COFs scales linearly as a function of their density suggesting that porosity can significantly control thermal transport in both in-plane and cross-plane directions in 2D COFs.

P. Comparative Finite-Element Solutions for Dielectric Films

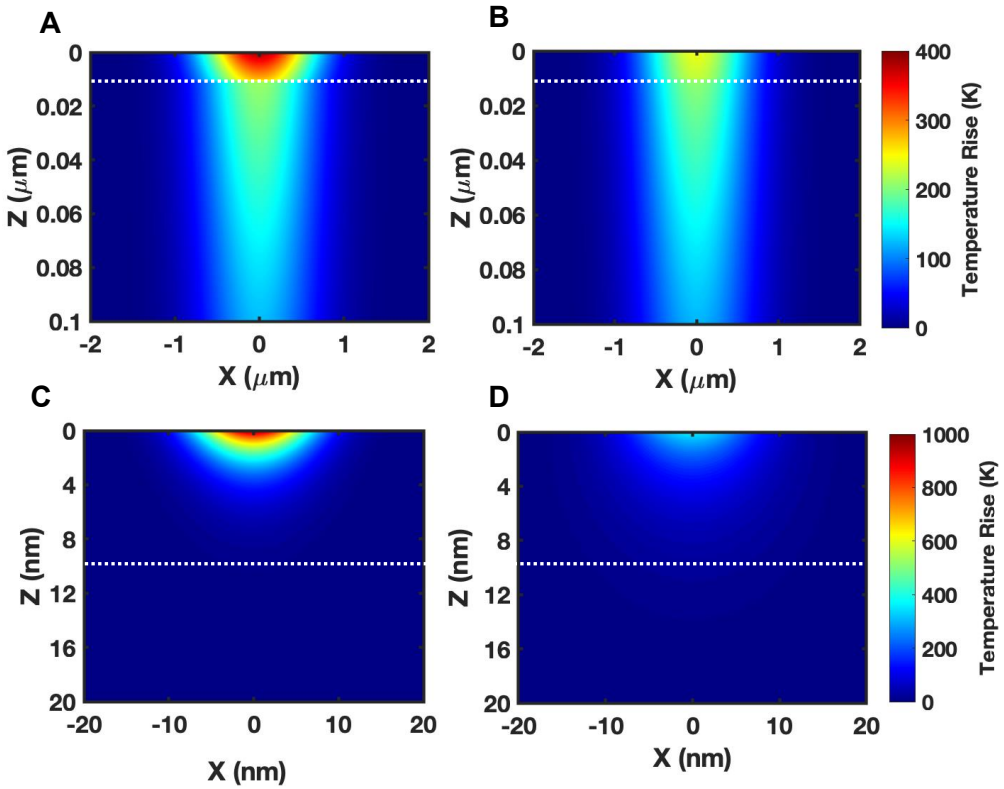

Figure S64: Temperature profiles as a function of radius and depth for a 10 nm conventional low-*k* dielectric thin film (with κ = 0.2 W m^{-1} K^{-1}) and for a 10 nm 2D COF/SLG/SiO_2 sample subjected to radially symmetric Gaussian surface heating event. Temperature profiles resulting from a heating event with 1/e^2 radius of 1 μm and an average absorbed power of ~4 mW in (A) a conventional 10 nm low-*k* dielectric thin film as compared that in a (B) 10 nm 2D COF/SLG/SiO_2 sample. Temperature profiles resulting from a heating event with 1/e^2 radius of 10 nm and an average absorbed power of ~4 mW in (C) a conventional 10 nm low-*k* dielectric thin film as compared to that in a (D) 10 nm 2D COF/SLG/SiO_2 sample.

To emphasize the potential application of our 2D COFs as highly thermally conductive ultra-low-*k* coatings in integrated circuits (with the next generation sub-10 nm technology nodes), we perform calculations of the steady-state temperature rise in these devices with varying heater radius and compare the results to that calculated for a conventional low-*k* dielectric thin film (with κ = 0.2 W m^{-1} K^{-1}). The details of the calculations can be found in our earlier work.[44] As shown in Fig. S64, when the "hot-spot" is much larger than the 10 nm thin film, a considerable temperature drop occurs at the interface between the film and the substrate for both the conventional low-*k* dielectric film and in the 2D COF sample geometry as shown in **Fig. S64A and S64B**, respectively. However, the 5 times larger thermal conductivity of the 2D COF greatly mitigates the "hot-spot" buildup and can lower the peak temperature by as much as half

the peak temperature that is built up in the conventional low-*k* dielectric film. The thermal mitigation capability of 2D COFs is further highlighted for the case when the characteristic size of the "hot-spots" are similar to the film thickness. For the conventional low-*k* dielectric case, a large temperature rise is observed at the surface of the film, however, due to the comparatively higher thermal conductivity of the 2D COF, considerable in-plane heat flow mitigates the "hot-spot" buildup. In these types of cases with heat sources length scales on the order of 10 nm (such as those in current and next generation IC technology nodes), device failure due to thermal buildup usually results from the lower thermal conductivity of the low-*k* dielectric film.

Q. Meta-Data Analysis

Table S7. Meta-analysis of other low-*k* dielectrics that have reported thermal conductivities.

Material	Dielectric Constant	Thermal Conductivity (W m^{-1} K^{-1})	Density (g cm^{-3})	References
Porous Silicon Oxide Aerogel	2.1	0.14	0.8	A.Delan et al./Microelectronic Engineering 70 (2003) 280–284
Orion, Porous SiOCH	2.2	0.16	1.04	A.Delan et al./Microelectronic Engineering 70 (2003) 280–284
methyl silsesquioxane	2.2	0.19	0.95	A.Delan et al./Microelectronic Engineering 70 (2003) 280–284
Philk, Porous Oxide	1.9	0.15	0.9	A.Delan et al./Microelectronic Engineering 70 (2003) 280–284
SiLK, Porous Organic Polymer	2.1	0.11	1.2	A.Delan et al./Microelectronic Engineering 70 (2003) 280–284
Fluorinated Carbon Polymer	2.3	0.13	1.84	A.Delan et al./Microelectronic Engineering 70 (2003) 280–284
MOF-5	2.7	0.1	0.5	H. Guo et al. / Microporous and Mesoporous Materials 221 (2016) 40-47
ZIF-4	1.85	0.28	1.2	Tan et al. / Phys. Chem. Let 9 (2018) 2678-2684
ZIF-7	2	0.21	1.25	Tan et al. / Phys. Chem. Let 9 (2018) 2678-2684
ZIF-8	1.65	0.3	0.95	Tan et al. / Phys. Chem. Let 9 (2018) 2678-2684
SiO_2 Xerogels	1.65	0.08	0.5	Plawsky et al./J. Vac. Sci. Technol. B 17 (1999) 205-210
SiO2 Xerogels	1.8	0.1	0.6	Plawsky et al./J. Vac. Sci. Technol. B 17 (1999) 205-210
SiO2 Xerogels	2	0.14	0.7	Plawsky et al./J. Vac. Sci. Technol. B 17 (1999) 205-210
Polyvinylchloride	4	0.21	1.38	G. Maier / Prog. Polym. Sci. 26 (2001) 3-654
Polyamide, (Nylon 66)	3.8	0.23	1.14	G. Maier / Prog. Polym. Sci. 26 (2001) 3-654
Polysulfone	1.52	0.26	1.24	G. Maier / Prog. Polym. Sci. 26 (2001) 3-654
Polyimide (Kapton)	3.4	0.8	1.42	G. Maier / Prog. Polym. Sci. 26 (2001) 3-654
Polytetrafluoroethylene	2.02	0.25	2.2	G. Maier / Prog. Polym. Sci. 26 (2001) 3-654
Polystyrene	2.7	0.03	1	G. Maier / Prog. Polym. Sci. 26 (2001) 3-654
Amorphous SiO_2	3.8	0.8	2.65	G. Ozin et al./Materials Today 9 (2006) 22-31
Crystalline SiO_2	3.8	1.3	2.65	G. Ozin et al./Materials Today 9 (2006) 22-31
Fluorine-Doped SiO_2	3.55	0.8	2.21	G. Ozin et al./Materials Today 9 (2006) 22-31
Organosilicate Glass	3	0.39	1.4	G. Ozin et al./Materials Today 9 (2006) 22-31
Al_2O_3	7.8	12	3.95	G. Ozin et al./Materials Today 9 (2006) 22-31

R. References

1 Jiang, Z. GIXSGUI: a MATLAB toolbox for grazing-incidence X-ray scattering data visualization and reduction, and indexing of buried three-dimensional periodic nanostructured films. *J. Appl. Crystallogr.* **48**, 917-926 (2015).

2 Ilavsky, J. Nika: software for two-dimensional data reduction. *J. Appl. Crystallogr.* **45**, 324-328 (2012).

3 Nelson, A. Co-refinement of multiple-contrast neutron/X-ray reflectivity data using MOTOFIT. *J. Appl. Crystallogr.* **39**, 273-276 (2006).

4 Wan, S., Guo, J., Kim, J., Ihee, H. & Jiang, D. A belt‐shaped, blue luminescent, and semiconducting covalent organic framework. *Angew. Chem. Int. Ed.* **47**, 8826-8830 (2008).

5 Spitler, E. L. *et al.* A 2D covalent organic framework with 4.7-nm pores and insight into its interlayer stacking. *J. Am. Chem. Soc.* **133**, 19416-19421 (2011).

6 Dharmapurikar, S. S., Arulkashmir, A., Das, C., Muddellu, P. & Krishnamoorthy, K. Enhanced hole carrier transport due to increased intermolecular contacts in small molecule based field effect transistors. *ACS Appl. Mater. Inter.* **5**, 7086-7093 (2013).

7 Colson, J. W. *et al.* Oriented 2D covalent organic framework thin films on single-layer graphene. *Science* **332**, 228-231 (2011).

8 Dovesi, R. *et al.* Quantum-mechanical condensed matter simulations with CRYSTAL. *WIREs Computational Molecular Science* **8**, e1360, doi:10.1002/wcms.1360 (2018).

9 R. Dovesi, V. R. S., C. Roetti, R. Orlando, C. M. Zicovich-Wilson, F. Pascale, B. Civalleri, K. Doll, N. M. Harrison, I. J. Bush, P. D'Arco, M. Llunell, M. Causà, Y. Noël, L. Maschio, A. Erba, M. Rerat, S. Casassa. *CRYSTAL17 User's Manual (University of Torino, Torino, 2017)*.

10 Adamo, C. & Barone, V. Toward reliable density functional methods without adjustable parameters: The PBE0 model. *The Journal of Chemical Physics* **110**, 6158-6170, doi:10.1063/1.478522 (1999).

11 Peintinger, M. F., Oliveira, D. V. & Bredow, T. Consistent Gaussian basis sets of triple-zeta valence with polarization quality for solid-state calculations. *Journal of Computational Chemistry* **34**, 451-459, doi:10.1002/jcc.23153 (2013).

12 Grimme, S., Ehrlich, S. & Goerigk, L. Effect of the damping function in dispersion corrected density functional theory. *Journal of Computational Chemistry* **32**, 1456-1465, doi:10.1002/jcc.21759 (2011).

13 Gajdoš, M., Hummer, K., Kresse, G., Furthmüller, J. & Bechstedt, F. Linear optical properties in the projector-augmented wave methodology. *Physical Review B* **73**, 045112, doi:10.1103/PhysRevB.73.045112 (2006).

14 Perdew, J. P., Burke, K. & Ernzerhof, M. Generalized Gradient Approximation Made Simple. *Physical Review Letters* **77**, 3865-3868, doi:10.1103/PhysRevLett.77.3865 (1996).

15 Gonze, X. Adiabatic density-functional perturbation theory. *Physical Review A* **52**, 1096-1114, doi:10.1103/PhysRevA.52.1096 (1995).

16 Costescu, R. M., Wall, M. A. & Cahill, D. G. Thermal conductance of epitaxial interfaces. *Phys. Rev. B* **67**, 054302 (2003).

17 Giri, A., Niemelä, J.-P., Szwejkowski, C. J., Karppinen, M. & Hopkins, P. E. Reduction in thermal conductivity and tunable heat capacity of inorganic/organic hybrid superlattices. *Phys. Rev. B.* **93**, 024201 (2016).
18 Wang, X., Liman, C. D., Treat, N. D., Chabinyc, M. L. & Cahill, D. G. J. P. R. B. Ultralow thermal conductivity of fullerene derivatives. *Phys. Rev. B* **88**, 075310 (2013).
19 Schmidt, A. J., Cheaito, R. & Chiesa, M. A frequency-domain thermoreflectance method for the characterization of thermal properties. *Rev. Sci. Instrum.* **80**, 094901 (2009).
20 Malen, J. A. *et al.* Optical measurement of thermal conductivity using fiber aligned frequency domain thermoreflectance. *J. Heat Trans.* **133** (2011).
21 Koh, Y. K., Bae, M.-H., Cahill, D. G. & Pop, E. Heat conduction across monolayer and few-layer graphenes. *Nano Lett.* **10**, 4363-4368 (2010).
22 Plimpton, S. *J. Comp. Phys.* **117**, 1-19 (1995).
23 Stuart, S. J., Tutein, A. B. & Harrison, J. A. A reactive potential for hydrocarbons with intermolecular interactions. *J. Chem. Phys.* **112**, 6472-6486 (2000).
24 Hoover, W. G. & Posch, H. A. Direct measurement of Lyapunov exponents. *Phys. Let. A* **113**, 82-84 (1985).
25 Giri, A. & Hopkins, P. E. Resonant phonon modes in fullerene functionalized graphene lead to large tunability of thermal conductivity without impacting the mechanical properties. *J. Appl. Phys.* **125**, 205102 (2019).
26 Salaway, R. N. & Zhigilei, L. V. Molecular dynamics simulations of thermal conductivity of carbon nanotubes: Resolving the effects of computational parameters. *Int. J. Heat Mass Transf.* **70**, 954-964 (2014).
27 Lukes, J. R. & Zhong, H. Thermal conductivity of individual single-wall carbon nanotubes. *J. Heat Trans.* (2007).
28 Allen, M. P. & Tildesley, D. J. *Computer simulation of liquids*. (Oxford university press, 2017).
29 Schelling, P. K., Phillpot, S. R. & Keblinski, P. Comparison of atomic-level simulation methods for computing thermal conductivity. *Phys. Rev. B* **65**, 144306 (2002).
30 McGaughey, A. & Kaviany, M. Thermal conductivity decomposition and analysis using molecular dynamics simulations. Part I. Lennard-Jones argon. *Int. J. Heat Mass Transf.* **47**, 1783-1798 (2004).
31 McGaughey, A., Kaviany, M. J. I. J. o. H. & Transfer, M. Thermal conductivity decomposition and analysis using molecular dynamics simulations: Part II. Complex silica structures. *Int. J. Heat Mass Transf.* **47**, 1799-1816 (2004).
32 Henry, A. S. & Chen, G. Spectral phonon transport properties of silicon based on molecular dynamics simulations and lattice dynamics. *J. Comput. Theor. Nanos.* **5**, 141-152 (2008).
33 Wang, Z., Safarkhani, S., Lin, G. & Ruan, X. Uncertainty quantification of thermal conductivities from equilibrium molecular dynamics simulations. *Int. J. Heat Mass Transf.* **112**, 267-278 (2017).
34 Lv, W. & Henry, A. Direct calculation of modal contributions to thermal conductivity via Green–Kubo modal analysis. *New. J. Phys.* **18**, 013028 (2016).

35 Chalopin, Y., Esfarjani, K., Henry, A., Volz, S. & Chen, G. Thermal interface conductance in Si/Ge superlattices by equilibrium molecular dynamics. *Phys. Rev. B* **85**, 195302 (2012).
36 Che, J. Ç. a. T., Deng W and Goddard. Thermal conductivity of diamond and related materials from molecular dynamics simulations. *J. Chem. Phys.* **113**, 6888 (2000).
37 Chen, J., Zhang, G. & Li, B. How to improve the accuracy of equilibrium molecular dynamics for computation of thermal conductivity? *Phys. Let. A* **374**, 2392-2396 (2010).
38 Volz, S. G. & Chen, G. Molecular-dynamics simulation of thermal conductivity of silicon crystals. *Phys. Rev. B* **61**, 2651 (2000).
39 Dong, H., Fan, Z., Shi, L., Harju, A. & Ala-Nissila, T. Equivalence of the equilibrium and the nonequilibrium molecular dynamics methods for thermal conductivity calculations: From bulk to nanowire silicon. *Phys. Rev. B* **97**, 094305 (2018).
40 Sun, L. & Murthy, J. Y. Domain size effects in molecular dynamics simulation of phonon transport in silicon. *Appl. Phys. Let.* **89**, 171919 (2006).
41 Fan, Z. *et al.* Force and heat current formulas for many-body potentials in molecular dynamics simulations with applications to thermal conductivity calculations. *Phys. rev. B* **92**, 094301 (2015).
42 Boone, P., Babaei, H., Wilmer, C. E. J. J. o. c. t. & computation. Heat flux for many-body interactions: Corrections to LAMMPS. *J. Chem. Theory Comp.* **15**, 5579-5587 (2019).
43 Sellan, D. P., Landry, E. S., Turney, J., McGaughey, A. J. & Amon, C. H. Size effects in molecular dynamics thermal conductivity predictions. *Phys. Rev. B* **81**, 214305 (2010).
44 Braun, J. L., Szwejkowski, C. J., Giri, A. & Hopkins, P. E. On the steady-state temperature rise during laser heating of multilayer thin films in optical pump–probe techniques. *J. Heat Transfer* **140** (2018).